Master's thesis

NTNU
Norwegian University of Science and Technology
Faculty of Engineering
Department of Civil and Environmental Engineering

Ida Lindkvist

Bridge Abutment Using Geosynthetic Reinforced Soil Technique

Master's thesis in Civil and Environmental Engineering
Supervisor: Arnstein Watn
Co-supervisor: Yutao Pan
January 2022

NTNU
Norwegian University of
Science and Technology

Ida Lindkvist

Bridge Abutment Using Geosynthetic Reinforced Soil Technique

Master's thesis in Civil and Environmental Engineering
Supervisor: Arnstein Watn
Co-supervisor: Yutao Pan
January 2022

Norwegian University of Science and Technology
Faculty of Engineering
Department of Civil and Environmental Engineering

NTNU
Norwegian University of
Science and Technology

Abstract

Geosynthetic reinforced soil bridge abutments are the supporting structure for a bridge, conducted by compacted soil and geosynthetic reinforcement. Incorporation of the reinforcement increases the tensile and shear strength of the soil, resulting in a material having higher resistance to failure and deformations. Geosynthetic reinforced soil structures can in many cases be established with a shorter constructing time, at a lower cost, and to a larger extent using local materials compared to conventional structures. With these environmental and economical benefits, it is a viable alternative to traditional practice.

This thesis looks further into deformations and behaviour of geosynthetic reinforced soil structures. Two existing geosynthetic reinforced slopes built in Norway during the late 80's and early 90's have been monitored with respect to deformations, strains and forces. The slopes are used as calibration cases and have been modelled using a finite element program, thereafter comparing the output to the monitored results. This modelling approach gives a satisfying correlation between monitored results and results from the modelling and is further used to analyse a case where geosynthetic reinforced soil bridge abutment is a possible solution.

The two slopes modelled in the calibration case are located in Lillehammer and Skedsmo. The slope in Lillehammer did not experience any additional load after the construction were finished, while the Skedsmo slope was exposed to external load after the end of construction. Results from modelling the slope in Skedsmo fits reasonably well with the monitored results for the case. Deformations were not monitored for the particular case, but are reasonable when comparing to expected values found in literature. Overall, the results correlates sufficiently to argue that the approach used when modelling the Skedsmo slope gives a realistic prediction of the behaviour of a reinforced structure, and can be adapted to further use. For the slope in Lillehammer, the model did not successfully predict the long-term deformations which had been monitored. However, the output showed realistic responses in the construction part of the modelling. To get a better prediction of long-term deformations, more advanced soil models should be applied. The modelling approach used in the slopes can successfully be adapted to structures having a similar load pattern as the Skedsmo slope.

For better calibration of the finite element model, it would be preferable to have a case with similar loading conditions as a bridge abutment where deformations are monitored over time. There is also uncertainties linked to the soil parameters in the calibration case, and a more exact mapping of the soil and its properties would give a more precise calibration model.

A smaller bridge, located in Risheim in Norway will eventually be replaced, and geosynthetic reinforced soil abutments could be a possible option. A design was suggested for the abutment and modelled using the modelling approach found for the Skedsmo case. Finite

element analysis were conducted, analysing both stability and deformations. The analysis exhibited sufficient stability for the abutment. Deformations from the analysis where within the acceptable range, comparing to literature and standards. Strains and forces in the geosynthetic reinforcement were realistic, being in the same magnitude as for the slope in Skedsmo, and within the requirements from literature and standards. The analysis over time showed that a majority of the deformations occurred instantly or within a short range of time after the load was applied, and after 1.5 to 2 years the change in deformations were close to zero. All in all, the results lead to the conclusion that geosynthetic reinforced soil bridge abutments can be good solution for the Rishem case, as well as cases with similar properties, and it is a relevant option to further investigate.

Sammendrag

Geosyntetisk armert jord er et kompositttmateriale sammensatt av kompaktert jord og geosyntetisk armering. I et brofundament er det denne kompositttkonstruksjonen som bærer broen. Ved å inkludere armeringen vil strekk- og skjærstyrken til jorden øke, som gir et materiale med større motstand mot brudd og deformasjoner. Geosyntetisk armerte jordstrukturer kan i mange tilfeller etableres på kortere tid, til en lavere kostnad og kan utnytte lokale materialer til en større grad sammenlignet med konvensjonelle løsninger. Disse økonomiske og miljømessige fordelene gjør det til et interessant alternativ til tradisjonell praksis.

Denne oppgaven ser på deformasjoner og oppførsel til konstruksjoner hvor geosyntetisk armering er brukt. To armerte skråninger, konstruert i Norge på sent 80-tall og tidlig 90-tall, har blitt overvåket, og deformasjoner, tøyninger og krefter er målt. Disse skråningene er brukt til kalibrering, og deretter modellert i et finite element-program, hvor analyseresultatene sammenlignes med de målte resultatene. Den modellen som gir en tilfredsstillende overenstemmelse mellom modellen og målte resultater vil videre bli brukt til å analysere et brofundament der geosyntetisk armering er en mulig løsning.

De to modellerte skråningene brukt til kalibrering er bygget på Lillehammer og Skedsmo. Skråningen i Lillehammer er ikke ytterligere belastet etter konstruksjonen ble ferdig, mens skråningen i Skedsmo har fått ytterligere belastning etter endt konstruksjon. Resultatene fra modelleringen av skråningen i Skedsmo stemmer rimelig godt med hva som er målt. Deformasjonen var ikke målt i Skedsmo, men er innenfor det som kan forventes i et slikt tilfelle, basert på litteratur og teori. Totalt sett korrelerer resultatene godt nok til å argumentere for at modelleringstilnærmingen brukt for skråningen i Skedsmo gir et realistisk bilde av oppførselen til en armert konstruksjon, og kan tilpasses og brukes videre. For skråningen i Lillehammer overensstemmer ikke de målte langtidsdeformasjonene med resultatene fra modellen, men responsen i konstruksjonsdelen av modellen er realistisk. For å bedre predikere langtidsdeformasjoner må man ta i bruk mer avanserte jordmodeller. Tilnærmingen brukt i modelleringen av skråningene kan med fordel brukes og tilpasses konstruksjoner med lignende belastningsmønster som skråningen i Skedsmo.

For å forbedre kalibreringen av finite element-modellen, er det ønskelig å se på et tilfelle med lignende belastningsmønster som et brofundament, der deformasjonene er overvåket. Det er i tillegg noe usikkerhet knyttet til jordparametrene i kalibrerings-tilfellene, og en mer nøyaktig undersøkelse av disse vil gi mindre usikkerhet i modellen.

En mindre bro, med beliggenhet ved Risheim i Norge, skal i fremtiden erstattes. Fundamenter av geosyntetisk armert jord er en mulig løsning for den nye broen. Et designforslag er presentert og modellert med tilnærmingen funnet for skråningen i Skedsmo. Finite element-analyse er gjennomført med fokus på stabilitet og deformasjoner. Deformasjonene er funnet å være innenfor akseptable verdier i henhold til litteratur og standarder. Tøyning og krefter i den geosyntetiske armeringen virker realistiske, ettersom de

er i samme størrelsesorden som skråningen i Skedsmo og er innenfor kravene fra litteratur og standarder. Analysen over tid viser at mesteparten av deformasjonene skjer direkte eller rett etter at konstruksjonen er belastet, og etter 1.5 til 2 år er forandringen i deformasjonene tilnærmet lik null. Totalt sett viser resultatene at brofundament av geosyntetisk armert jord kan være en god løsning i Risheim og i tilfeller med lignende forutsetninger, og er et relevant alternativ for videre undersøkelser.

Preface

This master's thesis is the final part of a five-year master's degree in geotechnical engineering, written in the autumn of 2021. The thesis is written at the Norwegian University of Science and Technology (NTNU) in Trondheim, at the Department of Civil and Environmental Engineering.

I would like to thank my main supervisor Arnstein Watn for his guidance, encouragement and sharing his experience with me and Yutao Pan for all the help with the challenges of finite element modelling. I would also like to thank Adrian for his patience, help and for knowing where I was lost in the were and was.

Trondheim, January 2022

Ida Lindkvist

Contents

List of Tables

List of Figures

Abbreviations

ASTM	=	American Society for Testing and Materials
CPTU	=	Cone Penetration Test Undrained
FE	=	Finite Element
FEM	=	Finite Element Method
GRS	=	Geosynthetic Reinforced Soil
IBS	=	Integrated Bridge System
GMSE	=	Geosynthetic Mechanically Stabilized Earth
MSE	=	Mechanically Stabilized Earth
PET	=	Polyester
PE	=	Polyethylene
PP	=	Polypropylene
PA	=	Polyamid
HDPE	=	High Density Polyethylene
NCHRP	=	National Cooperative Highway Research Program
HL	=	Higher Limit
LL	=	Lower Limit
UB	=	Undrained B
RSF	=	Reinforced Soil Foundation

List of Symbols

a	=	Attraction
$b_{q,vol}$	=	Width along top of GRS structure
CRF	=	Creep Reduction Factor
c	=	Cohesion
c_u	=	Undrained shear strength
c_R	=	Cohesion including reinforcement strength
D_L	=	Lateral displacement
D_V	=	Vertical displacement
H	=	Height of GRS structure
E	=	Youngs modulus
EA	=	Axial stiffness
E_r	=	Youngs modulus reinforced soil
E_{50}^{ref}	=	Reference Shear stiffness
E_{oed}^{ref}	=	Reference volumetric stiffness
E_{ur}^{ref}	=	Reference unloading stiffness
E_{50}	=	Shear stiffness
E_{oed}	=	Volumetric stiffness
E_{ur}	=	Unloading stiffness
FS_{po}	=	Required safety factor against pullout
F_S, F_D, F_C	=	Reduction Factors
K'	=	Effective coefficient for lateral stress
K_a	=	Coefficient of lateral stress in unreinforced soil, active state
K_r	=	Coefficient of lateral stress in reinforced soil
K_0	=	Coefficient of lateral stress, rest state
k	=	Seepage
l_u	=	Failure envelope of unreinforced soil
l_{RC}	=	Failure envelope of reinforced soil, with c_R
l_{RF}	=	Failure envelope of reinforced soil, with ϕ_R
M	=	One dimensional stiffness modulus
m	=	Stress-level dependency stiffness
P_a	=	Pullout Force
P_C	=	Reinforcement coverage ratio
P_r	=	Pullout resistance
p'	=	Mean effective stress
p'_a	=	Mean effective reference stress
S_u	=	Total undrained shear strength, Trescas failure criterion
S_v	=	Vertical spacing between reinforcement layers

T_{all}	=	Maximum allowed tensile force
T_f	=	Tensile force
T_{ult}	=	Ultimate tensile strength
u_x/u_h	=	Deformations in x-direction/horizontal direction
u_y/u_v	=	Deformations in y-direction/vertical direction

α	=	Inclination angle of failure envelope
γ	=	Unit weight
γ_{sat}	=	Saturated unit weight
γ_{unsat}	=	Unsaturated unit weight
ϵ	=	Strain
ϵ_e	=	Elastic strains
ϵ_p	=	Plastic strains
ϵ_L	=	Lateral strains
ϵ_v	=	Vertical strain
$\delta\epsilon$	=	Change in strain
ν	=	Poisson ratio
ν_{ur}	=	Poisson unloading ratio
ρ	=	Mobilised friction
σ'	=	Effective normal stress
σ_1	=	Highest principal stress
σ'_{lat}	=	Lateral effective stress
σ'_{ver}	=	Vertical effective stress
σ'_{v0}	=	Initial vertical stress
σ'_{h0}	=	Initial horisontal stress
σ_R	=	Reinforcement stress
$\Delta\sigma_3$	=	Change in Lateral stress
$\delta\sigma'$	=	Change in effective stress
τ_f	=	Failure shear strength, Mohr-Coulomb failure criterion
ϕ	=	Friction angle
ϕ_R	=	Friction angle including reinforcement strength
ϕ_p	=	Peak friction angle
ψ	=	Dilatancy angle

Chapter 1

Introduction

Soil is the foundation for many constructions, serving either as support to the structure or used as a construction material and part of the construction itself. Soil and other filling materials have a high capacity in compression but are relatively weak in tension. The soil can be altered to improve the tension capacity by adding another material that increases the tension resistance. This new composite material, with increased strength and tension properties, is termed reinforced soil (Shukla, 2017a).

The use of reinforced soil dates as all the way back to 5000 years BC, where dwellings were constructed using clay or brick reinforced with straw or reeds. Some of the oldest standing constructions in which reinforced soil techniques have been used are the Great Wall of China and the ziggurat in Agar-Quf which are believed to be over 3000 years. The ziggurat of Agar-Quf is constructed with clay bricks, reinforced with woven reed maths. And parts of the Great wall of China is made of a clay and gravel mixture reinforced with tamaric branches. The ziggurat of Agar-Quf with the woven reed maths used as reinforcement can be seen in Figure 1.1. The Romans also incorporated reinforced soil by using both reed and timber embedment's in different constructions (Jones, 1996). The type of soil reinforcement practiced in modern time Shukla (2017a) mentions to be developed by Henri Vidal in the 1960s in the form of metal and steel strips.

In modern practice straw, reeds, wood etc. have been replaced by materials like lime, cement, steel and geosynthetics. The reinforcement can be incorporated as continuous inclusions, placed in a pattern, or randomly distributed in the soil. It is common practice that the reinforcement is placed horizontally or in the direction where the soil experiences undesirable tensile strains. Placing the reinforcement in this desired pattern and orientation is called systematically reinforced soil (Shukla et al., 2009). A discrete distribution of reinforcement provides a more isotropic strength improvement.

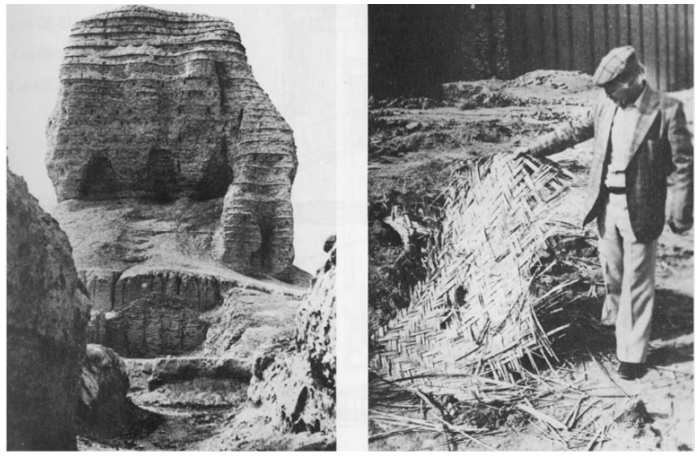

Figure 1.1: The ziggurat of Agar-Quf and the woven reed maths used as reinforcement (Ziegler, 2017)

1.1 Geosynthetics

In the **ASTM D4439**, standard terminology for geosynthetics is defined as: ***"a planar product manufactured from polymeric material used with soil, rock, earth, or other geotechnical engineering related material as an integral part of a human-made project, structure, or system."*** Koerner (2012)

Koerner (2012) lists different types of geosynthetics: geotextiles, geonets, geomembranes, geosynthetic clay liners, geofoam and geocomposites. They have different properties and are used for different purposes. For soil reinforcement purpose geotextile, geogrid and geocomposites are the most common and appropriate ones. The majority of the geosynthetics are made of synthetic polymers, generally characterised as plastic.

Geosynthetics are used in the reinforcement of steep slopes, erosion control, retaining structures, embankments constructed over soft soil, bridge abutments etc. Due to the relatively simple method of construction, Geosynthetic Reinforced Soil (GRS) supporting structures generally have a shorter construction time. Together with the possibility of using local materials, and the relatively common equipment required, it makes the construction costs lower. Establishing an GRS-IBS (GRS - Integrated Bridge System) bridge can potentially reduce the costs with 25-60% compared to traditional methods (Adams et al., 2012). GRS also has environmental benefits due to the use of local materials and reduced use of concrete. The economic and environmental benefits have made geosynthetic a viable option. This thesis will look specifically on the use of geosynthetic reinforced soil in bridge abutments.

1.2 GRS Bridge Abutments

Geosynthetic reinforced soil has been used in bridge abutments in Japan since the mid-90s. There were several GRS bridge abutments constructed, including three railway bridges in Tokyo and some highway supporting structures. In 1995 the Great Hanshin Earthquake struck Japan, measuring as high as 7.2 on the Richer scale. It was observed that the GRS structures were significantly less damaged than the conventional supporting structures. The GRS structures had higher resistance against seismic stress due to its flexibility and relatively large width/height ratio (Tatsuoka et al., 1997).

Several other projects in different countries were constructed in the following years. During the construction of the Vienna railroad embankment in Austria, six bridge supporting GRS structures were incorporated. In Australia, GRS bridge abutments were used in the construction of a major bridge in New South Wales built in 1994 (Wu et al., 2006). In 1996-1997 several full-scale tests were conducted; GRS bridge pier load tests, long-term load test of bridge abutment and bridge piers, and the Black Hawk bridge abutments (Wu et al., 2001). Later, in 1999, a GRS bridge was constructed in Colorado, called the new Founder/Meadow bridge (Abu-Hejleh et al., 2000). In a report from the NCHRP (Wu et al., 2006) six in-service GRS bridges were evaluated, all of them performing satisfactory under service load and being within the criteria for lateral displacements and settlements.

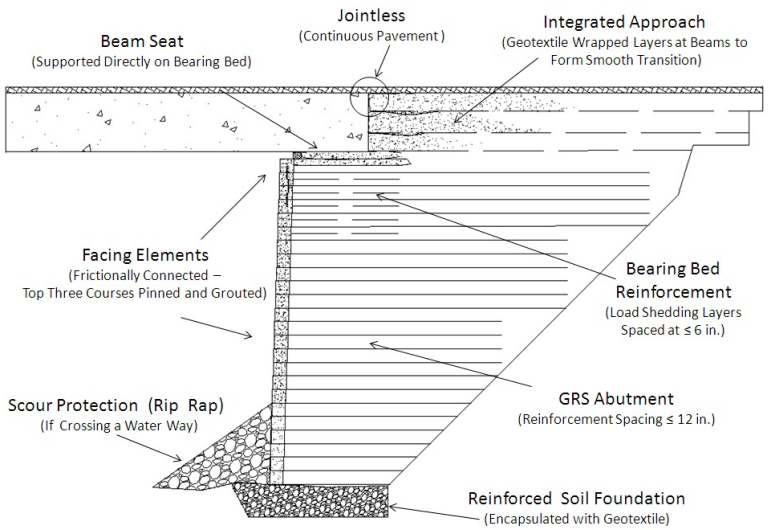

Figure 1.2: Typical cross-section of an GRS-IBS (Adams et al., 2012)

The GRS-IBS used for small, single-spanned bridges have gained popularity, especially in the U.S, due to the lower costs and that it is easy to design and fast to construct. In 2012 the U.S. Department of Transportation, Federal Highway Administration, published an implementation guide for GRS-IBS to meet the demand and secure safe constructions (Adams et al., 2012). A typical design for an GRS-IBS abutment is presented in Figure

1.2.

1.3 GRS Structures in Norway

In the period 1982-1984 three reinforced soil constructions based on the principle of Henri Vidal were built in Norway. The retaining walls and abutments were constructed using steel reinforcements. Some of the first supporting structures using geosynthetic reinforcement were built in Oppland 1983, designed as a gravity wall (Stokkebø, 1989). The most common use of GRS in the Nordic countries today is to reinforce steep slopes and gravity walls with a front consisting of stones, blocks/concrete or a green vegetation.

Reinforced slope walls have been constructed using geogrids near Skedsmo in 1987 (Fannin et al., 2014). A 13 m high, 60 degrees steep reinforced slope was built in Lillehammer in 1993, using geotextiles as reinforcement (Vaslestad et al., 1996).

The first GRS abutment bridge in Kråkstad, Norway was built in 2017. It is a 2 meter wide pedestrian bridge, with a span of 12 m, crossing a river (Vaslestad and Anthi, 2017). The bridge is pictured in Figure 1.3.

Figure 1.3: Kråkstad pedestrian bridge, constructed using GRS abutments (Vaslestad and Anthi, 2017).

1.4 Objectives

The infrastructure in Norway has manychallenges due to soft subsoil, mainly related to bearing capacity and settlements. When constructing a bridge with GRS abutments, the subsoil must have high enough bearing capacity and stability for the structure. A common solution for constructions with subsoil of lower capacity and strength is piling. GRS structures are not a suitable choice to combine with piles, and thus the ground conditions must

be sufficient in itself to establish the abutment. The total settlement and deformations in the abutment depend on the subsoil as well as the design of the abutment.

This thesis looks further into deformations of the reinforced soil and subsoil. Strains and forces in the geosynthetic are analysed together with deformations. Evaluations are made based on data from existing, long-time monitored structures, combined with numerical analyses. A real potential case, where a GRS bridge abutment could be a possible solution, is analysed using the approach calibrated with the existing cases

1.5 Approach

Two long-term monitored slopes located in Norway are modelled in the finite element program PLAXIS 2D. The monitoring data are used as calibration tool, to make the results of the models as close to the measurements as possible. The aim is to get a realistic modelling approach, behaving as close to a real reinforced structure as possible.

After the two existing slopes are modelled, a potential GRS bridge abutment is designed and modelled. The approach from the experience of modelling the slopes is further adapted to the GRS bridge abutment. The results of the finite element modelling are evaluated by looking at the behaviour of the structure. Deformations of the structure and subsoil, as well as strains and forces in the geosynthetic reinforcement are analysed. The results are compared to the calibration cases, expected outcome based on literature and requirements from guidelines.

1.6 Structure of the Report

- Chapter 1: Introduction

  The chapter gives a brief introduction to reinforced soil, the application in bridge abutments, and the use of GRS structures in Norway. Objectives and approach of this thesis are presented.

- Chapter 2: Literature study

  In this chapter, the background of geosynthetics, the mechanisms working in reinforced soil and the conventional approach of design for GRS structures are described. Further there are some relevant theory behind soil modelling, FEM and FEM analysis in geotechnics, and FEM program PLAXIS 2D presented.

- Chapter 3: Modelling Monitored GRS Slopes in Norway

  This chapter describes the background of the modelled calibration cases, the modelling approach and assumptions made. Results are presented and discussed; conclusions found.

- Chapter 4: Modelling of Potential GRS Bridge Abutment

  The background, design and modelling approach of the GRS abutment is described in this chapter. The results are presented and discussed.

- Chapter 5: Summary and Conclusion

  Results and discussions of the slopes and the GRS Abutment is summarised. The main conclusions from the work are presented.

- Chapter 6: Further Work

  Recommendations of improving points, and how to further explore this question are described in this chapter.

Chapter 2

Literature study

2.1 Geosynthetics

There is a variety of different type of geosynthetics aimed for different purposes. Koerner (2012) lists the most common geosynthetics and their primary field of application, Table 2.1. Geotextiles, geogrids and geocomposites are suitable for use in reinforced structures.

The vast majority of these products are made by synthetic polymers. The ones commonly used in geotextiles in geogrids are polyester (PET), polyethylene (PE), polypropylene (PP), polyamid (PA) and high-density polyethylene (HDPE) (Shukla, 2002).

2.1.1 Types of Geosynthetics

Geotextiles

Geotextiles are textiles woven of synthetic fibres by standard weaving machines to a flexible and porous fabric, or matted together in a random pattern, or even knitted. The material is porous, and liquid can flow through them to a various degree. Geotextiles have many different areas of application, see Table 2.1.

Type of Geosynthetic	Separation	Reinforcement	Filtration	Drainage	Containment
Geotextile	X	X	X	X	
Geogrid		X			
Geonet				X	
Geomembrane					X
Geocomposite	X	X	X	X	X

Table 2.1: Different types of geosynthetics and their primary function

The polymers are made by melting the material and forcing them through spinners, resulting in fibres. The fibres harden trough cooling and are stretched during or after the hardening process. When stretching the material, thereby reducing the diameter, the molecules in the fibres arrange themselves so that the material becomes more persistent. This results in increasing strength, decreasing elongation at failure and increased stiffness modulus (Koerner, 2012).

The different types of fibres can produce a range of geotextiles: Woven geotextiles, made by weaving polymeric yarns (multi- or monofilament) into a regular textile. Non-woven geotextiles, where the fibres are bonded by partially melting, needle-punching or chemically binding. The fibres can be structured or randomly oriented. Knitted geotextiles, made by knitting the fibres/yarns together and stitch-bonded geotextiles where the fibres/-yarns are stitched together. The properties of the geotextile is affected by the choice of process. The different types of geotextiles are pictured in Figure 2.1

Geogrid

Geogrid is a mesh or net extruded from polymeric materials, consisting of intersected tensile-resistant elements called ribs, joint in intersections. It has high strength and stiffness modulus, making it suitable for use in reinforcements (Koerner, 2012).

Geogrids are often manufactured using HDPE or PP as polymers. HDPE are used for the unidirectional geogrids and PP for the multidirectional ones. It can be made by either extrusion, bonding or interlacing/weaving the material (Shukla, 2017a).

When using the extrusion technique, it starts with a sheet of the chosen polymer with a thickness of 4-6 mm. After that a regular pattern of holes are punched in the sheet and drawn. The stretching can be uniaxial, biaxial or triaxial and are performed under controlled temperatures and strain rates. The aim is to allow free flow of the molecules into an elongated and isotropic condition while avoiding fractures. The draw process increases the material strength, stiffness modulus and reduces the creep sensitivity. Uniaxial geogrids have much higher strength in the longitudinal direction compared to the transferal. Biaxial geogrids have equal strength in both directions in the plane and triaxial geogrids have almost equal strength in all directions (Shukla, 2017a).

Geogrids can also be manufactured by high-tenacity polyester yarns, woven together by intertwining the perpendicular ribs. Bonded geogrids are when the rods and straps of the geogrid are joined by welding or using laser on the intersecting parts (Koerner, 2012). The different types of geogrids can be seen in Figure 2.2.

Geocomposite

Geocomposites are product composites of two or more materials, where at least one is a geosynthetic. The properties of more than one material can be used. It can be more efficient to combine materials for specific purposes than using them separately (Shukla, 2017a).

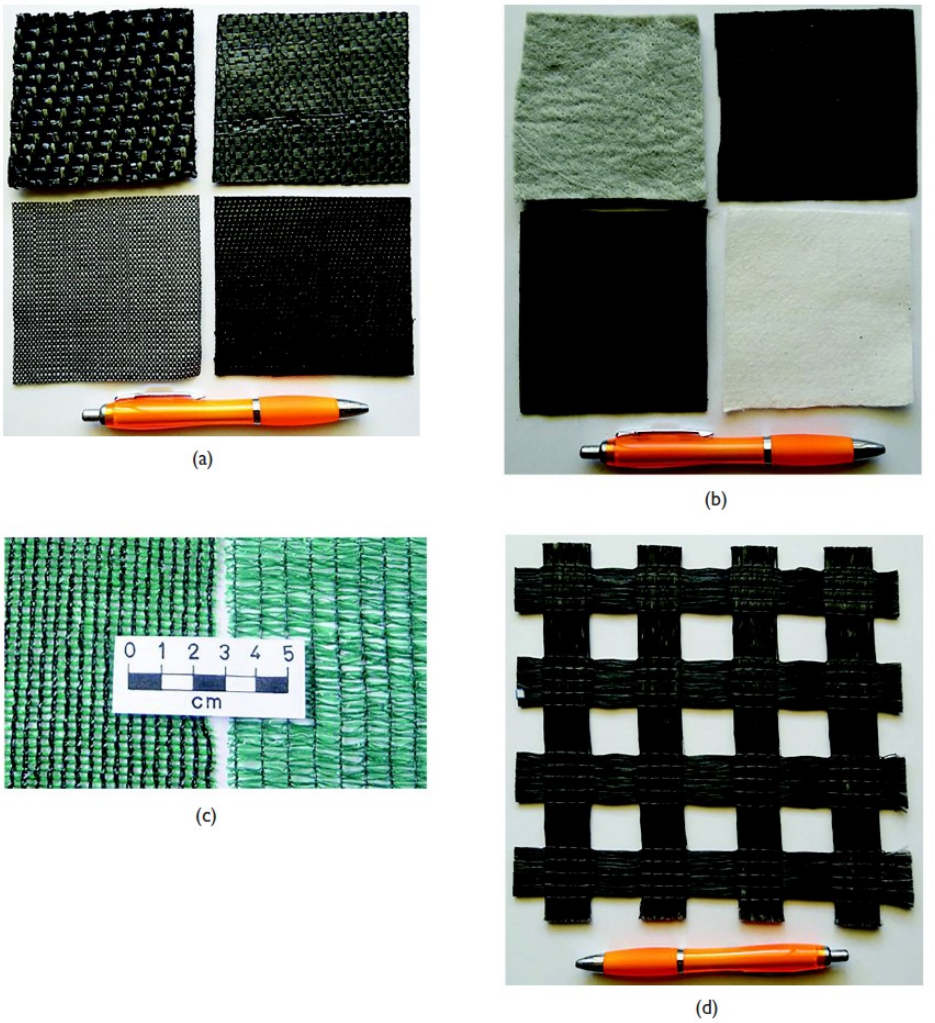

Figure 2.1: Different types of geotextiles: a) woven geotextile, b) non-woven geotextile, c) knitted geotextile and d) stitched geotextile form (Shukla, 2017a)

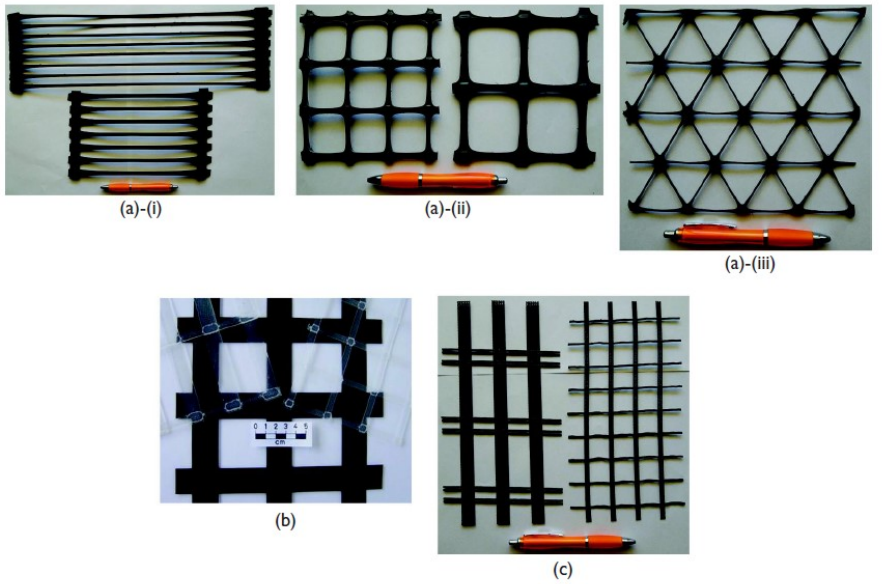

Figure 2.2: Different types of Geogrids: a) Extruded geogrids - (i) uniaxial, (ii) biaxial, (iii) triaxial; b) bonded geogrids, c) woven geogrids (Shukla, 2017a).

2.2 The Mechanisms of Reinforced Soil

Reinforced soil is a composite material consisting of soil and the reinforcement material. The reinforcement increases the soil's tensile strength capacity and makes it a stronger constructing material, with higher resistance of deformations and tensile failure.

By considering the reinforced soil as a homogeneous, anisotropic material, the basic mechanisms of the reinforced soil can be illustrated by applying the Mohr-Coulomb failure criterion. The Mohr-Coulomb material model assumes linear elastic and perfectly plastic behaviour. The contact between the reinforcement and the soil particle mobilizes frictional forces, adding confining stress and restricting the lateral strain in the soil. Looking at a small cylindrical element, tensile force T_f are induced in the reinforcement and a lateral stress $\sigma_R = \Delta\sigma_3$ compresses the soil mass. The reinforced soil will have higher stiffness and shear strength, illustrated in Mohr-Coulomb by the increase in the failure line. The increase can be characterised by either increase in friction angle ϕ_R or as a constant increase in cohesion c_R. In Figure 2.3 l_u represents the failure envelope of the non-reinforced soil, while l_{RC} and l_{RF} represents the failure envelope of the reinforced soil for the two different reinforcement approaches. For more detailed description, see Shukla (2017b).

Different reinforcement materials have different properties, divided into extensible, for example geosynthetics, and inextensible reinforcements, like steel. McGown et al. (1978) looked into the behaviour of different type of reinforcements, referred to as inclusions, in sand, and how the stress-strain curves were effected. As seen in Figure 2.4, the behaviour

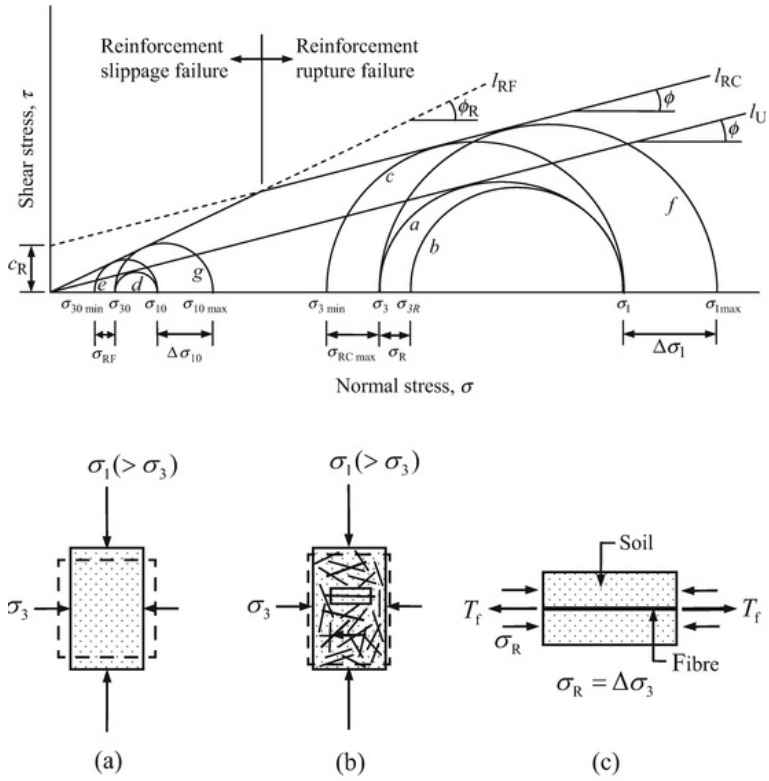

Figure 2.3: Top: Mohr circles for non-reinforced and reinforced soil. Bottom: Forces on soil specimen reinforced and unreinforced soil. (Shukla, 2017a)

of the sand reinforced with extensible inclusions does not fit the ideal linear elastic, perfectly plastic Mohr-Coulomb approach as good as the and reinforced with inextensible inclusions.

2.2.1 Geosynthetic Reinforcements

Geosynthetic reinforcement falls under the category extensible reinforcement, inhibiting greater extensibility and smaller loss of post-peak strength in comparison to inextensible reinforcement. The behaviour of the GRS depends on several factors, Lopes (2002) list the following:

- Soil and reinforcement mechanical characteristics
- Soil-reinforcement interaction mechanism
- Geometry of the reinforced system

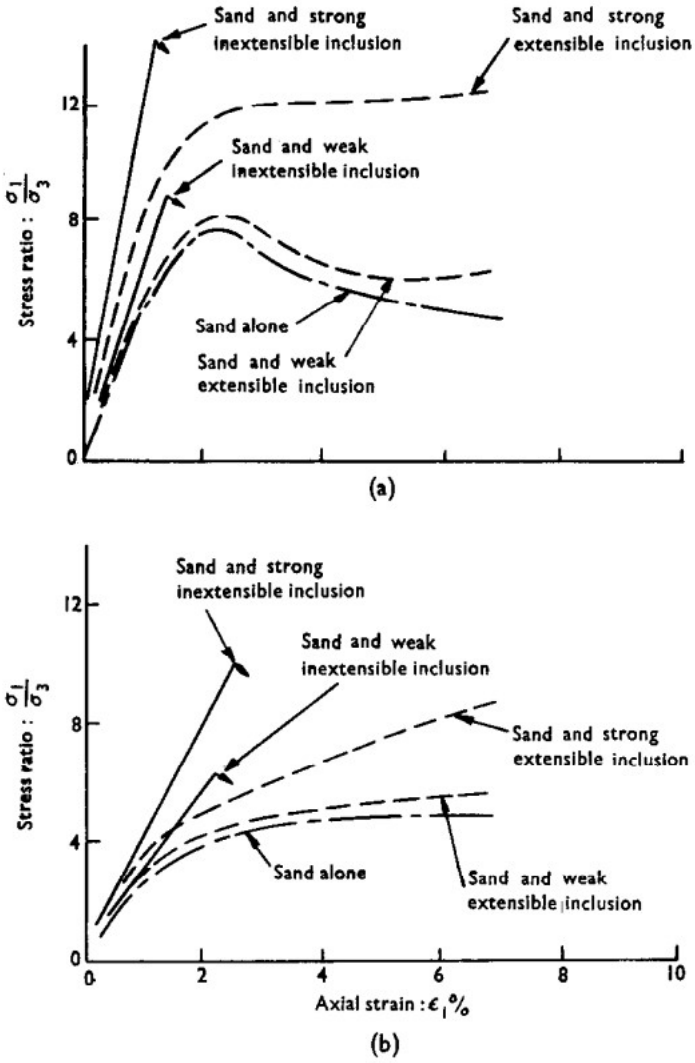

Figure 2.4: Postulated behaviour of a unit cell with and without inclusions: (a) dense sand with inclusions; (b) loose sand with inclusions (McGown et al., 1978)

- Shape, number, location and alignment of reinforcements
- Process of construction etc.

The most crucial factor being the soil-reinforcement interaction mechanisms and properties affecting it. The soil-reinforcement interaction decides how effective the tensile stresses will be transferred from soil to reinforcement, and thus affects the performance and behaviour of the entire reinforced soil. This is highly relevant especially in GRS supporting structures, where the reinforced soil serves as the stability and foundation of a superstructure. The interaction mechanisms can be divided into three parts; reinforcement skin friction, soil-soil friction and passive thrust on the bearing members of the reinforcement (Lopes, 2002). For geotextiles and strips, the skin friction, hence the friction between the soil and geosynthetic material, is the only working mechanism. However, when using geogrids, all the three mechanisms play an active part. The degree of mobilised shear strength depends on the extensibility of the synthetic and whether dilatancy is restricted or not. For example are geogrids less extensible than geotextiles and therefore the mobilisation of shear, and thus increase in soil strength, is higher along the interface.

2.2.2 Stress-Strain and Stiffness

The stiffness and stress-strain behaviour of the reinforced soil depends on the stiffness and frequency of the reinforcement, transfer mechanism in the soil-reinforcement interface and stiffness and compaction of the soil. The lateral stress conditions in the reinforced soil naturally effects the deformation of the structure itself. In addition, deformations in the adjacent soil and soil foundation must be considered.

The confining pressure in the reinforced soil changes stress-strain behaviour, and hence the stiffness modulus M. For one dimensional stiffness modulus M, assuming strain in only one direction, is Eq. 2.1 and in the elastic range Eq. 2.2 (Emdal, 2013).

$$M = \frac{\delta\sigma'}{\delta\epsilon} \tag{2.1}$$

M is the relation between change in stress, $\delta\sigma'$, and strain, $\delta\epsilon$.

From Hook's law and the assumption of one-dimensional strain gives the following expression.

$$M = \frac{\sigma'}{\epsilon} = \frac{E}{1 - 2\nu K'} \tag{2.2}$$

where E is the Youngs modulus for the soil, ν is the Poisson ratio and $K' = \frac{\sigma'_{lat}}{\sigma'_{ver}}$ is the relation between lateral and vertical stresses. With an increase in lateral confining stress, the coefficient for lateral stress K' will be higher and causing increase in stiffness M, see Eq. 2.2. Soil in general does not behave linear elastic and this is a simplified approach of the stress-strain relationship of soil.

Gofar (2008) presents different coefficients of lateral earth pressure for reinforced soil based on numerical studies she performed in 1994. The following empirical expressions were obtained for uncompacted, Eq. 2.3 and compacted, Eq. 2.4 fill in a reinforced wall:

$$K_r = 1.59K_a(f \sin\phi(\frac{E_r}{E_r + S_v E}))^{0.076} \tag{2.3}$$

$$K_{rc} = K_r(1 + 1.1(\frac{\Delta\sigma_{hc}}{q + \sigma_{ovb}})) \tag{2.4}$$

where K_r is the coefficient of lateral stress in reinforced soil, K_a coefficient in the unreinforced soil at active state, f is the apparent friction, ϕ is the soil friction angle, E_r is the tensile modulus of the reinforcement, E is the Young's modulus of the soil and S_v is the spacing between the reinforcement layers. K_{rc} is the coefficient of lateral stress in reinforced compacted soil, $\Delta\sigma_{hc}$ is the compaction force varying with depth, q is the applied compaction load and σ_{ovb} is the overburden pressure varying with depth. The study was conducted on two types of different uncompacted soil with six different reinforcement types (Gofar, 2008).

2.3 Conventional Design of GRS Structures

In the conventional design of GRS structure, stability, deformations, and settlements are calculated separately. The stability analysis is based on the assumption of limit equilibrium state, with the limit defined by the failure criterion. The following section describes the conventional stability analysis approach.

2.3.1 Stability

Stability analysis is performed for both external and internal failure modes. External stability analysis considers the reinforced soil structure as a rigid body and the potential of failure outside the reinforced zone. Conventional methods can be used to check the stability, and the analysis includes calculating bearing capacity, safety against sliding and overturning.

Internal stability analysis takes the failure mechanisms in the soil-reinforcement composite into account.

There are two types of failure conditions in a geosynthetic reinforced soil: pull-out or excessive elongation of the reinforcement or breakage of the reinforcement. Tensile force allowed (T_{all}) in the reinforcement, and pull-out force (P_a) at the soil reinforcement interface described from Gofar (2008):

$$T_{all} = \frac{T_{ult}(CRF)}{F_D F_C F_S} \tag{2.5}$$

where $T_{ult}(CRF)$ is the ultimate strength of the reinforcement, depending on CRF, the creep reduction factor. F_S, F_D, F_C are the reduction factors taking uncertainty of reinforcement strength, construction damage and chemical and/or biological durability into consideration.

$$P_a \leq \frac{P_r P_c}{FS_{po}} \tag{2.6}$$

where P_r represents the available pull-out resistance for the reinforcement. P_r depends mainly on the interaction at the soil reinforcement interface and the reinforcement stiffness. P_c is the coverage ratio and FS_{po} is the required factor of safety against pull-out.

The calculation of the internal stability requires an assumed critical slip surface since it depends on where the highest tensile forces are mobilised. How the failure plane is displayed depends on the type of reinforcement and inclusion of reinforcement. The analysis is mostly based on limit equilibrium concepts and does not take the stress and strain of the reinforced soil into account (Holtz and Lee, 2002). Some methods of modified limit state analysis are presented below.

Critical Slip Surface

Geosynthetics are an extensible reinforcement and for these types of structures reinforced with extensible inclusions, the failure mechanism resembles Coulomb's failure plane. The failure plane starts at the toe of the structure with an inclination angle of $\alpha = 45 + \phi/2$, where ϕ is the internal friction angle of the fill material (Gofar, 2008). It is assumed active stress state (K_a) in the reinforced soil imposed by movement starting at the top of the wall. This is known as Tie-Back Wedge Method, Figure 2.5, introduced by Murray (1980).

Full-scale experiments performed in France, 1974 exhibited maximum tensile strength different from the Coulomb failure plane. The actual failure plane observed, a curved surface, can be approximated by a bi-linear failure plane, indicating that that the movement in the structure is a rotation around the top starting at the toe (Gofar, 2008). This approach is called the Coherent Gravity Method. The stress state changes from rest (K_0) at the top to active stress (K_a) state in the lower parts of the structure (Anderson et al., 2010). The method was originally developed for inextensible reinforcements, like steel.

Another approach is the Two-Part Wedge Method, which uses a search procedure to find the critical slip surface. The method takes all forces acting on the structure into account and gives a picture of the complete mechanism of the reinforced soil. The method assumes the combination of two wedges, see Figure 2.6, one in the reinforced soil and one in the adjacent soil and many possible failure mechanisms are examined. Contribution of the reinforcement is considered as available resistance, making it possible to incorporate facing connection and reinforcement strength (Carrubba et al., 1999).

A paper by Anderson et al. (2010) compares different design methods for reinforced soil. Due to the difference in extensibility in different reinforcement materials, they will exhibit

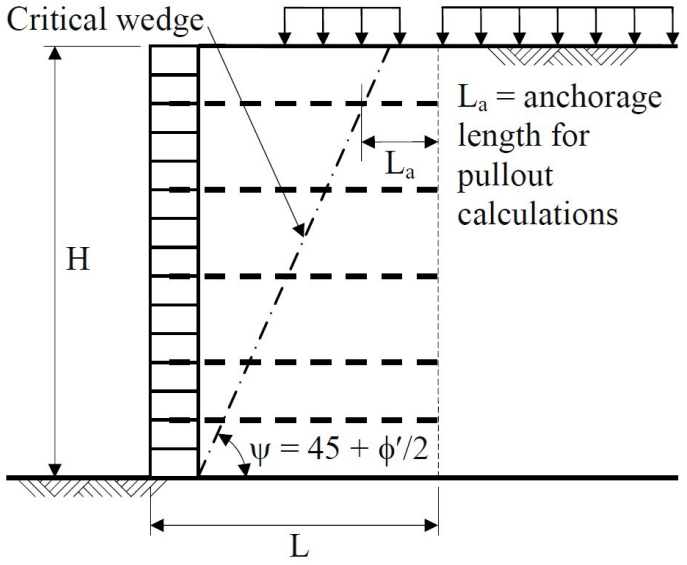

Figure 2.5: The Tie-Back Wedge Method (Carrubba et al., 1999)

different slip surfaces. They argue that soil reinforced with inextensible reinforcement have tension mobilized over the whole reinforcement length, behaving like a coherent gravity mass, while soil with extensible reinforcements does not. In the extensible reinforcement, tension does not distribute over the whole length and maximum tension in the reinforcement will lead to a failure mechanism consistent with the one approximated in the Tie-Back Method. The behaviour of extensible reinforcements, accumulation of tension of the reinforcement and the failure mechanism is demonstrated in Figure 2.7.

2.4 Strains and Deformations in GRS Structures

Adams et al. (2011) and FHWA published a report detailing the foundation of the design guide for GRS-IBS Adams et al. (2012). The report specifies that the vertical strain should be less than 0.5% and that the vertical deformation of the abutment itself is estimated to be the vertical strain multiplied with the height of the abutment. GRS abutments are in general constructed with granular fill, and the majority of settlements in the abutment will occur when the static load is placed before the bridge is opened for use (Adams et al., 2011). The settlements of the subsoil can be found by conventional methods, based on classic soil mechanics theory.

The analytical approach to find lateral displacement of the reinforced soil can be predicted by utilising a method assuming zero volume change in the GRS structure, giving a worst-case estimate (Adams et al., 2011). The method assumes plane strain conditions in a vertical wall, subjected to uniform load. Based on this the maximum lateral displacement,

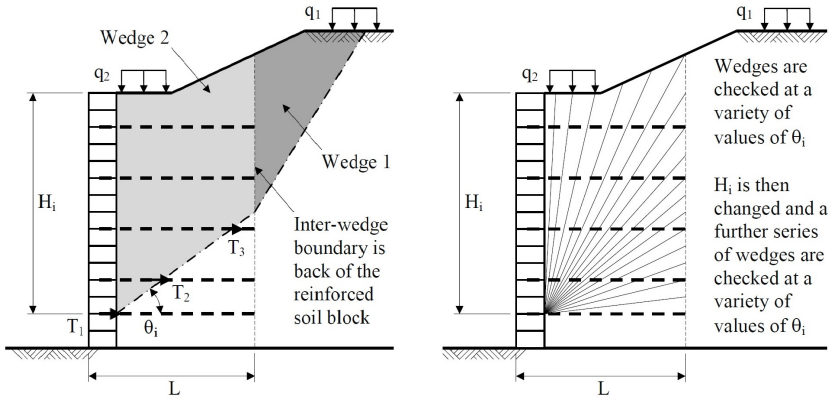

Figure 2.6: Basis of Two-Part Wedge Method (Carrubba et al., 1999)

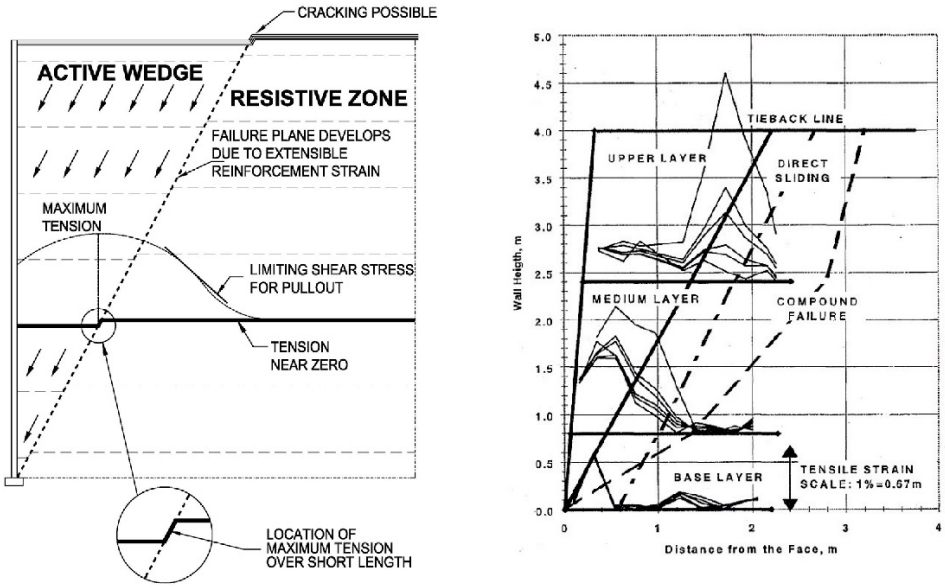

Figure 2.7: Behaviour of extensible reinforcement and tension accumulation in extensible reinforcement from Anderson et al. (2012). The figure to the left further refers to Carrubba et al. (1999).

D_L, is given in Eq. 2.7 and maximum lateral strain ϵ_L in Eq. 2.8.

$$D_L = \frac{2b_{q,vol}D_v}{H} \tag{2.7}$$

$$\epsilon_L = \frac{D_L}{b_{q,vol}} = \frac{2D_v}{H} = 2\epsilon_v \tag{2.8}$$

where $b_{q,vol}$ is the width along the top of the structure, measured from the edge, D_v is the vertical settlement in the GRS mass, H is the height of the structure and ϵ_v is the vertical strain at the top of the structure. The deformations are assumed to appear as a triangular shape in the lateral direction, illustrated in Figure 2.8, and in a uniform vertical direction.

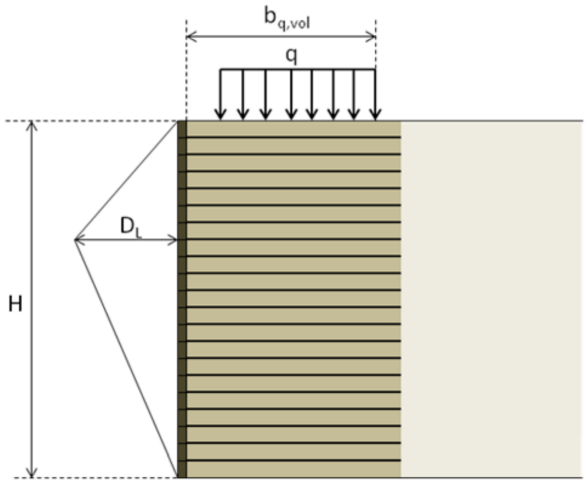

Figure 2.8: Lateral deformations in a GRS structure (Adams et al., 2012)

A thesis reviewing a short-term monitored GRS-IBS in Louisiana compared predicted settlements, approximated with the method, to the monitored results (Saghebfar et al., 2017). They found the vertical settlement of the abutment to be higher at the centre than at the corners. 70% of the total vertical deformations were due to settlements in the foundation soil and the remaining 30% where deformations in the GRS structure itself. Maximum vertical strain measured in the abutment were 0.2%. The theoretical values under predicted lateral displacements and strains in the facing of the wall, calculated from Eq. 2.7 and 2.8, compared to the measured results.

The Nordic guide for reinforced soil, Rogbeck et al. (2006), states that vertical settlements can be approximated with conventional methods based on effective stress and stiffness modulus. The horizontal deformations in GRS walls and abutments are predicted to $0.1\% - 0.3\%$ of the structure height.

The Norwegian road authorities have general requirements regarding roads and bridge abutments. Looking into general guidelines, the total settlements should not exceed 0.5 meter over the course of 40 years after the construction is finished (Vegdirektoratet, 2021, Req. 1.81). The differential settlements between the abutments and the adjacent soil should be zero, and if this is not possible, a transitioning plate should be used (Vegdirektoratet, 2021, Req. 1.82). In a publication for NCHRP, Wahls (1990) sets the maximum tolerable movement for a bridge abutment to 100 mm vertically and 50 mm horizontally after the end of construction.

For the geosynthetic reinforcement, the total strains must be lower than 5% for the lifetime of the construction and lower than 2% after construction is finished (Vegdirektoratet, 2018). Deformations due to creep in the reinforcement should normally not be larger than 2% (Rogbeck et al., 2006). Strains lower than 2% will insure long-term performance and serviceability (Adams et al., 2012).

2.5 GRS Bridge Abutments

2.5.1 Factors Affecting Design of GRS Bridge Abutment

Wu and Ooi (2015) investigate factors affecting the design of GRS for load bearing applications. They look into the effect of embedment length, reinforcement pullout, eccentricity, lateral earth pressures and connection strength and reduction factors. The focus on conventional design issues for load bearing structures, such as rigid- and Geosynthetic Mechanically Stabilized Earth (GMSE) and how they can be applied in GRS design. The main difference in GMSE and GRS is that the reinforcement acts as a tie-back system holding the structure in place in the GMSE structure, but in the GRS wall it only improves the properties of the stabilised soil itself, only providing internal strength.

Looking at embedment length, 0.6 - 0.7H is commonly used in design. Reinforcement lengths down to 0.3 to 0.4H are shown to be stable. Although reinforcement should have a length greater than 0.5H when subjected to heavy loads such as bridge abutments. Truncated base can be an option if the cost of uniform reinforcement is too high (Wu and Ooi, 2015). In the GRS-IBS Interim Implementation Guide by Adams et al. (2012) the reinforcement length in a slope with truncated base should be at least 0.3H at the bottom and 0.7H at the top. The reinforcement should follow the cut at the back of the slope and at slopes flatter than 1:1, reinforcement length larger than 1H is not needed (Adams et al., 2012).

Since the GRS structure serves as a composite, and the length of the reinforcement is dictated by external stability, it is stated that pull-out of the geosynthetic reinforcement theoretically is not an issue and doesn't appear to a probable failure mode. The pull-out stems from the designing of GMSE walls, where the reinforcement act as a tie back, and holds the structure in place. This is not the design concept of GRS structures (Wu and Ooi, 2015).

Eccentricity is a conventional design criterion used in design with rigid elements to prevent overturning. The GRS structure cannot be considered as a rigid element since it behaves more like a flexible element and bending moment does not transfer in the same way. The safety factor against overturning typically is high in GRS structures. It is argued that the bearing capacity check is enough, since the bearing capacity decrease with increasing eccentricity, the eccentricity will be limited because of the requirements for the bearing capacity.

Lateral stress in a GRS is affected by compaction-induced stress and the confining effects of the reinforcement. The facing stress of the GRS is additionally affected by the movements of the facing, especially if the facing has low connection strength. Comparing

unreinforced soil with reinforced soil, the lateral stress is higher in the reinforced soil. The theory estimating the lateral pressure on the face of the reinforcement based on the soil shear strength, reinforcement spacing and soil unit weight, indicates that increasing vertical load in the GRS abutment will increase the lateral stresses (Wu and Ooi, 2015)

Vertical capacity of the footings of GRS abutments are estimated using the W-equation. Several studies conclude that the spacing of the reinforcement has a much greater contribution to strength improvement than the strength of then reinforcement itself (Adams et al., 2011, 2007). The strength of the reinforced soil is based on the Mohr-Coulomb criterion, where an increase in confined stress, $\Delta\sigma_3$ will lead to an increase in σ_1 and thus shear strength. $\Delta\sigma_3$ can be expressed as the tensile strength of the reinforcement per unit wall length, T_f divided by the spacing area S_v per unit wall length.

Since the relation between the two is not linear, and the impact of S_v has a higher influence on the strength, the W factor is applied.

$$\Delta\sigma_3 = W\frac{T_f}{S_v} \tag{2.9}$$

The W factor is a semi-empirically equation:

$$W = 0.7^{\frac{S_v}{6D_{max}}} \tag{2.10}$$

where D_{max} is the maximum particle size of the fill material.

The conclusion is that the W-equation is important when estimating the capacity of the GRS structure, based on the fact that the capacity was in general overestimated when not using the W-equation, compared to the measured capacity.

Finally, Wu and Ooi (2015) investigated reduction factors, related to long-term design of GRS supporting structures: long-term degradation, construction damage and creep.

Studies have indicated that long-term degradation of geosynthetic reinforcement seems to be very small (Elias, 2001; Wu and Ooi, 2015). Experiments cutting the reinforcement into pieces did not affect the movement of the structure until severe cutting close to the facing. This is in line with the concept of the GRS, which aims to increase strength and stiffens, and not act as external support. The cutting of the reinforcement can be compared to an extreme case of degradation, indicating that long-term degradation is not a design problem in GRS structures.

Installation damage does not seem to have a large effect on the load-strain behaviour of the geosynthetic reinforcement, and the effect seems to be limited. It is also indicated that installation damage does not notably affect the creep strains (Allen and Bathurst, 1996).

The creep strain of a GRS structure is restrained to the material deforming the fastest, due to the soil-reinforcement interaction. However, results from field measures indicate that creep deformations are not a design issue when well-compacted granular fill is used in the construction (Wu and Ooi, 2015).

2.6 Soil Modelling Theory

2.6.1 Finite Element Method in Geotechnics

This section describes the basics of numerical modelling in geotechnics and is to a large extent based on the compendium for Geotechnical Engineering Advanced course by Nordal (2020).

Finite Element Method (FEM) is a numerical method of approximation that can be used to solve partial differential equations. It was developed in the mid-50's and is widely used in engineering and science to solve complex discrete problems. The method approximates continuous problems by discretization, and with a discrete number of finite elements the problem can be solved (Zienkiewicz et al., 2013). In geotechnical engineering FEM is used in a similar way as in structural mechanics, applying a method called the displacement method. The displacement method implies subjecting a soil body or structure to loads and forces and thereafter observe the response of deformations and displacements (Nordal, 2020). The displacement method can be adapted and applied for a number of different analyses: Static structural mechanics, dynamic problems, fluid flow, heat flux and coupled problems. When calculating extent of deformations and settlements in soil bodies and structures due to applied loads, the displacement method can be used.

The difference between FEM and traditional analyses in geotechnical engineering is that the traditional methods are based on the limit equilibrium methods. The method is based on the equilibrium state where the limit equilibrium is defined by a failure criterion. This is for example used in calculation of bearing capacity, slope stability, pile capacity and earth pressure, and defines the strength of the soil. Limit equilibrium calculations only take the limit state into account, looking into how much of the capacity in the soil has been used. It does not include deformations and settlements of the soil body, which is calculated separately. In the FEM analysis the failure load and deformations are connected and calculated at the same time. The load is usually applied in increments with corresponding increase in calculated deformations. Failure occurs when the deformations become "unlimited".

FEM analysis presents approximated solutions, and the accuracy depends on simplifications, assumptions made when modelling the reality, and deviations caused by the approximations in the calculation tool itself. The deviations can be caused by using an element that does not fit the purpose or not having a sufficient meshing. To control the quality of the calculation the following should be checked: element type, density of mesh, extent of soil volume modelled, use of interfaced and check convergent criterion. Inaccuracy caused by coarse mesh or too simple elements will cause too stiff behaviour and underpredict deformations, increasing errors.

The initial definition of the problem has a large impact on how realistic and usable the results of the FEM analysis are. Selecting a realistic and appropriate soil model and representative input soil parameters is very important.

Principles of FEM

When modelling a soil structure/volume with FEM it is divided into elements. The behaviour of each element is defined and connected to other elements by numerical and mathematical integration. The elements form a mesh, covering the whole soil volume and approximated behaviour. Dividing a structure/soil body into elements is called discretization. The elements have different shapes depending on desired characteristics and if the analysis is in 2D or 3D. The elements have a set of nodal points, that describe the deformations of the element. The more nodal points, the more detailed solution to the cost of higher computational power. Nodal points are points on the boundaries, and sometimes within the element that define the element response, such as movements and deformation, see Figure 2.9.

A FEM program often operates in the following process: Starting with the modelling of the elements for the object. A stiffness matrix for each element is obtained by numerical integration. The stiffness matrix for all elements is assembled into a large system of equations, the global stiffness matrix. An incremental load vector is found for the global system and the equations for the increments are solved, giving the incremental displacements. The displacement increments can be used to find incremental strains for each element, which in turn gives the incremental stress. The incremental stress is calculated for each nodal point in the element. By integrating the internal soil stresses, the internal force vector is obtained. Accuracy is checked by evaluating the difference between applied external force vector and internal force vector. If the difference does not satisfy the requirement for convergence, the unbalance is too high, meaning adding more iterations and adjusting the load increments will be necessary. The program will loop the process from start until convergence requirement is satisfied. When results are converting, the incremental deformation and stresses from the load step will be added to the total deformations and stresses. The same process will start again for the next load step until specified external load is reached, or failure takes place. It can also be an alternative to use time step analysis instead of load step, it is a similar process with results presented as a function of time.

2.6.2 PLAXIS 2D

PLAXIS is a finite element program developed for geotechnical engineering and can perform both two- and three-dimensional analysis. PLAXIS 2D is the two-dimensional program that can be used to perform stability, flow, and deformation analysis. By assuming plane strain or axisymmetric conditions, depending on the situation, one can approximate the real case. The finite elements used are triangular elements with either 6 or 15 nodes. The 15-node element is default setting in PLAXIS 2D. It is an accurate element which produces high quality stress results for demanding problems. The accuracy of the element leads to a high memory consumption and therefore the simpler 6-node element is available for calculations where lower accuracy is sufficient. Illustration of the two elements with nodes and corresponding stress points is presented in Figure 2.9.

In addition, different elements are used for different structures, such as plates, geogrids, walls etc. and interface elements to simulate the soil-structure interaction.

Geogrids and geotextiles are structures that can resist tensile forces but cannot withstand

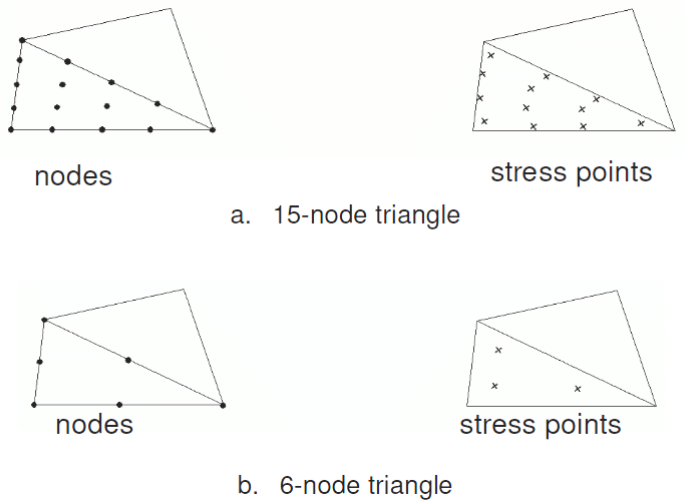

Figure 2.9: Positions of nodes and stress points in the two elements (PLAXIS, 2021a)

compression and obtains no bending stiffness. To simulate geogrids and woven textiles, Geogrid elements are used. The elements are simulated as lines with two degrees of freedom u_x and u_y at each node. To be compatible with the 15-node soil element, each line element has 5-nodes, or 3 nodes in the case of 6-node soil element. Nodal points and stress points coincide, and the axial forces are obtained from the stress nodes (PLAXIS, 2021b).

Interfaces are elements added to get an accurate interaction between two objects. The element is defined by the same number of nodes as the element it is interacting with. The coordinates for the node pairs are identical giving the element zero thickness. The stress points of the interface element coincide with the node pairs, from which the stiffness matrix is obtained (PLAXIS, 2021a).

2.6.3 Constitutive Material Models

To simulate the behaviour of soils and structures, a variety of different constitutive models can be used. A constitutive model aims to describe the response of a material to different types of loads. The reality is often complex, and the models are based on assumptions and simplifications to get an approximation. The models vary in degree of accuracy, with more or less advanced approximations.

The Mohr-Coulomb model may be considered as the simplest approximation of soil behaviour, as it is a linear elastic perfectly plastic model. More advanced material models that includes stress-dependency of stiffness, strain-hardening/softening can give more accurate results. The choice of model depends on the type of analysis and how much information there is about the material modelled. The real behaviour of soil is fairly non-linear when

subjected to stress or strain, and the stiffness of the soil depends on the level of stress and strain in the soil, and also the stress path (PLAXIS, 2021a). This section will describe some of the different soil models and the assumptions and theories behind them.

Linear Elastic model

The linear elastic model is based on Hooke's law. Hooke's law assumes linear proportional behaviour between stress and strain and isotropic elasticity. Elastic strains and deformations are reversible, when the stress is retrieved, the strains and deformations will reverse to its initial state. The stress-strain relationship is described by two parameters, Young's modulus, the stiffness of the material E and The Poisson's ratio ν, describing the volumetric response in the material (Nordal, 2020). The model is not suitable to describe soil behaviour, since deformations in soil are not linearly elastic, but can be used to model other constructing materials such as concrete, plates or soil rocks, where strength properties are high compared to those of soil (PLAXIS, 2021a).

Mohr-Coulomb model

As mentioned above, the Mohr-Coulomb model is a linear elastic perfectly plastic material model, that can be used as a first approximation of soil behaviour. A linear elastic perfectly plastic model, assumes strains, ϵ can be divided into an elastic part, ϵ_e and a plastic part ϵ_p, see Eq. 2.11.

$$\epsilon = \epsilon_e + \epsilon_p \tag{2.11}$$

For the Mohr-Coulomb model the elastic deformations are controlled by Hooke's law, relating the stress rates to the elastic strain. The plastic strains, on the other hand, give permanent deformations. The permanent strains emerge when the strength capacity of the soil reaches the yielding point, hence when state of failure is reached, plastic strains develop. The failure state is defined by the Mohr-Coulomb failure criterion, a mathematical equation describing the strength of a material defined in Equation 2.12 and illustrated in Figure 2.10. The strength of the soil is controlled by the effective normal stress σ', the critical friction angle ϕ, and the attraction, a, in the soil (Nordal, 2020).

$$\tau_f = c + \sigma' \cdot tan(\phi) = (\sigma' + a) \cdot tan(\phi) \tag{2.12}$$

$tan(\phi)$ = friction-coefficient
a = attraction
$c = a \cdot tan(\phi)$ = cohesion

In the Mohr-Coulomb material model the failure criterion, Eq. 2.12, is extended to a general state of stress, so that the criterion is valid in any given plane within a material element (PLAXIS, 2021a). The yield functions in a three-dimensional principal stress space represents a fixed hexagonal cone, Figure 2.11. Stress states within the cone represent elastic

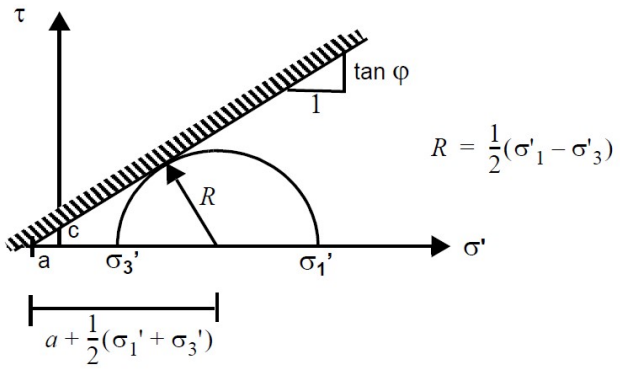

Figure 2.10: Mohr-Coulomb failure criterion in τ - σ' plane (Nordal, 2020)

Parameter	Unit
E Young's modulus	kN/m^2
ν Poisson's ratio	$-$
c Cohesion	kN/m^2
ϕ Friction angle	$^\circ$
ψ Dilatancy angle	$^\circ$

Table 2.2: Basic input parameters in Mohr-Coulomb model

strains, obeying Hooke's law, and stress states at the limit or outside of the cone forms the plastic strains.

When modelling undrained behaviour using total stress analysis, or a combination of total shear strength and effective stress analysis, the failure criterion is reduced to Tresca criterion. The Tresca criterion is based on the total shear strength of the soil, S_u, and is not affected by effective stress state in the soil. The total shear strength however can vary with depth, which PLAXIS takes into account by introducing an inclination parameter, $S_{u,inc}$, starting at a reference y value, and increasing with depth. The modelling of undrained behaviour is described more closely in Section 2.6.3.

Additionally, there is six plastic potential functions defined, incorporating the dilatancy angle ψ, to take plastic volume increase from dilatancy into account. Dilatancy is observed in dense and compacted soils. In cases where cohesion c is larger than zero, the Mohr-Coulomb criterion allows tension in the material. In reality, soil cannot sustain almost any tensile forces. To overcome this, a tension cut-off is specified resulting in three additional yield functions. The yield functions limit the possibility of tensile stresses in the soil. Basic input parameters in the Mohr-Coulomb model, listed in Table 2.2, are E and ν guarding the elastic behaviour, and ϕ, c and ψ determine the plastic behaviour (PLAXIS, 2021a) .

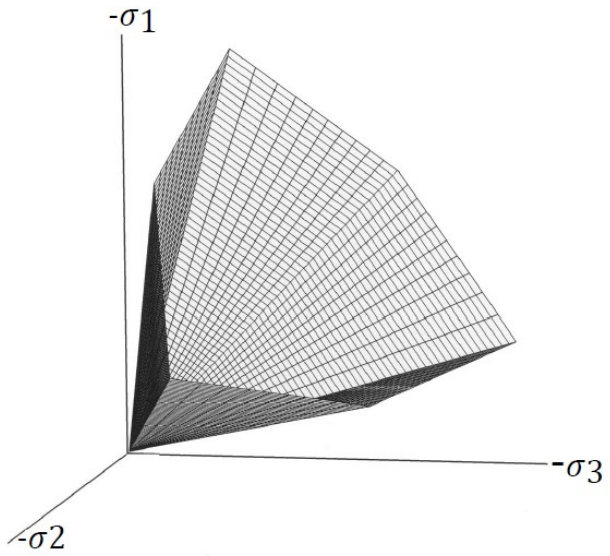

Figure 2.11: Mohr-Coulomb yield surface in principal stress space with $c = 0$ (PLAXIS, 2021a)

The Hardening Soil model

Hardening soil model is a more advanced model, simulating the hardening behaviour soil exhibits when experiencing load and unloading. By combining a stiffness-dependency of the effective stress with shear hardening, controlled by Mohr-Coulomb criterion, and volumetric hardening related to preconsolidation (Nordal, 2020).

In a model with hardening plasticity, the yield surface is not fixed in a principal stress space as in an elastic perfectly plastic model like the Mohr-Coulomb model. The yield surface can expand because of plastic straining. There is two main types of strains causing the hardening behaviour; plastic strains due to primary deviatoric loading is modelled as shear hardening, and plastic strains due to compression and isotropic loading is modelled as compression hardening (PLAXIS, 2021a).

The Hardening soil model is an elasto-plastic model with isotropic hardening guarded by two plastic yield surfaces, called 'cone' and 'cap'. The 'cone' is the yield surface following Mohr-Coulomb criterion using mobilised friction tanρ. As the load increases, the cone gradually expands, inducing plastic strains controlled by the increase in the mobilised friction tanρ, see illustration in Figure 2.12. The gradually increasing plastic and elastic strains towards failure are described by a hyperbola, accelerating as failure approaches, illustrated in Figure 2.13. As the soil is unloaded the cone will stay in its outer position and all the stress states within will become elastic. Elasto-plastic stiffness is described by the secant E_{50}^{ref} of the hyperbola and unloading stiffness E_{ur}^{ref}. The unloading, which is elastic, is stiffer than the loading due to the presence of plastic strain during loading, and E_{ur}^{ref} in the range of $3E_{50}^{ref}$ is used as default parameter for sand. Poisson's unloading ν_{ur} is often chosen in the range of 0.1 to 0.2 (Nordal, 2020). Soil dilatancy is related

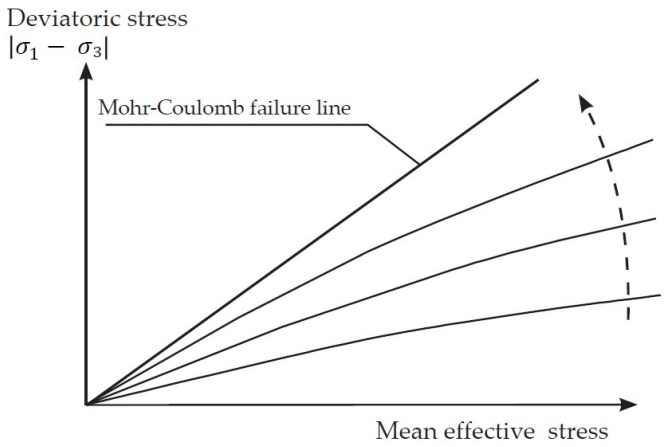

Figure 2.12: The expansion of the cone in Hardening Soil model (PLAXIS, 2021a)

to the yield cone in hardening soil model and affects the development of plastic strains. The dilatancy angle is set to vary with degree of mobilisation and becomes equal to ψ at failure.

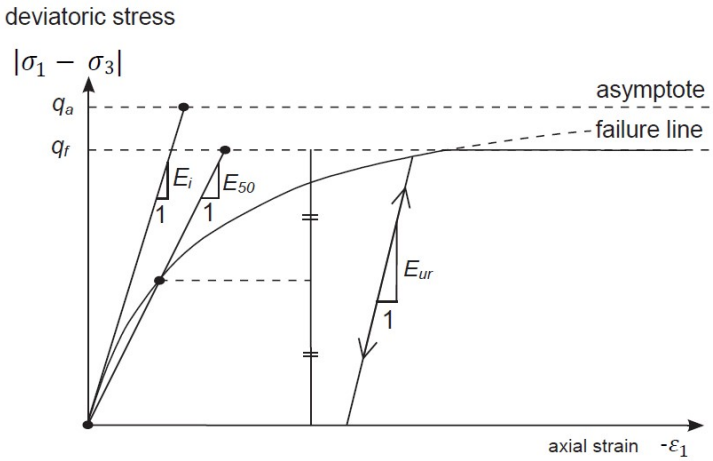

Figure 2.13: Hyperbolic stress-strain relation in primary loading for a standard drained triaxial test (PLAXIS, 2021a), illustrating the stiffness of the different loading conditions.

The 'cap' yield surface is controlled by the pre-consolidation stress. When loading up to effective mean stress p' at the preconsolidated level, strains are elastic. Loading further than preconsolidation level, p' will increase and plastic volumetric strains will develop, and the cap is pushed further out. This behaviour can be observed in oedometer test where the behaviour of the soil is stiffer in the over-consolidated range and softer in the virgin

load range. The stiffness for the soil inside the cap is described by E_{oed}^{ref}. The 'cone' and 'cap' yield surfaces are illustrated in Figure 2.14.

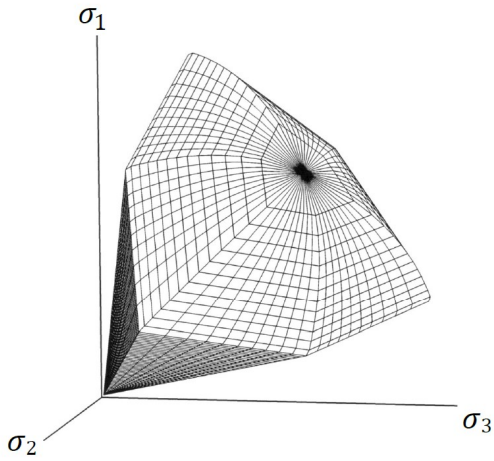

Figure 2.14: Yield surface in hardening soil model (PLAXIS, 2021a)

$$E_{50} = E_{50}^{ref}(\frac{\sigma_3' + a}{p_a' + a})^m \tag{2.13}$$

$$E_{ur} = E_{ur}^{ref}(\frac{\sigma_3' + a}{p_a' + a})^m \tag{2.14}$$

$$E_{oed} = E_{oed}^{ref}(\frac{\sigma_1' + a}{p_a' + a})^m \tag{2.15}$$

The stiffness parameters are dependent on the effective stress level with the reference pressure connected to a reference stiffness. Default reference pressure is $p_{ref} = 100kPa$. The input parameters are the reference values and index parameter m, with $m = 0.5$ for sand and $m = 1$ for soft soil normally (Nordal, 2020). Equations expressing the different stiffness parameters are described below in Equations 2.13, 2.14 and 2.15. Basic input parameters for the Hardening soil model are listed in Table 2.3.

Modelling Undrained Behaviour

Undrained behaviour appears when a saturated soil with low permeability, typically clay, experiences rapid loading or unloading, and the water in the soil cannot dissipate. Excess pore pressure builds up as a result and affects the strength and stiffness behaviour of the soil. In cases where permeability is low, the rate of loading is high or the short-term behaviour are investigated, it is relevant to look at the undrained behaviour. Undrained situations are commonly analysed with a total-stress approach, with the undrained shear strength as guarding Trescas failure criterion. This is usually a realistic approach when analysing the strength and failure envelope of the soil but can have some disadvantages

Parameter	Unit
m Power for stress-level dependency of stiffness	-
E_{50}^{ref} Shearing stiffness	kN/m^2
E_{ur}^{ref} Unloading stiffness	kN/m^2
E_{oed}^{ref} Volumetric stiffness	kN/m^2
c Cohesion	kN/m^2
ϕ Friction angle	$^\circ$
ψ Dilatancy angle	$^\circ$

Table 2.3: Basic stiffness and failure parameters for Hardening soil model.

when looking at other parameters. Effective stress conditions seem to dictate soil skeleton behaviour also under undrained conditions, so undrained conditions can be modelled by using the effective stress approach and in addition take excess pore pressure into account. When simulating a gradually change from undrained to drained conditions, this approach is necessary to get a realistic behaviour of the soil. The duration of the undrained phase is governed by the soil permeability, the stiffness of the soil skeleton E_{oed} and the drainage path of the soil (Nordal, 2020).

Undrained analysis is available with three different approaches in PLAXIS, named Undrained A, Undrained B and Undrained C. Undrained A and Undrained B are performed in terms of effective stress analysis and Undrained C in total stress analysis. However, Undrained A is guarded by effective strength parameters while Undrained B and Undrained C are limited by total strength parameters.

Undrained A uses effective stiffness parameters and adds the excess pore pressure in the soil. Excess pore pressures are generated due to small volumetric strains obtained during plastic calculation in addition to assuming a very low compressibility of pore water. The effective strength parameters are used to model the undrained shear strength in the material. The development of pore pressure controls the effective stress path, and it leads to a realistic value of undrained shear strength at failure (PLAXIS, 2021b). Most soils cannot provide the right effective stress path, and for the Mohr-Coulomb model one should have in mind that the model can over-predict the shear strength of the material. Undrained A is well suited to use when analysing undrained conditions changing into drained conditions.

Undrained B gives direct control over the undrained shear strength parameters and combines these with effective stiffness parameters. Calculations are performed as an effective stress analysis, but with the undrained shear strength controlling the failure criterion. The less advanced model, like Mohr-Coulomb that are linearly elastic perfectly plastic, struggles with generating the correct porewater pressures. This may lead to incorrect calculations of deformations and structural forces. It is not suitable to apply consolidation analysis after undrained analysis when this model is used without updating the shear strength of the soil. Undrained B is suitable to use in failure analysis of the soil in undrained conditions. Undrained C has undrained shear strength and stiffness as input values, performing calculations as total stress analysis. Pore pressures are not generated for this type

of calculations, and it is not suitable to perform consolidation analysis after the undrained calculations, as in Undrained B (PLAXIS, 2021b)

2.6.4 Types of Analysis in PLAXIS

Depending on the case to be analysed, different types of analysis can be chosen, with different approaches. The following section describes some of the analysis types in PLAXIS, with PLAXIS (2021b) used as reference.

To generate the initial stress in the in the soil, an initial calculation is done. The stresses in the soil in the initial stage are defined by the weight of the soil body and stress history. The K_0 procedure is the default initial stage in PLAXIS and is characterised by the initial vertical stress σ'_{v0}. The coefficient of lateral earth pressure, K_0, decides the initial horizontal effective stress, σ'_{h0}.

The K_0 procedure does not see to the equilibrium in the whole stress field, and only takes into account the vertical stresses. This is because the procedure does not generate shear stresses. The approach is therefore not realistic and is less suitable when the initial terrain or soil layer are not horizontal. To calculate the initial stress field in these situations, Gravity loading can be used. Gravity loading initiate stresses based on the volumetric weight of the soil. When the Mohr-Coulomb model is used in the soil during Gravity loading, the horizontal effective stresses are strongly dependent on the Poisson's ratio ν, and therefore it is important to choose a realistic value.

Plastic calculation type provides an elasto-plastic deformation analysis where the change in pore pressure with time is not considered. Calculations are performed with the stiffness matrix based on the undeformed geometry, assuming small deformations. The assumption is applicable to most geotechnical problems and comes as default. The loading of the model can be changed during a Plastic calculation by changing the load and geometry configuration or pore pressure distribution.

When needing to analyse the development and dissipation of excess pore pressure as a function of time, a Consolidation calculation can be conducted. The consolidation calculation uses the permeability for the soil to calculate the dissipation of pore pressure. It can be chosen to be performed over a specific time range, to a specific degree of consolidation or to minimum excess pore pressure are dissipated. However, only the consolidation analysis with specified time allows for changes in the loading conditions during the analysis.

2.7 FEM analysis of GRS strucures

Several studies investigating numerical analysis of GRS structure have been conducted during the last couple of decades (Abu-Farsakh et al., 2019; Ardah et al., 2017, 2021; Helwany et al., 2003; Wu et al., 2014). A lot more have been done on free-standing geosynthetic MSE walls than that of GRS-IBS (Ardah et al., 2021). Helwany et al. (2003) investigated the impact of the foundation soil on the GRS bridge abutment by numerical analysis. They calibrated the program using monitor data from Founders/Meadow GRS

bridge in Colorado (Abu-Hejleh et al., 2000). The results showed that the numerical program used was a reliable tool for analysing performance of GRS bridge abutments. The analysis indicates that the behaviour of the foundation soil has a considerable impact on the performance of the GRS bridge abutments. The aim of the study was to investigate the possibility of reducing the differential settlements between the bridge abutment and the adjacent embankment, known as the bridge bump. The foundation soil ranged from dense sand to medium stiff clay, with the loose sand exhibiting the largest settlement and the stiff clay the smallest settlement. All soil foundations exhibited displacements within a tolerable range for the 6-meter-high abutment (Helwany et al., 2003).

FE analysis of stress-strain behaviour and change in volume for a field-scale geosynthetic composite was conducted by Wu et al. (2014). Field scale tests with closely spaced geosynthetic reinforcement, and corresponding FE analysis exhibits suppression of soil dilation resulting in a stronger soil. The material models used where Soil Hardening model for the soil and Linear elastic model for the reinforcement, with the interface between the soil and reinforcement assumed to be fully bonded. It is pointed out that effect of increased residual lateral stress due to fill compaction needs to be considered in the FE analysis. This is done by simulating a compaction force for each soil lift in a staged construction. The results obtained from the FE analysis exhibited good agreement with experimental data for the stress-strain and volumetric behaviour.

Ardah et al. (2017) used field measurements from the fully-instrumented Maree Michel Bridge in Louisiana to verify the performance of the FE numerical analysis model they developed. The model simulated GRS-IBS system under service load conditions. The height of the abutment was almost 4.8 meter, with a width of 13 meter and the bridge spanning 19.8 meter, with a superstructure width of 9.1 meter. They used FE program PLAXIS 2D (2016), applying hardening soil model to simulate behaviour of the granular backfill, linear-elastic model with Mohr-Coulomb frictional criterion to simulate the interaction between the geosynthetic and the backfill material. The linear elastic model was used for the facing blocks and the geosynthetics and Mohr-Coulomb constitutive model for the foundation soil. The FE simulations predicted lateral deformations with good correlation to the measured values, see Figure 2.15, while the settlement was found to be two times higher than the actual field measurements, probably due to the consolidation caused by the old bridge. The results also showed that the failure envelope of the wall did not coincide with the tie back wedge envelope ($45° + \phi/2$), described in Section 2.3.1, but extended approximately 40 % beyond. All in all, the result from the analysis correlated well with the monitored field measurements, showing that 2D plane strain analysis can be used to predict the performance of GRS-IBS.

Abu-Farsakh et al. (2019) investigated the performance of GRS-IBS looking at lateral facing deformation, reinforcement strain and location of possible failure zone, and how these where affected by different structural parameters under service load. The parameters included span length, height of GRS abutment, refinement spacing and stiffness, and was investigated using FE program PLAXIS 2D (2016). The model was calibrated with the Maree Michel Bridge, as in Ardah et al. (2017). The abutment height caused an increase in lateral deformation due to the increased stress applied in the reinforcement. Length of the bridge span showed a significant effect on the lateral displacement and maximum strain

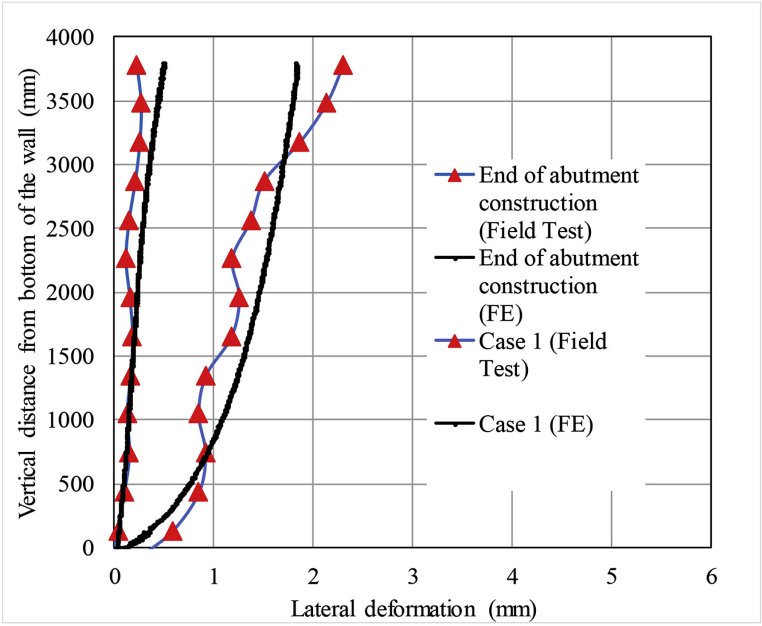

Figure 2.15: Lateral deformations at the front of the wall, FE modelling and experimental values (Ardah et al., 2017)

of the reinforcement but did not change the distribution of the displacement. Spacing of the reinforcement had a high impact on the deformations of the abutment, giving a greater impact than the stiffness of the geosynthetics for reinforcement space at 0.2 meter or less. Ardah et al. (2021) investigated the same case further, since the 2D modelling been done with success in (Abu-Farsakh et al., 2019; Ardah et al., 2017), also looking at the impact on lateral deformation and reinforcement strain, of several different parameters. Results indicated that the internal friction angle of the back fill soil showed to have a significant impact on the structure's behaviour. The failure mechanism of the GRS structure was found to be a combination of punching shear envelope at the top, following the inner edge of the footing, meeting the Rankine failure envelope and following that to the foot of the structure in both cases (Ardah et al., 2021; Abu-Farsakh et al., 2019). The material models used in both analysis where the same as in Ardah et al. (2017).

Furthermore, a numerical 3D study of the Maree Michel Bridge using PLAXIS 3D comparing the results with the 2D simulations and field measurements (Abu-Farsakh et al., 2018). Comparing the two analyses showed little difference in predicted results, concluding that 2D plane strain FE analysis can be used to model GRS-IBS systems with satisfactory outcome.

Chapter 3

Modelling Monitored GRS Slopes in Norway

In this chapter, two existing structures with available monitoring data are modelled. The models are calibrated using the monitored data, with the aim of finding an appropriate modelling approach that can be further used to analyse stability and deformations in structures not yet constructed. The structures, two different geosynthetic reinforced slopes built in Norway during the late 80's and early 90's, have been modelled in PLAXIS 2D. The behaviour of the structures has been monitored over time, looking at lateral displacement in the structure, strains, forces in reinforcement and variations in temperature. The two slopes will be further presented in this chapter, going through properties, conditions, monitored results and assumptions made when modelling the cases. The results from the actual field measurements will be compared with the one obtained from FEM analysis in PLAXIS.

3.1 Reinforced slope Skedsmo

In 1987 a 4.8-meter-high sloped wall reinforced with geogrid was built in Skedsmo, close to Oslo in Norway. The slope wall is located at the toe of an existing hillslope. The structure is 20 meter long, divided into two sections, 10 meter each, with different arrangement and spacing of geogrid reinforcement. The structure has a slope of 1:2, approximately 63 °and the foundation soil consists of a competent gravelly sand. In the modelling of the slope only one of the two sections was chosen, denoted section 'N'. The finished construction is pictured in Figure 3.1.

Uniformly graded clean medium to fine sand, with some traces of gravel, was used as a backfill soil. Characteristics of the sand were: $d_{50} = 0.2$ mm, unit weight $\gamma = 17kN/m^3$ and a friction angle of $\phi_{ds} = 38°$ obtained from direct shear tests (Fannin and Hermann, 1990). In 2013, samples of the backfill in section 'N' were collected and the strength of the material tested with different methods. Drained direct shear tests (DS), triaxial testes

Figure 3.1: Picture of the finished slope with the permanent berm on top (Fannin and Hermann, 1990)

(TX) and plane strain tests (PS) were performed. The results exhibited peak friction angel as $\phi_{p,ps} = 54°$, $\phi_{p,tx} = 42°$ and $\phi_{p,ds} = 40°$. However, the strains obtained from the laboratory shear strength tests compared to the strains measured in the reinforced structure suggest that peak friction angle has not yet been mobilised. There are no available tests of the stiffness and elastic modulus for the soil, these are chosen based on information from PLAXIS (2021a) and Nordal (2020). There is neither any data on the seepage of the soil and in this approximations it is assumed based on the particle-size distribution (Fannin and Hermann, 1990), Hazen's formula and experience-based values (Emdal, 2013). It was found to be between 15 - 20 m/day for backfill soil and around 5 - 25 m/day for the foundation soil. The dilatation angle is estimated on the basis of PLAXIS (2021a) and Nordal (2020), and the characteristics of the material, with a conservative approach.

The reinforcement used in the construction is a uniaxial geogrid, Tensar SR 55. It is a high-density polyethylene (HDPE) grid made by punching of a homogeneous polymer sheet. The geogrid characteristics are (Fannin et al., 2014; Fannin and Hermann, 1990): T_{ult} = 57 kN/m, at peak strain 11.2 %. For long-term performance Tensar SR 55 exhibit a stiffness of 3.5-4.5 $kN/m$for small strains in the range 0.5 to 1.0 % .

Section 'N' has a uniform vertical spacing of 0.6 meter between the 8 layers of reinforcement, constructed with 0.3-meter soil lift. The geogrid reinforcement has a length of 2.2 meter, see Figure 3.2. The soil in each soil lift is compacted to a dry density greater than 92% of the maximum value of Standard Proctor test with a water content of 5-10 %. A lightweight facing was fixed in the geogrid reinforcement, consisting of a steel mesh and a fabric to retain the soil.

When the construction of the slope was finished, a period of 28 days where the self-weight of the structure was the only load followed. During the next 63 days, a surcharge of 29 kN/m^2 was applied in a load-unload cycle by filling up water tanks. Finally, a permanent

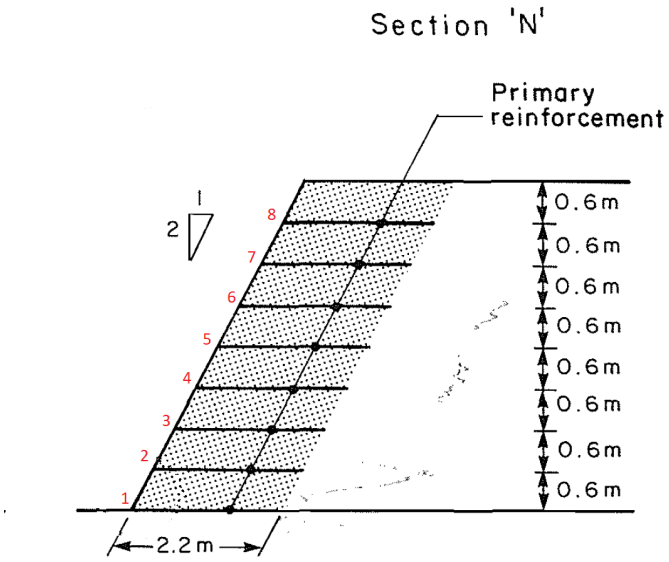

Figure 3.2: Cross-section of 'N' with geogrids numbered 1 - 8, adapted from (Fannin and Hermann, 1990)

surcharge of 49 kN/m^2 was applied, building a 3 meter high berm on top of the slope (Fannin and Hermann, 1990).

3.1.1 Measurements from Monitoring of the Slope

The slope was monitored with force cells and strain coils. The force was measured at one point in each reinforcement layer, in section 'N' they are placed 0.86 m behind the front of the slope. Strain coils are placed at three points for each reinforcement layer. Detailed description of the instrumentation in the slope can be found in Fannin and Hermann (1990). The strains in the geogrid measured during self-weight loading and after applying permanent surcharge can be seen in Figure 3.4. The average strain measured in the coils closest to the front of the slope (0.86 meter behind the face of the slope) was $\epsilon_{0.86} = 0.47$ % at self-weight and $\epsilon_{0.86} = 0.70$ % at permanent surcharge. Average strain in all the 9 measuring points during permanent surcharge is $\epsilon = 0.56\%$.

Tensile force was measured to be an average of 1.76 kN/m during self-weight and 2.49 kN/m at permanent surcharge. Development of measured forces in the geogrid during the first year of construction is presented in Figure 3.3, showing a variation from 1 to maximum 3 kN/m. A summary of average strains and tensile forces in the geogrids for different load situations are represented in Table 3.1 based on data from Fannin and Hermann (1990).

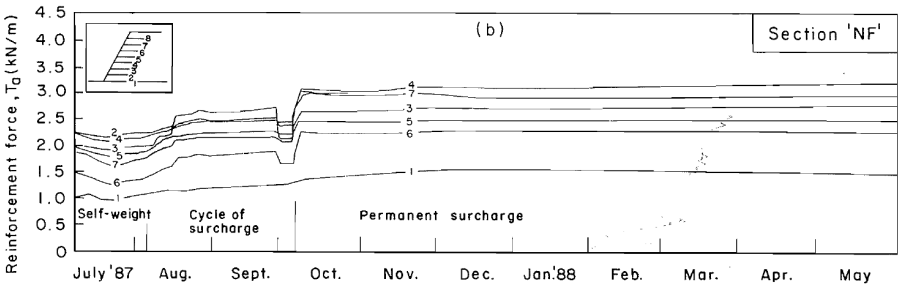

Figure 3.3: Tensile force in the geogrid reinforcement (Fannin and Hermann, 1990)

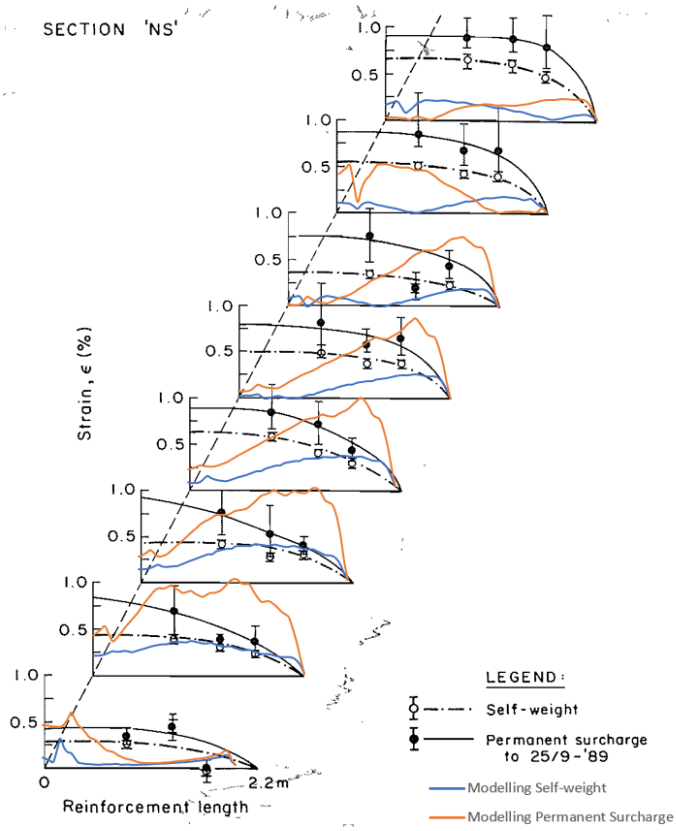

Figure 3.4: Measured strains in the geogrids, interpolated between point (Fannin and Hermann, 1990) plotted with modelled strains.

Loading conditions	Average $\epsilon_{0.86}$(%)	Average ϵ (%)	Average T (kN/m)
Self-weight	0.47		1.76
Permanent surcharge	0.70	0.56	2.49

Table 3.1: Average strain and tensile force in the geogrids, in cross-section A, under different loading conditions.

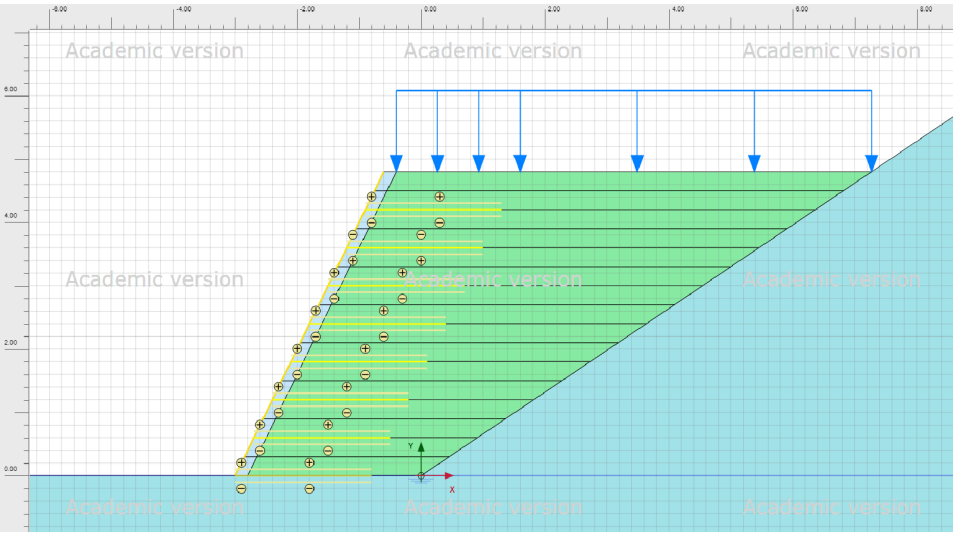

Figure 3.5: Close-up of the reinforced slope in Skedsmo, modelled in PLAXIS

3.1.2 Modelling of the Slope

The slope is modelled in the FEM program PLAXIS 2D, using 15 node elements, fine meshing, and plane strain conditions. The initial existing slope was modelled as 1.5:1, building the reinforced slope at the toe. Since the initial phase in the simulation does not have horizontal geometry, a so-called gravity loading was performed to get realistic initial stresses on the soil (2.6.4). The reinforced soil body was created in stages, with every soil lift of 0.3 meter in a separate stage compacted with a line-load of 15 kN/m. The backfill soil was modelled using Hardening Soil model, to take the load and unloading of compaction force for the sand into account. For the foundation soil, Mohr-Coulomb soil model was used. Since the strains in the geogrids are small, less than 5%, is assumed to behave linearly elastic and perfectly plastic with an axial stiffness of EA = 500 kN/m. Interaction between the soil and geogrid is approached by using an Interface, with Mohr-Coulomb strength and assuming linear elastic behaviour. In the interaction between the soil and the geogrid it is assumed a strength reduction of 0.85 for the interface (TENSAR, 2005).

A summary of the parameters and different material models for the slope is presented in Table 3.2. When all the soil lifts were created, 16 in total, the three stages of loading were simulated. The first stage represents the self-weight of 28 days with no external load on the

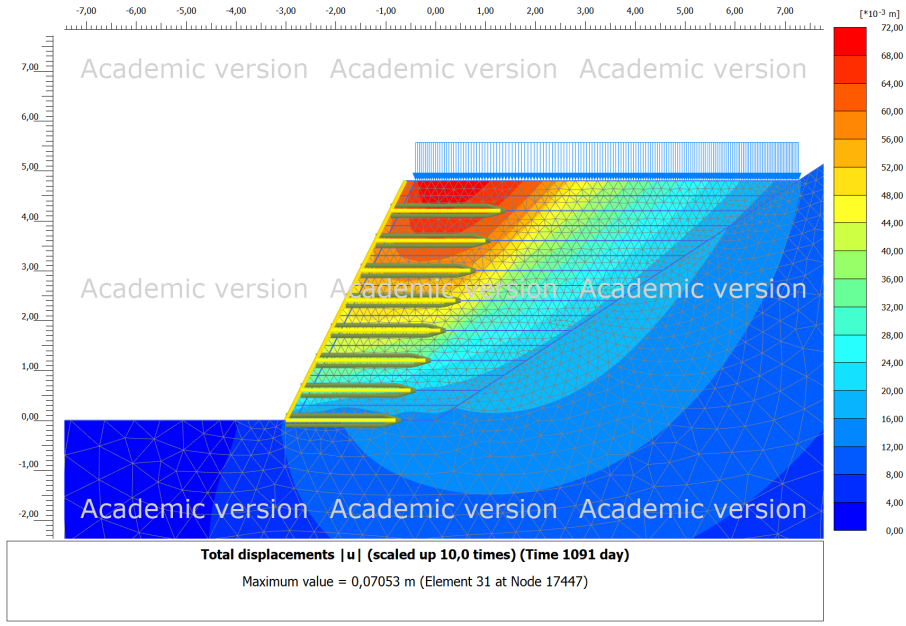

Figure 3.6: Total deformations in the slope at permanent surcharge.

construction, second is the cyclic loading, with a 29 kN/mline load applied on top of the slope for 63 days. Finally, the last stage is the building of the berm, modelled by putting a 49 kN/mline load on top of the structure. The analysis of the slope was performed in drained conditions, since the permeability of the soil is high, this was the most realistic approach. The calculation type is set to plastic, performing elastoplastic analysis in all stages (2.6.4). Consolidation analysis was considered but since the permeability is high in the materials, the build-up of excess pore pressure was assumed to be low and rapidly drained. The boundary conditions of the slope allowed vertical movement but not horizontal movement at the two sides of the model, and the boundary condition at the bottom of the model did not allow horizontal or vertical deformations. The model of the slope can be seen in Figure 3.5. An overview of the whole model is available in Appendix A.

3.1.3 Results Reinforced Slope Skedsmo

The largest deformations in the slope, ca. 70 mm, are present at the top of the slope, about 1 meter behind the front, at the last stage of loading when the permanent berm is built. The deformations decrease vertically from the top, to about 10-15 mm at the bottom, and horizontally behind the front of the slope. Total deformations for the stage of permanent surcharge can be seen in Figure 3.6.

The horizontal deformations and vertical settlements are investigated more closely in a cross-section 0.5 meter behind the front of the slope. The highest vertical deformations

Category	Description
Backfill soil	Hardening soil model Dry and wet unit weight: $\gamma_{unsat} = 17kN/m^3$ $\gamma_{sat} = 18kN/m^3$ Cohesion $c = 3.9kPa$ Friction angle $\phi = 38°$ Dilatation angle $\psi = 8°$ Stiffness parameters: $E_{50}^{ref} = 30,000kPa$ $E_{ur}^{ref} = 90,000kPa$ $E_{oed}^{ref} = 30,000kPa$ $\nu_{ur} = 0.2$ and $m = 0.5$
Foundation soil	Mohr-Coulomb soil model Dry and wet unit weight: $\gamma_{unsat} = 17kN/m^3$ $\gamma_{sat} = 18kN/m^3$ Cohesion $c = 3.9kPa$ Friction angle $\phi = 38°$ Dilatation angle $\psi = 5°$ Stiffness parameter $E = 30000kPa$ $\nu = 0.3$
Interface soil-geotextile	Mohr-Coulomb soil model Cohesion $c = 3.315kPa$ Friction angle $\phi = 32.3°$ Dilatation angle $\psi = 4.250°$ Stiffness parameter $E = 7000kPa$ $\nu = 0.2$
Geotextile	Linear elastic Short time tensile strength $T = 57kN/m$ with a peak strain of 11.2 % $EA = 500kN/m$
Front	Same soil as the backfill soil but with $c = 20kPa$ Geogrid Front with EA = 1000 kN/m

Table 3.2: Modelling parameters for reinforced slope in Skedsmo

in the cross-section emerge at the top of the slope and decrease approximately linearly with depth. The horizontal deformations however are about constant from the top of the slope all the way down to 2 meter height where they start to decrease, approximating zero at the bottom of the slope. The deformations are plotted against the respective height of the slope in Figure 3.7. The largest horizontal deformations are about 37 mm, with an increase of 22 mm from end of construction till permanent surcharge, and the largest vertical deformations 62 mm. The slope itself shows a vertical deformation of 27 mm from the end of construction until the permanent berm is built, and 52 mm from start of construction until the permanent berm is placed. The subsoil accounts for 16-22% of the total vertical settlements. The total displacement at the end of construction is respectively 0.3 % horizontally and 0.7 % vertically, compared to the height of the slope.

The strains in the geogrids are not available as an automatic output result in PLAXIS but are deduced from the deformations in the nodal points on the grids. Average deformations are calculated by using the local, axial displacement at the end nodes of the geogrid, finding the elongation of the grid, ΔL, and dividing it with the original length of the grid: $\epsilon = \frac{\Delta L}{L}$. The strains in the geogrid at self-weight have an average size of 0.14 % and after the installation of the berm, when the structure is under permanent surcharge, it increased to 0.41 %. In Both cases geogrid 2, 3, and 4 from the bottom experience the highest strains and the one at the bottom, grid 1 and at the top, 7 and 8 exhibit the lowest strains. The numbering of the geogrids can be seen in Figure 3.2. Average modelled strains in the grids are presented in the Table 3.3. The continuous strains throughout the geogrids are also deduced from incremental axial nodal displacements in the geogrids and plotted in Figure 3.4.

Geogrid Nr. (Ref. 3.2)	Strain at "Self-Weight" (%)	Strain at "Permanent Surcharge" (%)
8	0.11	0,11
7	0.04	0.27
6	0.03	0.34
5	0.12	0.42
4	0.21	0.54
3	0.28	0.68
2	0.26	0.73
1	0.04	0.18
Average	0.14	0.41

Table 3.3: Strains in geogrids at different load stages

The strain cartesian strain in the soil, ϵ_x was evaluated in a cross section 0.5 meter behind the front of the slope, at permanent surcharge. The maximum measured value exhibited was $\epsilon_{x.max} = 1.5$ % app. 0.5 meter above the bottom of the slope, and the average cartesian strain was $\epsilon_{x.av} = 0.47\%$.

The forces in the geogrids are accessible as a direct output from PLAXIS 2D. The force distribution over the grids is presented continuously in Figure 3.8. The average force in the grids is derived from these values. Average force for all the geogrids is calculated for

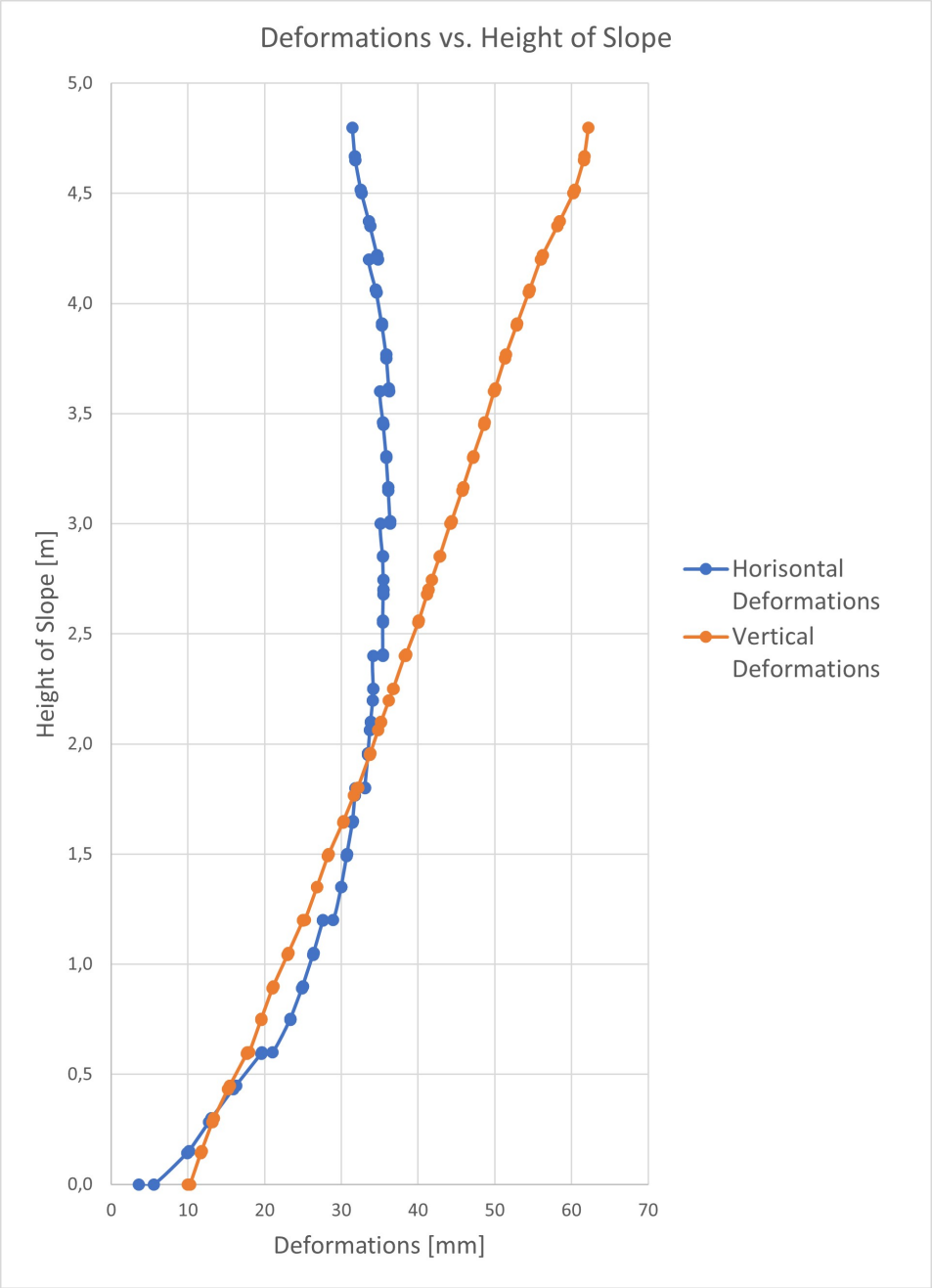

Figure 3.7: Horizontal and vertical deformations in cross-section 0.5 meter behind front, at permanent surcharge, plotted against height of the slope.

the "Self-weight" stage and "Permanent Surcharge" stage. Average force at self-weight in the geogrids is 1.11 kN/m, increasing to 2.71 kN/m at permanent surcharge. As for the strains, geogrid 2,3 and 4 exhibit the highest forces and 1 and 8 the lowest.

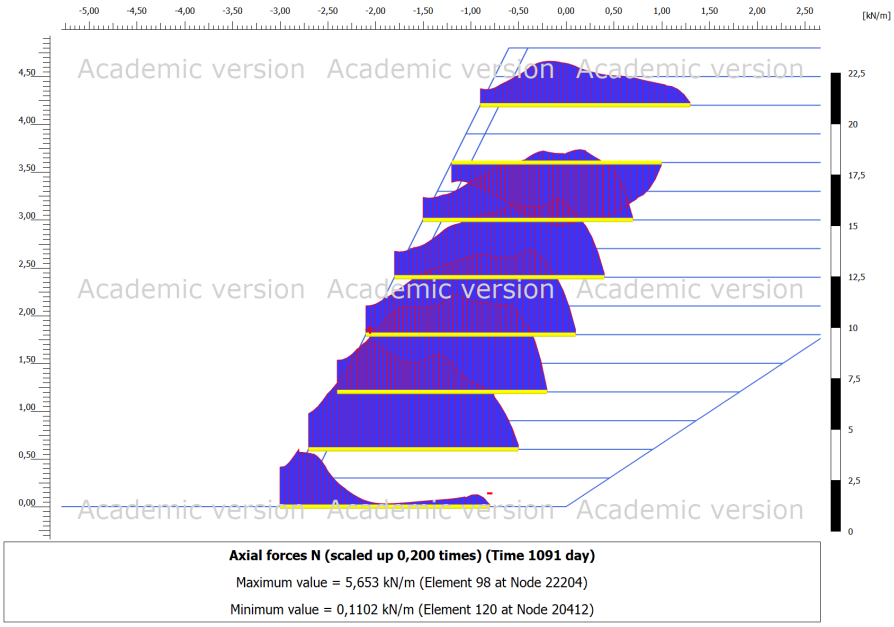

Figure 3.8: Force distribution in the geogrids from output in PLAXIS 2D, presented for permanent surcharge.

3.1.4 Discussion and Conclusion

Comparing the measurements with the modelling result, they are at about the same order of magnitude. The measured forces are in the range of average 1-3 kN/m over time and modelling results exhibit average forces in the same range. The average force exhibited during self-weight are a bit lower than the measured results for the loading stage, but when subjected to permanent load the model gives slightly higher values than the measured ones. Monitored and modelled results of strains and forces in the geogrids are set side by side in Table 3.4. When comparing the results, it is important to have in mind that the monitored results are taken at one point in each grid, and an average is then calculated over those 8 measurements. The modelled forces are presented over the whole geogrid, and the average forces are obtained by taking the modelled forces over whole geogrids. The modelled average force in the geogrids, at end of construction, are $1.11kN/m$, approximately 2% of short term ultimate tensile strength.

The monitored strains in the geogrids are a bit higher than the modelled results for all loading conditions. As the strains are measured over three points in every geogrid, and

the modelled results are obtained from deformations over the whole length of the geogrid, they should be comparable. However, the average strains in Table 3.4 during self-weight are calculated based on the measurements in one point on every geogrid, 0.86 m behind the facing. Looking at the distribution of the strain in Figure 3.4, the average strains 0.86 m behind the slope face are assumably higher than the average for all of the measurements. The figure also shows that the modelled strains agree quite well with the measured for the 5 lower geogrids but are a bit low in the top 3 layers. The horizontal strain in the soil correlates with the strains in the geogrid well enough to assume that the strains in the grid are realistic.

Loading conditions	**Average** $\epsilon_{0.86}(\%)$	**Average** ϵ (%)	**Average** T (kN/m)
Self-weight, monitored results	0.47		1.76
Modelling Self-weight		0.14	1.11
Permanent surcharge, monitored results	0.70	0.56	2.49
Modelling Permanent surcharge		0.41	2.72

Table 3.4: Modelled and monitored results under different loading conditions.

Deformations of the structure have not been monitored, so there are no measured results to compare with. In section 2.4 it is said that the vertical strains in a GRS abutment itself should be less than ϵ_v = 0.5 % and the vertical deformations can be estimated to be: $\epsilon_v * H$, H being the abutment height. Applied in this case it would give a maximum vertical displacement of 24 mm in the slope. The results from the modelling of the slope showed vertical deformations in the scale of 27 mm from end of construction to permanent load was placed, and the total vertical deformations at the same time were 30 mm. Horizontal deformations of a reinforced abutment and walls can be expected to be 0.1-0.3 % of the structure height H (Vegdirektoratet, 2018). For this slope it would mean the horizontal displacement would be expected to be in the range of 4.8 to 14.4 mm. The horizontal deformation from the model is about 22 mm in the slope itself after the end of construction, 1.5 times higher than expected for a comparable GRS abutment/wall.

The results from the numerical modelling of the slope fits overall reasonably well with the measurements from the case and the deformations of the slope are within the range of what could be expected in a GRS abutment of the same dimensions. There are of course many assumptions made when modelling the slope that will affect the outcome but seeing the agreement between the modelled and the measured results, they can be assumed to be to have a fairly good correlation with the reality. The differences in the results between the modelled case and the measurements can partially be explained by the lack of information of the properties of the back fill and foundation soil. The choice of soil models will also affect the result, with more advanced soil models giving additional information of long-term creep and degradation deformations. In this case the Mohr-Coulomb model is used for the foundation soil and the Hardening Soil model for the back fill soil. The Hardening Soil model does capture the hardening behaviour of sand in a realistic way 2.6.3, but does not take creep/degradation in the soil into account. Neither does the elasto-plastic Mohr-Coulomb model, which offers a simplified approach to deformations. Nevertheless, the

Figure 3.9: Picture of the finished slope, not yet vegetated (Vaslestad et al., 1996)

results for the case correlate good enough to argue that the modelling approach could be adapted to other situations, giving realistic predictions of the behaviour of a reinforced structure.

3.2 Reinforced Slope Lillehammer

During the summer of 1993 a 13 m high geosynthetic reinforced slope was built in Lillehammer as a part of a new road system. The slope was built along the side of a road leading into a tunnel under the city. The horizontal deformations of the slope have been measured over the last decades by an inclinometer channel. The slope starts at the tunnel opening, descending 120 meters from the opening. The slope angle is 60°with a terrace at the height of 2.5 meter for aesthetic reasons. The front of the slope is vegetated to absorb traffic noise. A picture of the finished slope can be seen in Figure 3.9. The subsoil consists of silty, gravelly sand and the material was used as backfill in the construction of the slope. The reinforcement used in the slope is a woven polyester geotextile with uniaxial characteristic, giving a short-term tensile strength of 150 kN/m(Vaslestad et al., 1996). After the end of construction, the slope experienced no external additional loads.

The slope was constructed using 0.25-meter soil lift compacted to an average of 96% Standard Proctor. Drainage layers of a thickness 0.5 were placed at the bottom and back of the slope. In addition, 0.2 m thick drainage layers were incorporated with a vertical spacing of 1.5 meter, connecting to the drainage layer at the back of the slope. The primary layers of reinforcement have a length of 7.8 meter and were placed at every 1.0 meter, except at the top two layers, where the vertical spacing was 1.5 m. The secondary reinforcement was placed in between, with a vertical spacing of 0.5 meter. An overview of the construction can be seen in Figure 3.10. The behaviour of the geotextile is described in detail in

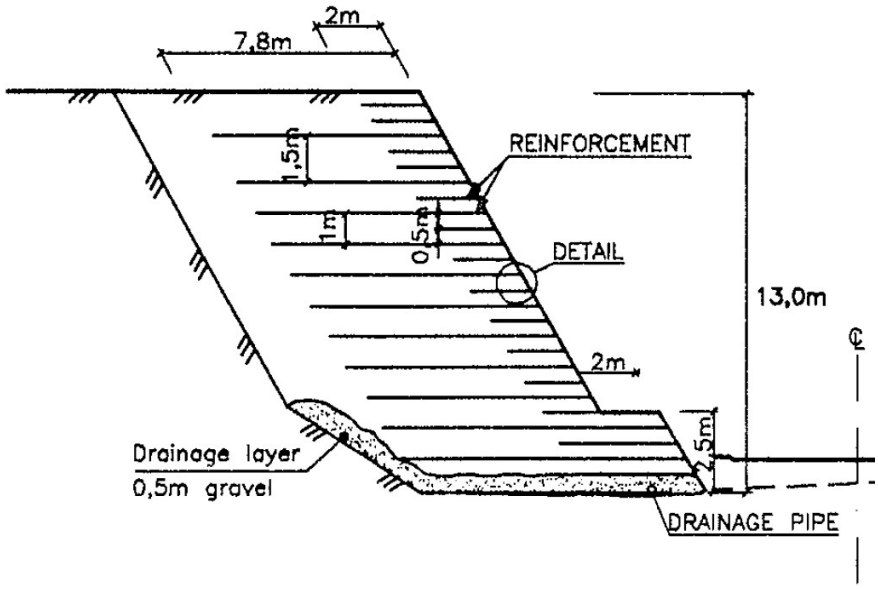

Figure 3.10: Cross-section of the reinforced slope in Lillehammer (Vaslestad et al., 1996)

Fjeldheim (1993), showing a material with high axial stiffness with a tensile strength of 150 kN/mat strains of about 10 %, giving an axial stiffness, EA = 1500 kN/m.

Triaxial tests of the in-situ soil exhibited a characteristic friction angle of $\phi = 36°$ and cohesion of $c = 7kPa$. The material was compacted to ca. 96 % Standard Proctor. The ground water level was located below the bottom of the slope (Vaslestad et al., 1996). There is no available information of the soil stiffness for the backfill material, the parameters used are estimated based on information from PLAXIS (2021a) and Nordal (2020). There is neither any data on the seepage of the soil and this approximation is based on the particle-size distribution (Fjeldheim, 1993), Hazen's formula and experience-based values (Emdal, 2013). The seepage was found to be between 0.35 - 3 m/day for the silty sand and around 10 - 15 m/day for the drainage material. The dilatation angle is estimated based on PLAXIS (2021a) and Nordal (2020), and the characteristics of the material, with a conservative approach.

3.2.1 Measurements from Monitoring of the Slope

Monitoring results of horizontal deformations of the slope, measured by an inclinometer channel located 3 meter behind the face of the slope, are presented in Vaslestad et al. (1996) and Vaslestad et al. (2012). The deformations have been measured over a period of 18 years after the construction. The top of the slope always exhibits the largest horizontal deformations, decreasing with depth and converging towards zero at the bottom of the

slope. The deformations in the first months and year are shown to be the largest, with about 6-8 mm deformations at the top after a month and 14-15 mm within the first year. The rate of the deformations slows down after the initial year, increasing with around 1-1.5 mm/year at the top of the construction. The last measurements, from 2012, show a total deformation of about 40 mm at the top of the slope. Figure 3.11 illustrates the horizontal deformations in the slope during the first 3 years after ended construction.

3.2.2 Modelling of the Slope

When modelling the slope, the Hardening Soil model (2.6.3) was used to imitate the behaviour of sand under load and unloading conditions and compaction of the soil in the construction phase. For the foundation soil, the Mohr-Coulomb model with the same strength parameters as the backfill soil was used. Since the geotextile operates in a range of very small strains and is restricted to maximum 5% strain within the lifetime of the reinforced structure (Vegdirektoratet, 2018), it can be approximated to behave linearly elastic, perfectly plastic. To model the geotextile-soil interaction, an interface was created. The interface strength is guarded by Mohr-coulomb criterion and is assumed to behave linearly elastic, with the same strength parameters as the surrounding soil reduced with a factor of 0.7 (Rogbeck et al., 2006). A summary of the parameters and material models used for the different elements can be seen in Table 3.5.

The slope was modelled in PLAXIS 2D, using 15-node elements, under plain-strain conditions using a fine mesh. Stages in the construction were imitated to get as realistic as possible development of stresses and strains in the construction. Starting with excavating the area with a slope at the back of the reinforcement of 1:1.5. After that, each soil lift was constructed individually as a stage, with induced compaction as a line load of 15 kN/mover the whole layer. Since the slope is 13 m, with 0.25 m soil lift, the construction of the slope itself was 52 stages. The computational time for this and the following consolidation phases were too high and time-consuming, so a simplified model with 1 m soil lift were made, pictured in Figure 3.12. Calculations were made in both drained and partially undrained conditions. Since permeability in the soil is quite high, totally undrained conditions does not represent a realistic approach, and therefore some phases of consolidation were incorporated to achieve partially saturated conditions in the slope. The boundary conditions of the slope allowed vertical movement but not horizontal at the two sides of the model, and the boundary condition at the bottom of the model did not allow horizontal or vertical deformations. An overview of the whole model is available in Appendix B and for the 52 stage model in Appendix B.

3.2.3 Results Reinforced Slope Lillehammer

The results from the analysis showed deformations in the soil almost immediately in the consolidation phases, after the end of construction. The deformations did not change noticeably with time and kept rather constant within the post-construction phase. The drained analysis exhibit no further horizontal deformation after the end of the construction. The partially undrained analysis exhibits horizontal deformations in in the direction in towards the slope, Figure 3.11 illustrates the deformations 3 meter behind the front. For both the

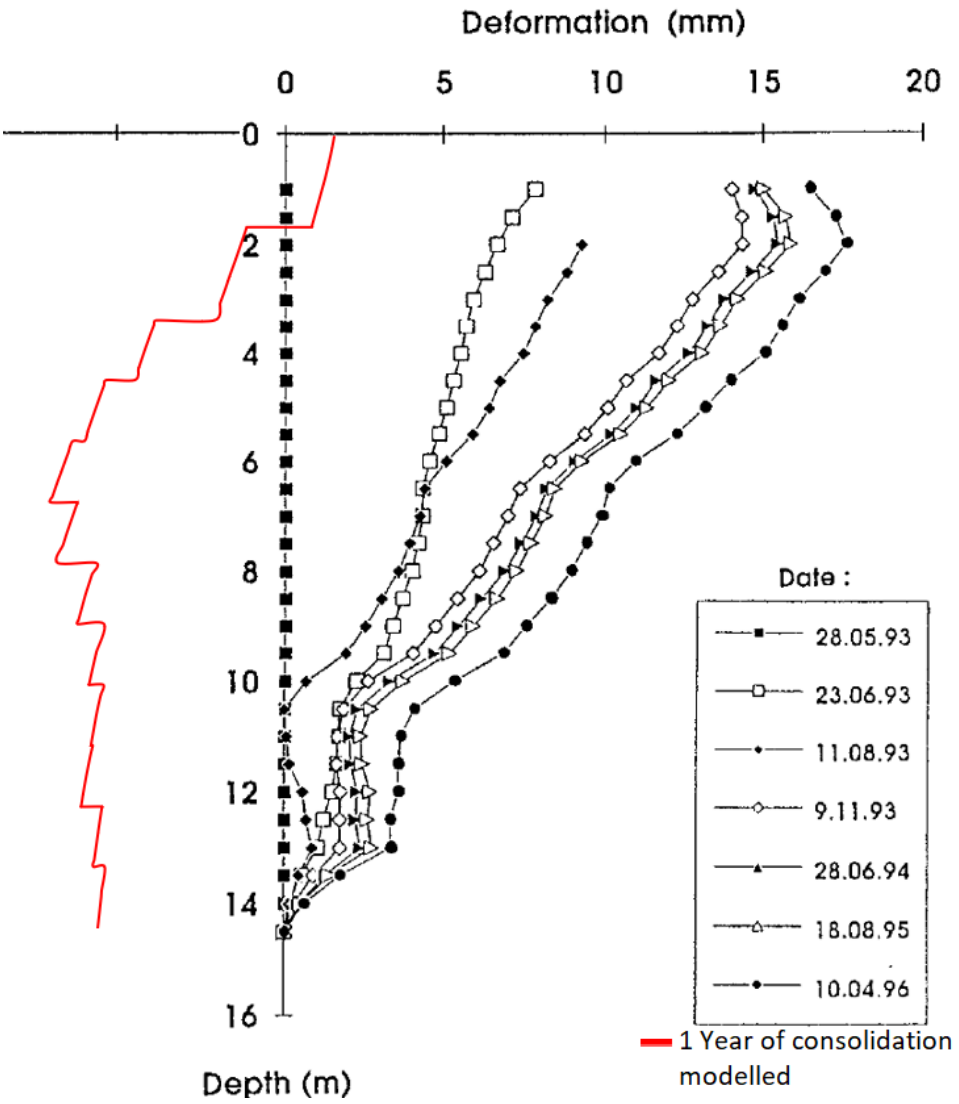

Figure 3.11: Horizontal deformations after the end of construction, for the first 3 years (Vaslestad et al., 1996) and Horizontal deformations 1 year after ended construction, partially drained modelled in PLAXIS.

Category	Description
Backfill soil	Hardening soil model Dry and wet unit weight: $\gamma_{unsat} = 17kN/m^3$ $\gamma_{sat} = 18kN/m^3$ Cohesion $c = 7kPa$ Friction angle $\phi = 36°$ Dilatation angle $\psi = 4°$ Stiffness parameters: $E_{50}^{ref} = 30000kPa$ $E_{ur}^{ref} = 90,000kPa$ $E_{oed}^{ref} = 30,000kPa$ $\nu_{ur} = 0.2$ and $m = 0.5$ Seepage: $k_x = k_y = 0.35m/day$
Foundation soil	Mohr-Coulomb soil model Dry and wet unit weight: $\gamma_{unsat} = 17kN/m^3$ $\gamma_{sat} = 18kN/m^3$ Cohesion $c = 7kPa$ Friction angle $\phi = 36°$ Dilatation angle $\psi = 4°$ Stiffness parameter: $E = 22300kPa$, $\nu = 0.3$ Seepage: $k_x = k_y = 0.35m/day$
Drainage soil	Hardening soil model Dry and wet unit weight: $\gamma_{unsat} = 17kN/m^3$ $\gamma_{sat} = 18kN/m^3$ Cohesion $c = 7kPa$ Friction angle $\phi = 36°$ Dilatation angle $\psi = 4°$ Stiffness parameter: $E = 30000kPa$ and $\nu = 0.2$ Seepage: $k_x = k_y = 13m/day$
Interface soil-geotextile	Mohr-Coulomb soil model Cohesion $c = 7kPa$ Friction angle $\phi = 36°$ Dilatation angle $\psi = 4°$ Stiffness parameters: $E = 3000kPa$ and $\nu = 0.2$
Geotextile	Linear elastic Short-time tensile strength $T = 150kN/m$ $EA = 1500kN/m$

Table 3.5: Modelling parameters for the reinforced slope in Lillehammer

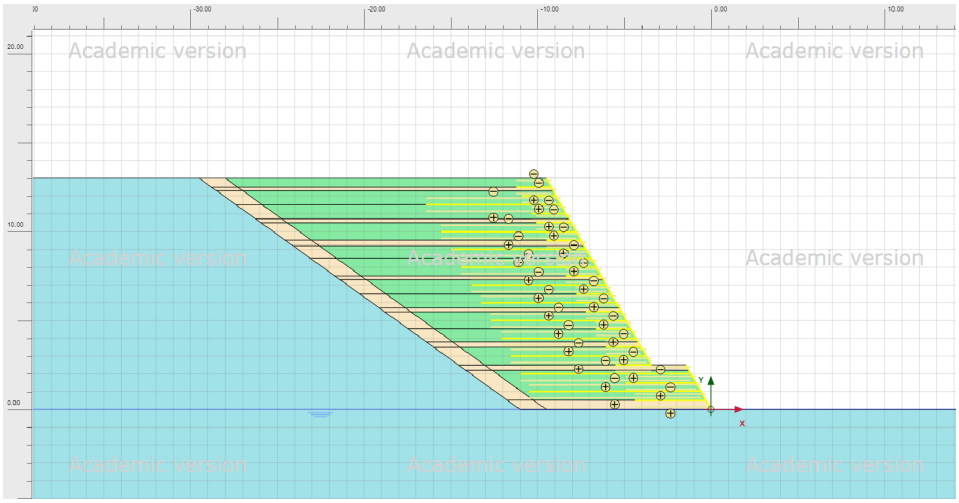

Figure 3.12: Close-up of the reinforced slope in Lillehammer, modelled in PLAXIS.

drained, and partially undrained analysis, the maximum deformations in the slope at the end of construction are in the upper part and the front of the slope. In drained situation, horizontal displacement is about 1.0% of the total height of the slope at most and the vertical displacement around 1.2%. For the partially undrained analysis, maximal deformations displayed at the end of construction were 2.6% horizontally and 1.8% vertically of the total height of the slope.

The forces in the geotextile had an average value of 16.3 kN/m after the end of construction of the slope for the partially drained analysis and 5.7 kN/m for the drained analysis. From end of construction until the end of the last phase of consolidation the average force changes marginally for both cases. The strains in the geotextile are deduced from the deformations in the nodal points on the grids. Average deformations are calculated by using the local, axial displacement at the end nodes of the geogrid, finding the elongation of the grid, ΔL, and dividing it with the original length of the grid: $\epsilon = \frac{\Delta L}{L}$. At the end of constructing the slope, the average strains in the reinforcements are about 1.3% for partially undrained analysis and 0.4 % for drained analysis.

3.2.4 Discussion and Conclusion

Monitored results of the horizontal deformations of the 13 m high slope and the results from the numerical modelling of the slope did not correlate at all. The post-construction deformations, that where the measurements in this case, proved hard to predict. The chosen soil model, Hardening Soil model, is a constitutive model that describes the soil's response to load and unloading and does not take creep and degradation of the soil over time into account. In this case, the slope experienced no additional loads after the end of construction. The partially undrained analysis does change the load situation by decreasing pore pressures, but it results in a deformation inward in the slope, and not forward as

in the monitored case. This could be because of the placement of the drainage material at the back and the model's approach to pore pressure dissipation. The drained situation exhibited almost any additional deformation after the end of construction. This would be logical since the chosen soil models associate the incremental deformations with change in loading.

Looking at the deformations and strains in the structure at the end of construction, they are in a quite reasonable range. The strains about 0.4 and 1.3% (drained and partially drained) are less than the required 2% (Vegdirektoratet, 2018), and the average tensile force of 5.7 to 16.3 kN/m is approximately 4 and 11% (drained and partially drained) of the short-term tensile strength for the geotextile. Since there were no monitoring of these parameters for the slope, there are no values to compare with.

The factors affecting the deformations of the slope after end of construction would initially be due to drainage and initial settlement, but after approximately 1 year, the rate of deformation decreases significantly. The monitored deformation rate is more or less constant over the following 17 years, indicating that it is due to degradation and creep in the soil. There are constitutive models that can take this into account, but it takes some knowledge of the soil behaviour and often oedometer testes are conducted to find such parameters. Since there is a lack of information considering the stiffness and consolidation behaviour of the soil, it is challenging to use these advanced soil models in a realistic way.

The deformations that occurred during the first year were not modelled successfully. Neither of the approaches used, drained or partially drained, responded similarly as the real slope. The model's post-construction deformation rely on a realistic change in pore pressure, since it is the only load changing. It can be challenging to model pore pressures correctly with simple soil models and may be one of the reasons for the misleading results.

Because of the shortcomings in the modelling of the slope, it is not relevant when looking at long-term settlements and deformations after the end of the construction.

3.3 Discussion and Conclusion of the Modelling of Existing Slopes

The modelling of the two existing slopes had various outcome. The model of the slope in Skedsmo fits overall reasonably well with the measurements from the monitoring of the case, and the deformations of the slope are in the range of what could be expected in a GRS abutment of the same dimensions. The model of the slope in Lillehammer, however, was more challenging, and the long-term prediction for the behaviour of the slope was not realistic.

A difference between the two cases is that the slope in Skedsmo experienced change in external loading, even after the end of the constructing phase, while the slope in Lillehammer did not. The chosen soil models in the analysis respond mainly to changes in loading and is thereby more accurate to use in the analysis of the Skedsmo slope. Even though the slope in Lillehammer does exhibit deformations during monitoring, the behaviour is

more difficult to predict, partially because it depends on dissipation of pore pressure and partially because some of the deformations are due to creep and degradation. Modelling pore pressure and the dissipation of pore pressure can be challenging, as it depends on assumptions and simplifications in the model.

Comparing the two models at the end of construction, it can be seen that the force in the geogrid used in Skedsmo is about 1.1 kN/m, 2% of its ultimate tensile strength, while the geotextiles in the Lillehammer slope, the forces are 5.7 and 16.3 kN/m (drained and partially drained). It corresponds to approximately 4 and 11% (drained and partially drained) of the short-term tensile strength for the geotextile. Modelled average strains in the geogrids for Skedsmo at end of construction are low, $\epsilon = 0.14\%$. The corresponding value for the slope in Lillehammer is about 0.4 and 1.3% (drained and partially drained). Deformations at the same stage are respectively 0.3% horizontally and 0.7% vertically, compared to the height of the Skedsmo slope. For the Lillehammer slope, the deformations of the drained model are 1.0% horizontally and 1.2% vertically, while for partially undrained 2.6% horizontally and 1.8% vertically. Looking at these values, the Lillehammer slope has consequently higher values than the slope in Skedsmo, both for its drained and partially drained analysis. The values obtained at drained analysis for Lillehammer slope are however closer to the values from the Skedsmo slope. The results obtained for the slopes at the end of construction phase are of the same magnitude. Since the Skedsmo slope provided a reasonable fit with expected results, the first part in the modelling of Lillehammer slope, until the end of construction, seems to be quite acceptable and the response in the model could be realistic.

Based on the similar case modelled in Skedsmo, the modelling of the slope in Lillehammer seems to be acceptable until the end of construction. Post-construction behaviour is not represented realistically and cannot be predicted using the approach for a similar case. For the slope in Skedsmo the results correlate good enough to argue that the modelling approach could be adapted to other situations, giving realistic predictions of the behaviour of a reinforced structure. For a more accurate modelling of the post-construction behaviour, more advanced soil models should be applied. More advanced soil models need more information of the material, requiring testing and evaluation of the material to a larger extent than what is available for these cases.

Chapter 4

Modelling of a Potential GRS Bridge Abutment

This chapter presents a model of a bridge abutment constructed using the GRS approach. The location and the premises of the bridge abutment will be presented as well as the chosen approach of design for the abutment itself and the interpretation of soil parameters for the existing subsoil. Finally, the deformations of the abutment, and the impact in the geosynthetic reinforcement will be evaluated.

4.1 Background

Risheim bridge, located at Bøn, Eidsvoll municipality in Norway, see Figure 4.1, is a part of county road 504-1, crossing a ravine, with a river at the bottom. The bridge, built in 1950, is a one-spanned bridge 9.44 m long, built on high steep fills with correspondingly high abutments. A photo of the existing bridge can be seen in Figure 4.2.

A report investigating short- and long-term alternative measures to increase the safety conditions for the traffic was conducted for the Norwegian Road Administration, Abrahamsen and Valnes (2011). The report recommends establishing a new bridge at the site as a lasting solution to achieve an acceptable traffic safety. The new bridge is suggested to be built as a one-spanned, with prefabricated beams on concrete abutments with a width sufficient for two cars to meet. The new bridge would have span of 24 meter and a driving-width of 6 meter, giving a total width around 7 meter.

The foundation soil at the site is investigated in Nokken (2010) and consists of a top layer of 4-6 meter silt and sand layers over firm clay. The investigations stopped the soundings at 10-25 meter depth and did not encounter solid rock.

The size and dimensions of the bridge and the relatively solid soil foundation conditions on the site makes it a possible candidate where GRS Abutments are a reasonable alternative.

Figure 4.1: Location and map of the existing bridge (Norgeskart.no, 2021).

Figure 4.2: Picture of the existing bridge (Abrahamsen and Valnes, 2011).

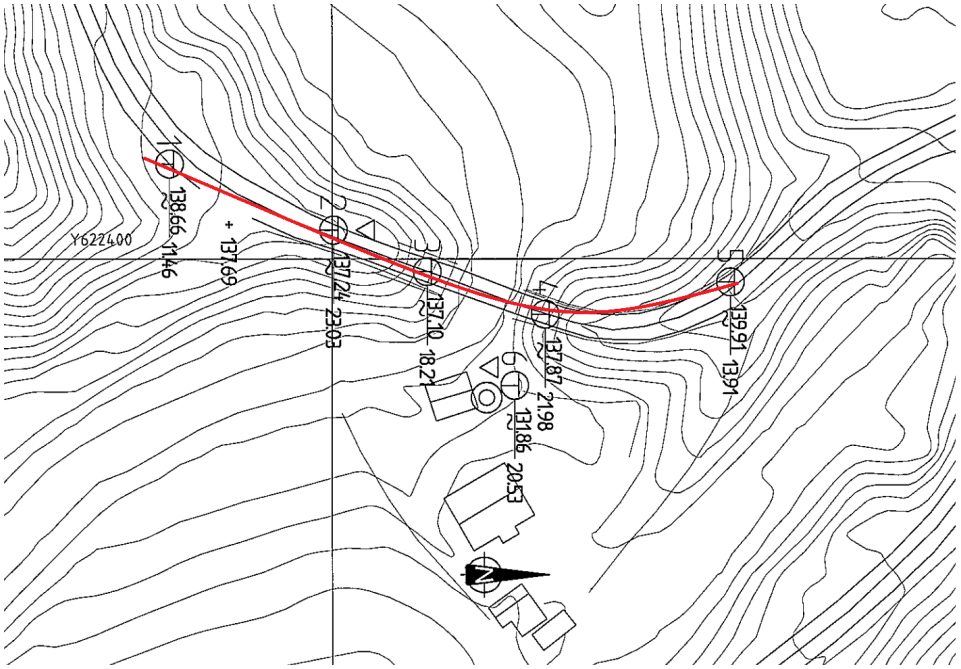

Figure 4.3: Overview of the site investigations with the cross-section, see Appendix C.6 in red (Nokken, 2010).

4.1.1 Ground Conditions

Site investigations and were performed in 2010 and presented in a data report (Nokken, 2010). The results indicate firm foundation soil, with the top at 4-6 meter consisting of sand and silt over clay. The firm clay layer continues for 16-20 meter until the end of sounding. Solid rock is not found in any of the sounding points, and the depth to solid ground is assumed to be large. Total soundings were performed at 6 points, and additional CPTU(Cone Penetration Test Undrained) sounding was done in 2 of the points. An overview of the sounding points can be seen in Figure 4.3. A simple interpretation of the soil layers can be found in Appendix C.6 for the cross section in Figure 4.3. The cross-section is marked with a red line on the map with the soundings.

Phreatic groundwater level is assumed to be at the same level as the river, around +130-131 meters above sea level and approximately following the boundary between the clay and sand/silt layers. In the CPTU interpretations, phreatic groundwater level is set to level +130 and +132 (Nokken, 2010). The river Risa has a normal level of ca. + 130.7 and +132.8 at flooding (Abrahamsen and Valnes, 2011).

The layer consisting of silt and sand at the top have a water-content between 20-40%, and a unit weight γ = 20 kN/m. Interpretation of the results from the CPTU sounding, see Appendix C, indicates a stiffness modulus $M = E_{oed}$ of 8 to 12 MPa, a friction angle ϕ in the range $35°$ and $38°$, and an undrained shear strength c_u between 60 and 200 kPa.

The clay has a water content around 30%, and a unit weight γ= 20 kN/m. Continuous oedometer tests have been performed with clay samples from sounding point 6, 4.5 and 5.5 meter below the surface. The results indicate a modulus number of 25-28, characterising it as a firm clay (Emdal, 2013), not particularly prone to settlements, with a stiffness modulus $M = E_{oed}$ ranging between 5 and 10 MPa. The pre-consolidation stress, p'_c for the samples was found to be around 100 - 130 kPa, indicating it is overconsolidated. The seepage from the oedometer tests were found to be 0.01 to 0.02 m/year, which is approximately $4 * 10^{-5}$ m/day. The clay has a low sensitivity, and an undrained shear strength, c_u, measured 40 kPa increasing to 90 kPa in falling cone and uniaxial tests from the top 3 meter of the clay. Undrained shear strength interpretations from the CPTU soundings indicate an average of 50 kPa at the top, increasing to 150 kPa at the end of the sounding. A conservative choice, looking at the CPTU interpretations, are $c_u = 35 + 2,86 * dz$, with an initial shear strength of 35 kPa at the top of the clay layer, increasing with 2.86 kPa/m depth (Appendix C).

4.1.2 Orientation of GRS Abutment

Based on the ground investigations and the interpretations of the soil layers, the ground conditions are reasonably equal for the abutments on both sides of the creek. The assumption that the modelling of one of the two abutment would give adequate results to predict that the other one would behave similarly, is sensible. Further on, the abutment on the north side of the creek is used in the model. The results are assumed to be representable for both abutments connected to the bridge. Figure 4.4 illustrates the orientation and placement of the GRS abutment. The background of the figure is an illustration the original bridge from the suggestion of Abrahamsen and Valnes (2011) and the soil layers and groundwater level are the interpretations discussed in Section 4.1.1. The whole cross-section can be found in Appenix C.4, as well as interpretations of the soil layers.

4.2 Design of the GRS Integrated Bridge Abutment

The design of the GRS Abutment is to a large extent based on the guidelines from GRS-IBS Interim Implementation Guide by Adams et al. (2012), published by the U.S. Department of Transportation. In Figure 4.5, an overview of the dimensions chosen for the model of the GRS abutment is presented. Element like the bearing bed, reinforcement spacing, reinforcement embedment length and reinforced soil foundation, see Figure 1.2, are described in the design guide.

The height of the abutment is chosen based on the general geometry of the site and initial design of the bridge. Looking at the original drawings of the bridge and the existing terrain, an abutment height of 4 meter was chosen. The total width of the abutment, B_{tot}, are depending on the span length of the bridge. For a bridge with a span length larger than 7.63 meter, the total width of the abutment, including the facing width, should be at least 1.83 meter. B_{tot} of 2.3 meter are chosen, with the facing having a thickness of 0.3 meter. With a truncated base, the ratio B_{tot}/H should at least be 0.3, which it exceeds in this particular case.

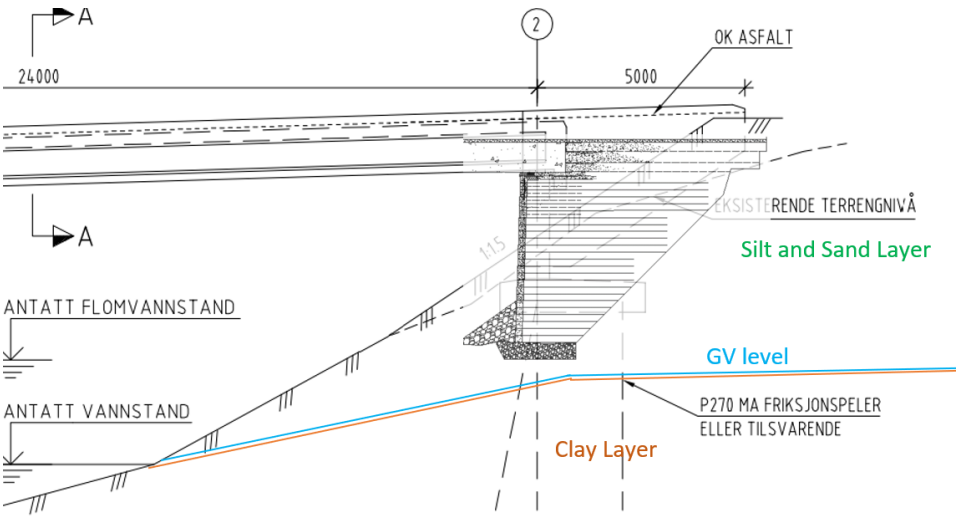

Figure 4.4: A part of the cross-section for the new bridge, from (Abrahamsen and Valnes, 2011), with the orientation of the GRS Abutment and soil layers.

The beam seat is the area where the bridge will be placed upon. The width of the beam seat is based on the span of the bridge. If the span of the bridge, L_{span}, is larger than 7.63 meter, the beam seat is recommended to be 0.763 meter or wider. The bearing bed under the beam seat is the area in the abutment experiencing the largest impact loads. The area is reinforced with an extra, secondary reinforcement, to increase its strength. The width of the bearing bed reinforcement zone is recommended to be as wide as the beam seat and extend at least 0.2 meter behind it. There should be a minimum of 5 layers with the secondary reinforcement. Vertical reinforcement spacing for the primary reinforcement is recommended to be 0.3 meter or less. The reinforcement spacing in the bearing bed should be half of the primary reinforcement spacing, and no more than 0.15 m.

In this design, the beam seat is chosen to be 0.8 m. The setback distance is chosen to be 0.3 m, making the minimum recommended bearing bed width $0.8 + 2 * 0.3 = 1.4m$. The bearing bed width was chosen to be 1.7 meter, hence the secondary reinforcement length is 1.7 m. Vertical reinforcement spacing is chosen to be 0.2 m in the primary reinforcement, and 0.1 m in the bearing bed with the secondary reinforcement.

The embedment length of the reinforcement is decided based on the height of the abutment. When designing an abutment with truncated base, the reinforcement at the bottom should at minimum extend the base width and increasing, following the cut slope to preferably a length of 0.7H. For excavation with a back slope flatter than 1:1, reinforcement lengths larger than $1H$ is not needed. In this model the embedment length of the reinforcement is extended to the slope line of 1:1.5.

The reinforced soil foundation RFS should, according to the guidelines, extend 1/4 of B_{tot} beyond the base of the abutment, and have a depth of $1/4 * B_{tot}$. In this model $1/4 * B_{tot}$

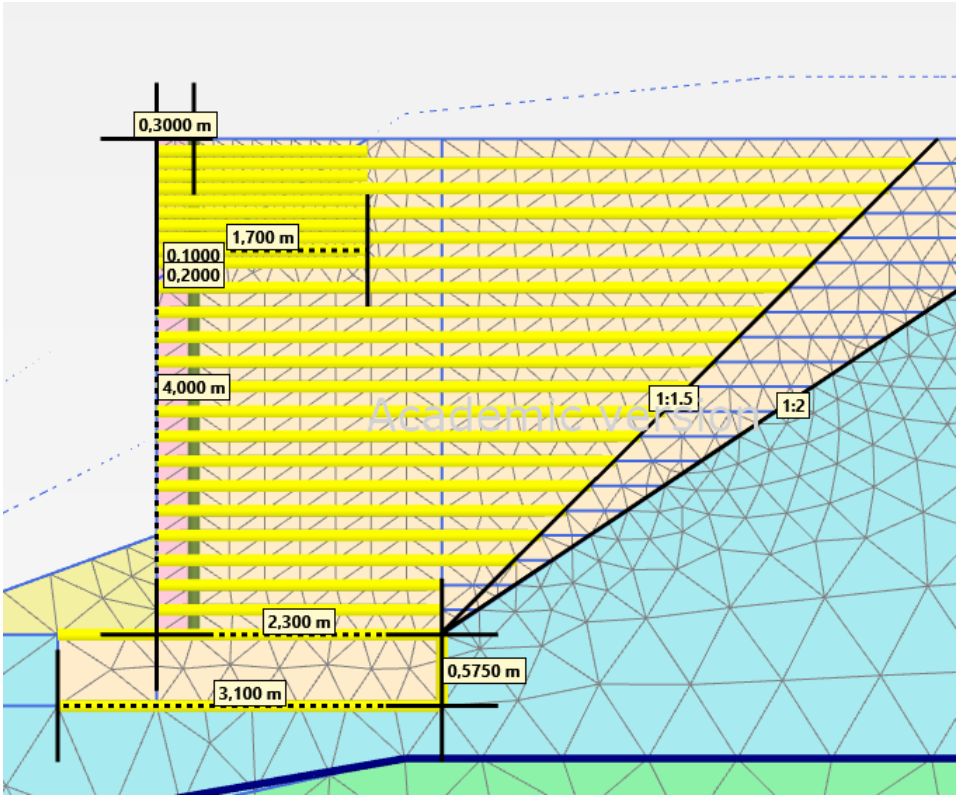

Figure 4.5: Dimensions of elements in the GRS abutment

is 0.575 m and the RSF dimensions are chosen to be $3.1m * 0.575m$

The superstructure has a width of around 7 meters in the plane. The GRS Abutment would extend further, extending to around 8.5 to 10.5 meter into the plane, looking at the design of Maree Michel Bridge (Saghebfar et al., 2017).

4.3 Modelling of the GRS Abutment

The GRS abutment is modelled using PLAXIS 2D FEM program. Plane strain conditions are presumed, using 15-noded elements and a fine mesh. The abutment layout and dimensions of the abutment is described in the section above 4.2 and illustrated in Figure 4.5. The model is a cross-section, assumed to be located at the centre-line of the abutment. Initial excavations are done with slope of 1:2 at the back. The construction of the abutment is modelled in stages, using 0.2 meter soil lift at every stage and induced a 15 kN/m line load on top. The line load approximates the impact of the compaction of the soil lifts during the construction of the abutment, using the same approach as in Section 3.2 and 3.1. When the construction of the abutment was finished, the installation of the

bridge was modelled by applying a line load over the beam seat. To check the stability of the abutment, a load corresponding to the live loads was applied over the beam seat. A 15 kN/m line load was applied over the back fill to the edge of the model, approximately equal to the load of the road embankment and pavement. A riprap is placed at the bottom front to prevent water from eroding into the material, weakening the abutment.

Since the subsoil consists of clay, which has a low permeability, using undrained analysis for the construction of the GRS abutment was suitable. The subsoil is modelled as undrained during the construction phase, to the placement of the bridge. After the bridge is placed, a consolidation analysis was performed to evaluate the effects of the dissipating pore pressure over time. The backfill was set to dry cluster, since there is no noticeable extra pore pressure built up in the material and it has a high permeability.

When modelling undrained behaviour in PLAXIS 2D, several approaches are available, see Section 2.6.3. From the soil investigations, described in Section 4.1.1, the undrained strength-parameters are evaluated but not so much the effective strength parameters. Using the undrained strength parameters, modelled with Undrained B, gives a good approximation of the actual strength of the soil, and stability of the abutment, but has its shortcomings when evaluating deformations due to the way it generates pore pressure. Undrained B is due to this, and the constant definition of strength, not appropriate to be used ahead of a consolidation analysis. When performing undrained analysis with subsequent consolidation analysis, Undrained A is a suitable model to use. Undrained A is based on effective strength of the material and has more accurate generation of pore pressures and deformations but can over-predict the strength of the material in the undrained analysis. With this in mind, two separate analyses were done: one using Undrained B, with the purpose of looking at the strength and stability if the abutment, and one using Undrained A, looking at the deformations and strains in the structure. Since the soil investigations linked to effective strength parameters are deficient, the analysis were performed using estimated parameters with a lower- and high-limit approach. The consolidation analysis is modelling the changes over 5 years.

The Hardening soil model was used for the backfill material, and Mohr-Coulomb for the clay and silt/sand at the site. The backfill material was assumed to have a unit weight $\gamma = 19kN/m^3$, friction angle $\phi = 38°$ and dilatation angle $\psi = 8°$. The stiffness and strength parameters are further presented in Table 4.1 and are estimated based on information from PLAXIS (2021b), Nordal (2020) and requirements from Adams et al. (2012). The dilatation angle is estimated on the basis of PLAXIS (2021a) and Nordal (2020), and the characteristics of the material, with a conservative approach.

For the silt/sand material, a unit weight is $\gamma_{sat} = 20kN/m^3$, friction angle ϕ is in the range 35-38°and a stiffness $E_{oed} = 8,000 - 12,000kPa$ from soil investigations (4.1.1). The seepage k and Poisson's ratio ν are based on information from Nordal (2020) and Emdal (2013). The undrained shear strength c_u of the material is conservatively chosen to be 60 kPa, see Section 4.1.1.

The clay has a unit weight of $\gamma_{sat} = 20kN/m^3$, stiffness $E_{oed} = 5,000 - 10,000kPa$, seepage $k = 0.04 * 10^{-3}m/day$ from soil investigations. The undrained shear strength is conservatively chosen to be $c_u = 35 + 2,86 * dz$, from Section 4.1.1. The clay exhibits

characteristics as a firm clay and can be assumed to have effective strength parameters in the following range: Based on Nordal (2020), typical values for Norwegian clay of medium dense characteristics has attraction $a = 15$ to $25kPa$ and a friction $tan(\phi) = 0.50$ to $0.5 - 0.55$. Therefore, the cohesion $c = 7.5$ to $13.75kPa$ and friction angle $\phi = 26.5 - 28.8°$ are chosen as the upper and lower limits. Poisson's ratio ν for the clay is estimated based on information from Nordal (2020) and Emdal (2013).

The geosynthetic is assumed to have a tensile ultimate strength of $T = 70kN/m$, the minimum requirement from Adams et al. (2012), giving an axial stiffness at about $EA = 600kN/m$. It is assumed to behave linearly elastic, perfectly plastic. The interaction between the geosynthetic and the backfill soil is modelled with an interface, guarded by the Mohr-Coulomb strength criterion with the same parameters as the backfill soil, reduced with a factor of 0.8.

The parameters of the facing and RipRap are assumed to be approximately the same as what is used in Abu-Farsakh et al. (2019). They are both models using a linear elastic model. The interaction between the facing and geosynthetic is modelled with an interface guarded by the Mohr-Coulomb strength criterion. Materials and parameters are listed in Table 4.1 and 4.2.

The load from the bridge onto the abutment, modelled as Dead Load, is based on Vegdirektoratet (2019, p.11), guidelines for prefabricated bridge beams. Bridge beam (d) on page 11 was used to estimate the loads in the model. Since the prefabricated beam bridge has a road-width of 8.6 meter and the one suggested in Risheim only have a road-width of 6 meter, the loads are adjusted. From this, the prefabricated bridge is assumed to have a dead-weight of 14 kN/m^2, which will give a dead load of 120 kN/m over the beam seat. The live load is estimated from Lovdata.no (2021), giving an approximate additional load of 135 kN/m. The live load is assumed to have elastic impact, with no permanent deformations. When modelling the abutment, only vertical loads are taken into account, and additional forces acting on the abutment, like breaking forces and effects of wind or cyclic loading, are neglected.

When modelling the abutment, no strength reduction of the soil or geosynthetic is applied, and no load factors are taken into account for the dead and live load.

Boundary conditions of the model allowed vertical movement, but not horizontal for the two sides, and the boundary condition at the bottom at the model did not allow horizontal or vertical deformations. The bottom and left-hand boundary allowed seepage, but the right hand boundary with the middle of the river, was closed for seepage. This is a realistic approach since there is no solid rock found, assuming water can dissipate downwards trough the clay.

The phreatic groundwater level is assumed to be the same level as the surface of the river, following the boundary between the clay and the silt/sand. The water level during flooding is not considered, since it does not have a negative impact on the stability of the abutment. In addition, a riprap or protection should be placed along the riverbank, so that the river cannot erode into the soil and abutment. This is not further investigated in this assignment, but should be considered in design for practical use. A figure of the initial geometry in the

Category	Description
Backfill soil	Hardening soil model Dry and wet unit weight: $\gamma_{unsat} = 19kN/m^3$ $\gamma_{sat} = 19kN/m^3$ Cohesion: $c = 0.1kPa$ Friction angle: $\phi = 38°$ Dilatation angle: $\psi = 8°$ Stiffness parameters: $E_{50}^{ref} = 40,000kPa$ $E_{ur}^{ref} = 120,000kPa$ $E_{oed}^{ref} = 40,000kPa$ $\nu_{ur} = 0.2$ and $m = 0.5$
Foundation soil Silt/Sand	Mohr-Coulomb soil model Dry and wet unit weight: $\gamma_{unsat} = 19kN/m^3$ $\gamma_{sat} = 20kN/m^3$ Cohesion $c = 1kPa$ Friction angle $\phi = 35 - 38°$ Undrained shear strength $c_u = 60kPa$ Stiffness parameters: $E_{oed} = 8,000 - 12,000kPa$ $\nu = 0.35$ Seepage: $k_x = k_y = 0.35m/day$
Foundation soil Clay	Mohr-Coulomb soil model Dry and wet unit weight: $\gamma_{unsat} = 19kN/m^3$ $\gamma_{sat} = 20kN/m^3$ Cohesion $c = 7.5 - 13.75kPa$ Friction angle $\phi = 26.5 - 28.8°$ Undrained shear strength $c_u = 35 + 2.86 * dzkPa$ Stiffness parameters: $E_{oed} = 5000 - 10,000kPa$ $\nu = 0.38$ Seepage: $k_x = k_y = 0.04 * 10^{-3}m/day$
Interface soil-geotextile	Mohr-Coulomb soil model Friction angle $\phi = 30.4°$ Dilatation angle $\psi = 6.4°$ Stiffness parameters $E' = 7500kPa$ $\nu = 0.25$

Table 4.1: Modelling parameters for GRS Abutment Risheim, Part 1

Category	Description
Geoynthetic	Linear elastic Short time tensile strength $T = 70kN/m$ $EA = 600kN/m$
Facing	Linear elastic $\gamma = 12.5kN/m^3$ $E' = 30,000000kPa$ $\nu = 0$ Geogrid Front with EA = 1000 kN/m Interface strength reduction $R_i = 0.65$
RipRap	Linear elastic $\gamma = 22kN/m^3$ $E' = 50,000kPa$ $\nu = 0.25$

Table 4.2: Modelling parameters for GRS Abutment Risheim, Part 2

model can be seen in Appendix C and over the finished abutment in Appendix C.

4.3.1 Results Modelling GRS Abutment

The results from the different models will be presented in this section.

Modelling with Undrained B

When modelling with the total shear strength parameters, using Undrained B, the main focus is the stability of the abutment. The result shows that the stability for the structure with undrained strength parameters gives a sufficient resistance against failure and exhibits a satisfactory behaviour both during construction and when external loads are applied.

The average force in the geosynthetic reinforcement at the end of abutment construction is 1.16 kN/m, and 1.78 kN/m when the bridge is placed, and dead load applied. The average force increases to 2.68 kN/m when adding the live load. The highest force in the reinforcements is exhibited at the transition between facing and GRS body in all of the load cases. The average force in the individual reinforcements is plotted in Figure 4.10.

Modelling with Undrained A

When using Undrained A in the soil model, the strength of the soil is defined by the effective strength parameters. The main goal of the analysis is the evaluation of the deformations and strains developed in the abutment, both short-term and over time. The modelling has been done with a higher and a lower limit, both will be presented in this section. Higher limit analysis is denoted HL and lower limit LL further on.

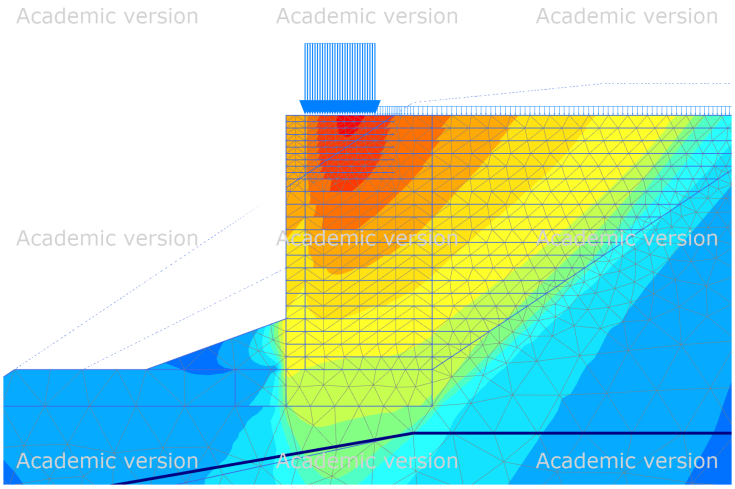

Figure 4.6: Total deformations in the abutment

The largest deformation in the abutment, after ended construction, appears at the top of the abutment, about 1 meter behind the front, right under the bearing bed. Both when there is no load applied and when dead load is applied this area exhibits the highest deformations, and for the LL and HL analysis. The deformations can be seen in Figure 4.6, with red illustrating the highest deformations and dark blue none.

The deformations are more closely evaluated in a cross-section 0.6 meter behind the face of the abutment. The results show a total deformation in the scale of 140 mm for the LL analysis after 5 years of consolidation. Looking at horizontal deformations, the maximum displayed deformation ranges from 43 mm at the end of construction to 82 mm when the dead load is applied and decreasing to 78 mm after 5 years of consolidation. The highest horizontal deformations appear in the upper 1 meter of the abutment and decreasing with depth. For the vertical deformations, the highest values emerge at the top, linearly decreasing with depth. The maximum vertical displacement at end of construction is about 45 mm, increasing to 99 mm when applying the dead load. The vertical displacement continues to increase to 115 mm within a consolidation time of 5 years. The vertical settlement in the foundation soil is around 54% of the total maximum settlement in the abutment at the end of construction and 67% after 5 years of consolidation. The deformations in the abutment itself, measuring from the end of construction to 5 years of consolidation are in the range of 0.42% of the abutment height in the vertical direction and 0.16 to 0.19% in the horizontal direction. The abutment will settle a total of 70 mm vertically and after the end of the GRS construction and 39 mm horizontally. The horizontal settlement will decrease with time.

The HL analysis exhibits a total deformation around 85 mm after 5 years of consolidation. Maximum horizontal displacement is around 27 mm at the end of construction, increasing

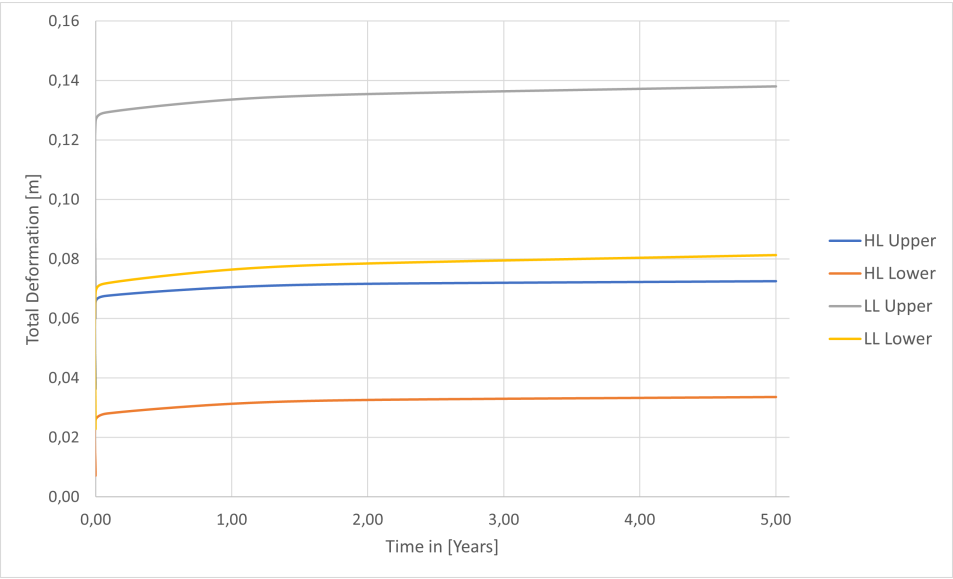

Figure 4.7: Total deformations in meter for different nodes in the GRS abutment, plotted against time in years

to 45 mm when the bridge is installed, and dead load applied. The horizontal displacements decrease marginally with time and measure 43 mm after 5 years of consolidation. The largest horizontal displacement emerges at the top 1 meter of the abutment, as for the LL analysis, and decreases with depth. The vertical displacement of 27 mm at the top of the abutment is exhibited after end of construction, increasing to 61 mm when dead load is applied. The vertical displacement continues to increase with time, reaching 70 mm after 5 years of consolidation. About 28% of the vertical settlements at the end of construction are due to settlements in the foundation soil, increasing to 37% when the dead load is applied and further increasing to 46% after 5 years of consolidation. The isolated settlements in the abutment after the end of construction are about 0.47% vertically and 0.32-0.34% horizontally, corresponding to 43 mm in the vertical direction and 17-19 mm in the horizontal direction. A summary of deformations for the higher and lower limit analysis can be found in Table 4.4.

Deformations for the cross-section are plotted in Figure 4.8, for the end of construction, applying the dead load and after 5 years of consolidation. The graph presents the results both for the LL analysis and the HL analysis. The development of settlements over time can be seen in Figure 4.7, illustrating that the change in deformations decrease with time, being close to zero after 1.5-2 years. The Figure also shows that the majority of the settlements happen instantly, when the load is applied.

The strains in the geosynthetic reinforcement are not available as an automatic output result in PLAXIS but are deduced from the deformations in the nodal points on the reinforcement, as for the two slopes in Section 3.2 and 3.1. Average deformations are calculated

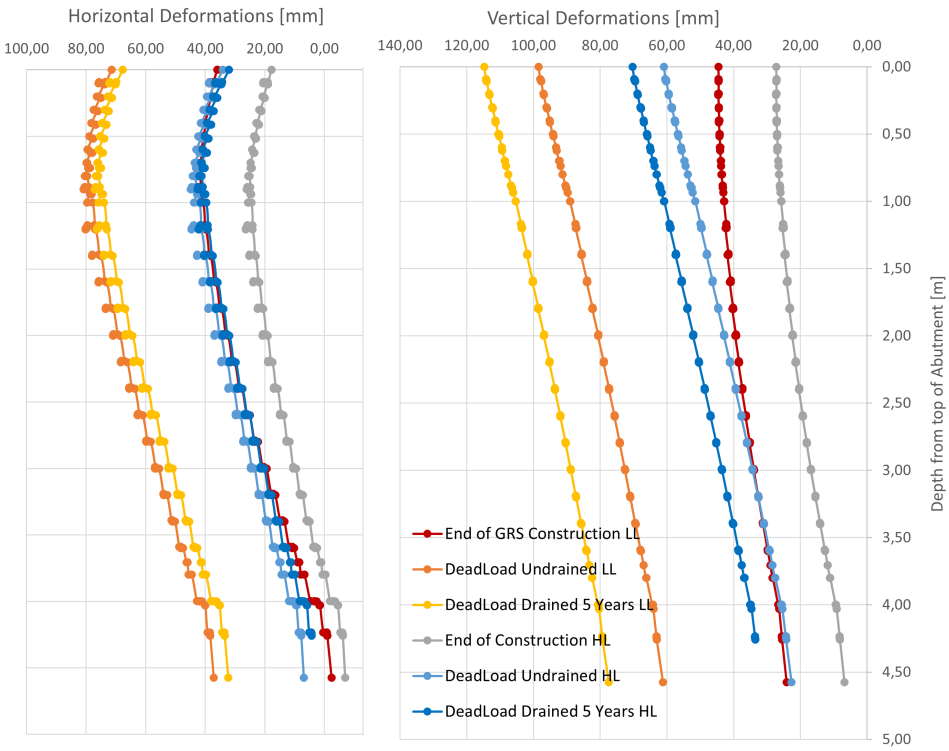

Figure 4.8: Horizontal and vertical deformations in meter for the cross section 0.6 m behind the front, plotted against Y coordinate. LL = Lower Limit, HL = Higher Limit

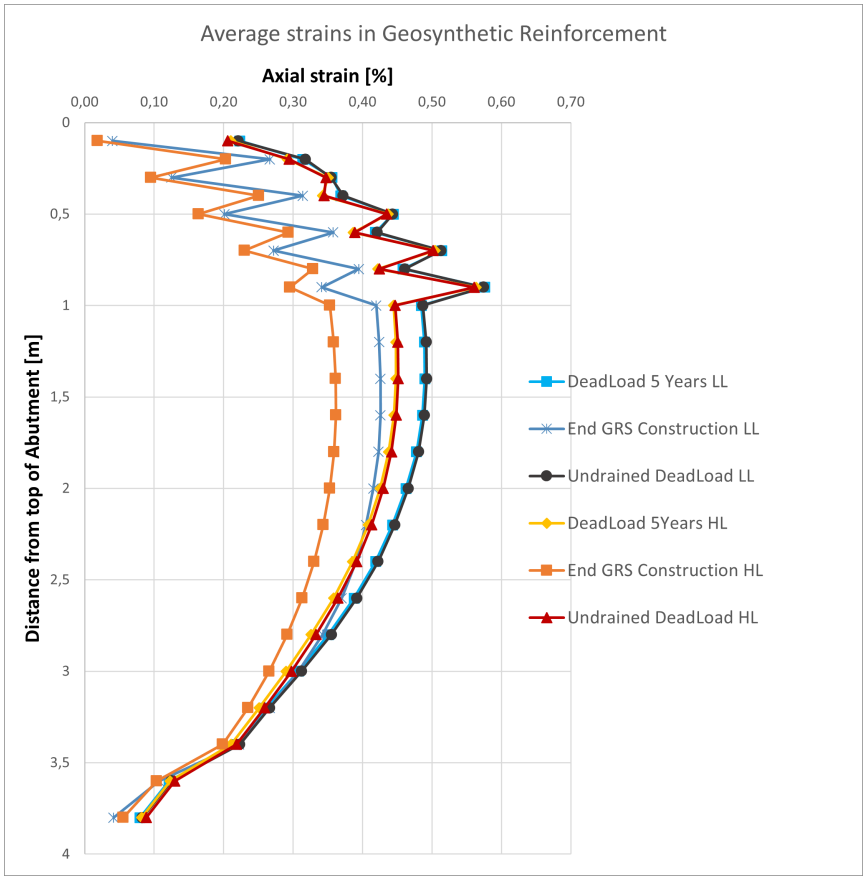

Figure 4.9: Average strains in the reinforcements plotted against depth of abutment. LL = Lower Limit, HL = Higher Limit

by using the local, axial displacement at the end nodes of the geosynthetic reinforcement, finding the elongation, ΔL, dividing it with the original length: $\epsilon = \frac{\Delta L}{L}$. Looking at the LL analysis, the strains vary from an average of 0.30% at end of construction, to 0.38% with the dead load applied. For the HL analysis the strains vary between 0.26% to 0.36% from end of construction to applied dead load. The average strains in the individual reinforcements are plotted in Figure 4.9. The strains in the individual reinforcements can vary from almost 0 to close to 0.6%. The highest strains are observed in the reinforcement located between 0.5 to 1.5 meter below the top of the abutment. From around 2 meter below the top, the strains decrease with depth for all loading cases, LL and HL analysis, ending 0.05 to 0.09% at the bottom.

Analysing the strains in the GRS abutment soil, it exhibits compression in the vertical direction and tension in the horizontal. The soil strains are analysed in a cross-section 0.6 meter behind the front of the abutment, the average shows vertical strains ϵ_H around 0.53%

and average horizontal strains ϵ_V in the range 0.82 to 0.85%. The strains are analysed after ended construction and after 5 years of consolidation has finished.

Average forces in the geosynthetic reinforcement at the end of construction is 1.28 kN/m for LL analysis and 1.20 kN/m for HL analysis. When applying the dead load, the force increases to 1.81 kN/m for LL, and 1.87 for HL. The average force decreases with 0.01 kN/m after a month of consolidation for both types of analysis, not changing further over time. The average force in the individual reinforcements are plotted in Figure 4.10, for different loading cases, HL and LL analysis.

The distribution of the force over the reinforcement is illustrated in Figure 4.11, exhibiting a high peak at the transition between facing and GRS soil structure, decreasing with length and stabilising. The distribution over the reinforcements is similar for all the different load cases, and limit analysis, but with different values. The case illustrated in the figure (4.11) is for HL analysis, during the application of the dead load, when the bridge is put in place.

Average forces in the reinforcement, applying live load, are 2.90 kN/m with approach Undrained A, for the HL analysis and 2.68 kN/m with Undrained B. For the LL analysis using Undrained A, the model fails.

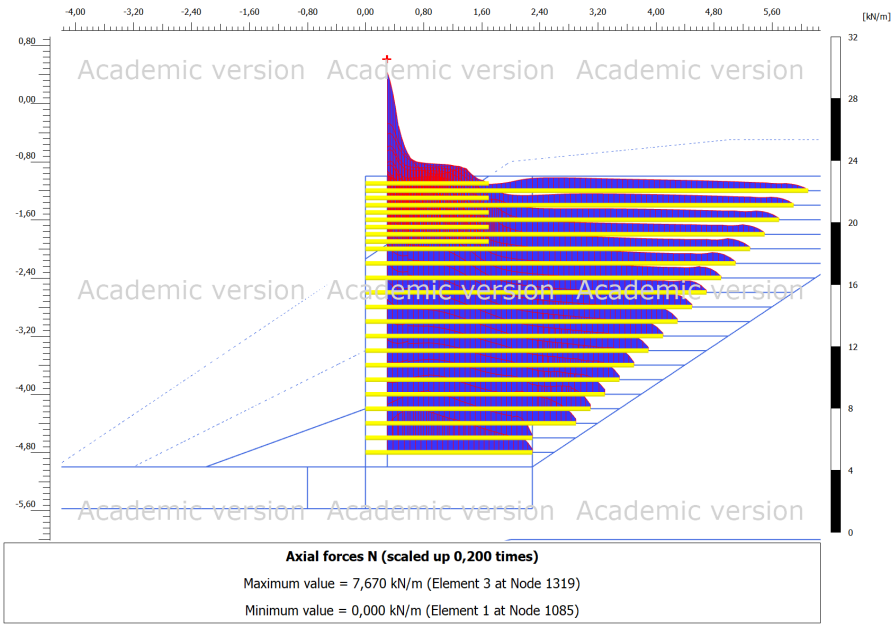

Figure 4.11: Force distribution over the geosynthetic reinforcement

A summary of average forces and average strains, for different load stages an types of analysis are presented in Table 4.3.

Loading conditions	**Average** ϵ (%) LL	**Average** ϵ (%) HL	**Average** T (kN/m) LL	**Average** T (kN/m) HL	**Average** T (kN/m) UB
End of GRS Construction	0.30	0.26	1.28	1.20	1.16
Applying Dead Load	0.38	0.36	1.81	1.87	1.78
Applying Live Load	-	0.58	-	2.90	2.68
Dead Load 1 Month	0.38	0.36	1.80	1.86	-
Dead Load 1 Year	0.38	0.36	1.80	1.86	-
Dead Load 5 Years	0.38	0.36	1.80	1.86	-

Table 4.3: Average strains and tensile forces during different loading conditions, where LL = Lower Limit, HL = Higher Limit and UB = Undrained B.

4.4 Discussion and Conclusion GRS Abutment

The analysis where Undrained B was used exhibited a sufficiently high strength in the structure, implying that stability is not an issue. No strength reduction factors or load factors are applied in this analysis. This model is merely a first draft of a GRS abutment, and if it should be further used in designs, the analysis would have to be reviewed according to relevant standards. However, in this master thesis, the focus is mainly on deformations for the GRS Abutment, and the modelling with Undrained B is used to initially check the stability with the most accurate strength approach. Since the deformations detained when using Undrained B are not as reliable, they were not further investigated.

For the analysis of deformations, Undrained A was used. The difference between the exhibited deformations of the LL approach and the HL approach, with the LL approach resulting in deformations 1.6 to 1.8 times higher than the HL approach in both vertical and horizontal directions. The deformations, ranging between 27 and 78 mm horizontally and 27 and 115 mm vertically, seem reasonable comparing to the two slopes modelled and reviewed in section 3.2 and 3.1. The Lillehammer slope showed deformations in the range of 1-2.6%, and Skedsmo slope 0.3-0.7% of the slope height at the end of construction. The abutment modelled for the Risheim bridge shows deformations around 0.7 to 1.1%. Looking at the deformations in the subsoil, the abutment is located over clay, exhibiting larger subsoil settlement than the slope in Skedsmo, who is built on sand and gravelly soil. For the slope in Skedsmo, deformations in the subsoil were around 16-22% of the total vertical deformations in the analysis, while in Risheim the corresponding part were 37-67%. The settlements of the subsoil were approximately 18-19% higher for the LL analysis compared to the HL analysis. Comparing the deformations to the requirements in Section 2.4, both the LL analysis and the HL analysis are within the acceptable range. The requirements focus on the deformations after the end of the construction. The horizontal

Loading conditions	**Total** u_h (mm) LL	**Total** u_h (mm) HL	**Total** u_v (mm) LL	**Total** u_v (mm) LL	**Abutment** u_h (%) HL/LL	**Abutment** u_v (%) HL/LL
End of GRS Construction	43	27	45	27	0.66/0.98	0.49/0.51
Applying Dead Load	82	45	98	61	0.98/1.14	0.96/0.93
Dead Load 1 Month	79	44	104	64		
Dead Load 1 Year	79	44	109	68		
Dead Load 5 Years	78	43	115	70	1.02/1.17	0.96/0.93
Construction end to 5 Years	35	17	70	43	0.35/0.19	0.47/0.42
Dead Load applied to 5 Years	-3.7	-2.1	16.3	9.4	0.03/0.03	0/0

Table 4.4: Total deformation for the structure, and for the GRS abutment only, for different loading conditions, with LL = Lower Limit, HL = Higher Limit. Deformations: u_v = Vertical, u_h = Horizontal.

deformations in the abutment after the end of construction correlates well with expected values of 0.1 to 0.3 % (Rogbeck et al., 2006), being in the range 0.2 to 0.35 % (4.4). Horizontal deformations after the dead load is applied surprisingly decrease, and the abutment deforms slightly in the direction of the back slope, exhibiting the same behaviour as the Lillehammer slope 3.2. The change is very small but should still be mentioned.

Looking at Figure 4.8 the different results between LL and HL analysis are clear. For both the vertical and horizontal deformations, the subsoil exhibits far greater deformations for the LL case, illustrated by the deformations at the bottom of the abutment (around 4.5 m in the figure), are significantly higher than for the HL analysis. The deformations for the HL analysis with dead load applied, are in the same range as the deformations from the LL analysis at the end of construction of the GRS, without the dead load.

The distribution of deformations over the cross-section in Figure 4.8 correlates well with how the deformations for the Skedsmo slope were distributed, Figure 3.7. The deformation in the abutment itself after end of construction until consolidation of 5 years is actually larger in the HL analysis than in the LL analysis. This is probably due to the fact that the subsoil behaves stiffer in the HL approach, resulting in the GRS abutment itself having to take up more of the applied load.

Looking at change in deformation over time, Figure 4.7, one can assume the primary part of the deformations to be finished after 1.5 to 2 years. Settlements due to creep and degradation are not considered in this model, but are expected to be small, see Section 2.5.1. A large part of settlements are obtained directly after load is applied.

In Section 2.4, the horizontal deformations are obtained from the vertical deformations, assuming plane strain conditions and zero volume change. Using vertical deformations obtained from the model and looking at the GRS abutment only, the horizontal deformation is predicted to be around 14 to 27 mm (both for LL and HL). This is about 40 to 65 % of the values obtained from the modelling, and thus under-predict the horizontal deformations highly in comparison. The horizontal deformations are calculated using Eq. 2.7, with $b_{q,vol}$ = 1.4 m and H = 4 m. For the study of the GRS Abutment in Louisiana (2.4), the horizontal displacements were obtained using the same approach, and compared to monitored results, showing that the method underestimated the real deformations. This could indicate that the horizontal deformations are reasonably realistic.

It should also be kept in mind that in the slopes used in the calibrating cases, the deformations were only measured for the slope in Lillehammer, after ended construction, and this was not satisfactory modelled. In the Skedsmo slope, deformations were not monitored, and the results presented are obtained from the model.

Strains illustrated in Figure 4.9 show a peak of average strains in the reinforcements located at the same depths as the highest horizontal deformations. The strains decrease with depth of the abutment. In Figure 4.9 it can be observed that the secondary reinforcement, located in the top meter, shows a significant response when dead load is applied, during the installation of the bridge. The secondary reinforcement, located in the bearing zone to strengthen the structure where the extra loads of the bridge are located, has an increase in strain around 0.25% when the dead load is applied. The load-response is realistic with the location of the dead load in mind. A zoomed-in adaption of Figure 4.9 with the reinforcement in the background illustrates the behaviour in Figure 4.12.

Average values for all the reinforcements varies between 0.26 and 0.38%, giving a reasonably good fit with the strains obtained from the analysis of the slopes in Section 3.2 and 3.1. The slope in Skedsmo exhibited average strains between 0.14 to 0.41% for in the geogrids, while the slope in Lillehammer had strains around 0.4 and 1.3% in the geotextile at the end of construction. The strains for the bridge abutment in Risheim seem to be in the right scope. Highest average strain, 0.58 %, is obtained when applying live load for the HL, Undrained A model. The average strains in the reinforcement are within the requirements of maximum 2% (Vegdirektoratet, 2018).

The average strains on the soil in the abutment are about $\epsilon_H = 0.53\%$ and $\epsilon_V = 0.85\%$. This is higher than what is specified in guidelines (2.4), which specifies that the vertical strains should be less than 0.5% and horizontal less than 1%. The horizontal strains are within the required range, and correlates well with the strains in the reinforcement. The vertical strains are somewhat high, over the standard requirement.

Reinforcement tensile forces are evaluated for analysis using Undrained A and Undrained B. Average forces for the reinforcement are illustrated in Figure 4.10, at different load cases. The force exhibits the same response-pattern as the strains, with the dead load having a significant impact on the secondary reinforcement. For the analysis with Undrained B, Live load was applied, resulting in even larger increase in average force. The average tensile force in all of the reinforcements are presented in Table 4.3, showing that the average force is lower for all load cases when modelled with Undrained B, indicating that

the material itself has a higher strength than both Undrained A's HL and LL approach. Since the model with Undrained B indicated that the strength is high enough to apply live load, and the LL analysis with Undrained A does not, it may indicate the effective strength of the soil is closer to the HL approach using Undrained A, which withstands the live load.

Modelled with Undrained A, the LL analysis has the highest tensile reinforcement forces at the end of construction but when applying the dead load the HL analysis surpasses and obtains the highest forces. This can be due to the fact that the subsoil is stiffer, as mentioned earlier, and that the abutment itself is being forced to handle more load as a response. The average forces are within the range of 1.16 to 2.90 kN/m, the difference not being that large.

Comparing to the slope modelled in Skedsmo, which has modelled force in the range of 1.11 to 2.72 kN/m, suggesting that the forces exhibited in the modelling of the GRS Abutment are within a realistic range.

Looking at the dimensions, the Skedsmo slope and the Risheim abutment are comparable, both being of a height in the range of 4 to 5 meter. The Skedsmo slope experiences additional permanent loading, as does the bridge abutment in Risheim. The relative similarities make the Skedsmo slope a good case to compare the obtained results. The fact that the modelling results of the Risheim abutment are within the same scope in respect to strains, forces and deformations, indicates that the model is relevant, and the results are realistic. The deformation pattern in the slope and the abutment corresponds well, looking at Figure 3.7 and 4.8. The two cases differ with the Skedsmo slope continuing for 10 meter, bordering to another slope of additionally 10 meter, all in all a 20 meter long structure, while the abutment has superstructure with a width of ca. 7 meter and total width of about 8.5 to 10.5 meter. The assumption of plane strain conditions correlates in general better with structures that has a larger width, as a slope for example, while for structures of a smaller width, like a bridge abutment, the assumption may not be as accurate. In Section 2.7, studies of a GRS bridge abutment modelled in 2D and 3D are presented. In that specific case, the results from the 3D modelling and 2D modelling correlated well, leading to the assumption that 2D modelling of the bridge abutment gives satisfactory results and can be utilised with success. The bridge abutment in the study has a width of 13 meter, a bit larger than the abutment designed for Risheim, but still near enough to give a relevant input.

Many of the soil parameters used in the modelling of the Abutment are estimated, and even though they are within a reasonable range, they give an approximate result. The choices made in relation to the HL analysis are on the conservative side and may be even higher in reality. The constitutive models chosen for the FEM analysis are relatively simple, and even though they give a good estimate, they do not take long-term effects like creep and degradation into account. With more detailed soil investigations, more advanced soil models can be used, and more accurate assumptions of the soil characteristics made.

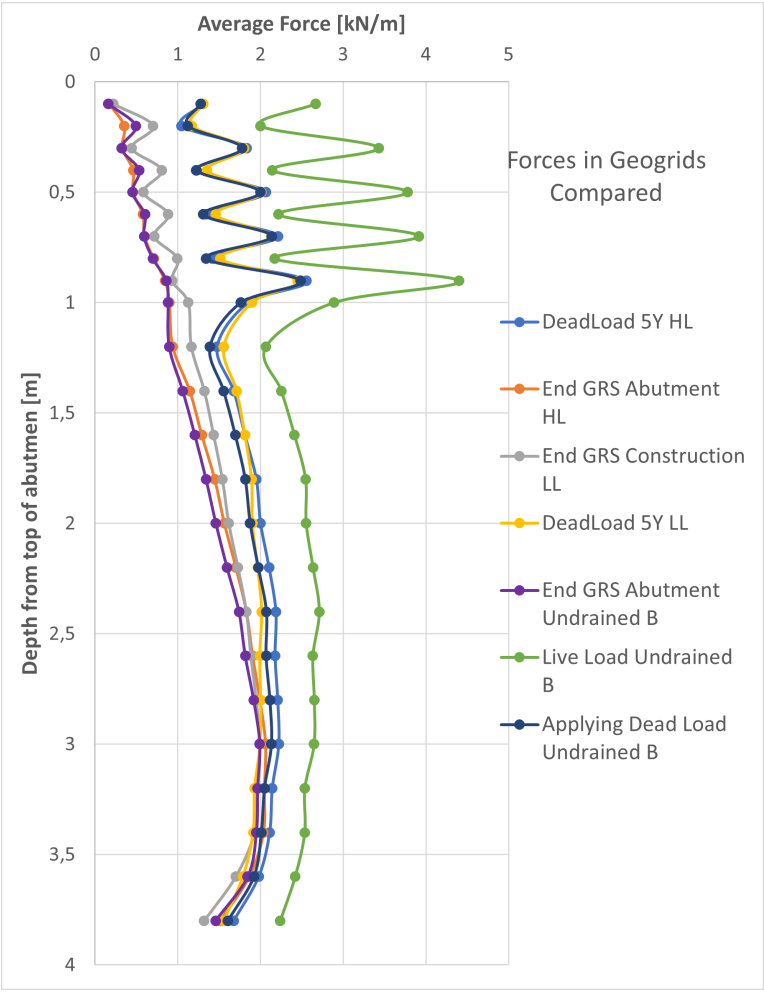

Figure 4.10: Average force in the reinforcements plotted against depth of abutment. LL = Lower Limit, HL = Higher Limit

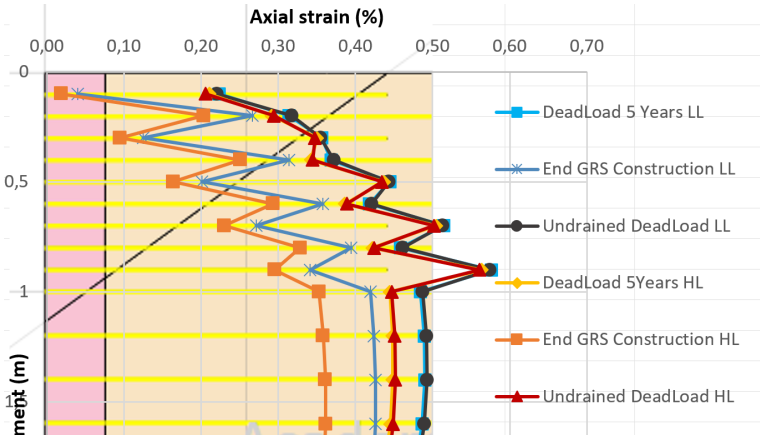

Figure 4.12: Illustration of Figure 4.9, with secondary reinforcement in the background.

Chapter 5

Summary and Conclusion

Two existing GRS slopes built in Norway during the late 80's and early 90's have been monitored with respect to deformations, strains and forces. The slopes have been used to calibrate the FEM model of GRS structures, comparing the results obtained from the modelling with the actual monitored results. The slopes are located in Lillehammer and Skedsmo. The modelling approach giving the highest correspondence between measurements and model was further used in the modelling of a possible GRS bridge abutment. A smaller bridge located in Risheim in Norway, shall eventually be replaced by a new one. The dimensions of the bridge, and the relatively solid soil foundation makes it a possible candidate for abutment construction using the GRS approach. A suggested GRS abutment for the Risheim bridge was modelled. The results were evaluated especially with respect to strains and deformations in the structure, comparing it to the calibration case, expected behaviour and requirements from theory in literature and design standards.

The modelling of the two monitored GRS slopes, Lillehammer and Skedsmo, had various outcome. Modelled results for the slope located in Skedsmo fit reasonably well with the monitored measurements, see Section 3.1. Force and strains in the geogrids were within the same scope as the measured strains and forces, and the deformations exhibited in the model output are what could be expected for a corresponding GRS structure. The average strains and forces in the geogrids are within the recommended requirements, Section 2.4. The deformations in the slope were not monitored, and only compared to theoretical results. Overall, the results correlated good enough to argue that the approach used when modelling the Skedsmo slope gives a realistic prediction of the behaviour of a reinforced structure, and can be adapted and further used.

The outcome of the model of the slope in Lillehammer, Section 3.2, did not successfully predict the long-term deformations in the slope. The monitored parameters for the slope were the horizontal deformations, measured after the end of the construction. The forces and strains in the geotextile gave reasonable results compared to what could be expected looking at the theory and comparing it with the slope in Skedsmo, Section 3.3. The deformations in the structure until the end of construction are within an acceptable

range compared to the deformations found in modelling of the slope in Skedsmo. After the end of construction, the model failed to predict deformations realistically. The reason is possibly because the constitutive soil models used in the slope, the hardening soil model, mainly corresponds to load changes, and does not take creep and degradation into account. The slope in Lillehammer does not experience any additional external loading after the end of construction, and the attempt to model the change in loading by modelling partially drained condition did not succeed. Modelling change in pore pressures correctly is challenging, especially using simpler soil models. For a better prediction of the post-construction behaviour, more detailed examination of the soil is needed, so that more advanced soil models can be applied.

Modelling of the GRS abutment for the bridge in Risheim was done using the approach calibrated in the Skedsmo case. The layout and design of the model is described in Section 4. Two models were conducted, one looking into the stability of the structure and the other focused on deformations and strains. The results showed a sufficient strength for the structure, indicating satisfying stability of the structure.

In the analysis, looking into deformations and strains, a higher and lower limit approach was used, since not all of the effective material parameters were investigated in the soil investigation, and had to be estimated. The Results from the modelling (both LL and HL) exhibited strains and forces in the reinforcement within a realistic scope compared to the slope in Skedsmo and satisfied the recommended requirements, Section 2.4. The reinforcement force and strains from the stability analysis correlate best with the HL approach, indicating that this may be more accurate with respect to material strength. The distribution of the strains and forces in the reinforcement shows a realistic response to applied load, indicating that the model can be representative for a real case. The deformations exhibited are 1.8 times higher for the LL than the HL approach, but both are within reasonable magnitude when comparing to the modelling of the slopes in Skedsmo and Lillehammer. The main difference between the LL and HL approach is that the settlements in the foundation soil are much higher in the LL approach, which is highly realistic. The post-construction deformations, in both HL and LL approach, are within the range of the maximum suggested values and in the expected scope, see Section 4.4 and 2.4.

The fact that the slope in Skedsmo and the abutment in Risheim had similar dimensions and comparable loading conditions makes the comparison between the two cases sensible and valid. For a more precise modelling approach, more detailed soil investigations need to be performed. The range for the soil parameters estimated have been chosen a bit on the conservative side and could be altered. The most accurate approach would be to establish the effective parameters needed for the analysis.

The GRS abutment is modelled in 2D, assuming plane strain conditions. This may not be realistic since the width of the abutment is about 7 meter, and strains of significance in the lateral direction could be present. By modelling the abutment in 3D, and comparing the results with the 2D model, one can see how big of an impact the assumption has on the results.

All in all, the modelled GRS abutment in Risheim showed acceptable deformations and strains. The model can be assumed to have a reasonably good correlation with the reality

and could be used as a basis for further analysis of the possibility to establish GRS abutments for the Risheim bridge. The results from the model indicates that it is a possible solution to use GRS abutments Risheim, with an outcome in the acceptable range regarding deformations and strains in the abutment. More detailed analysis would have to be done for a final conclusion in the case.

The main conclusions found in this study are listed below:

- The modelling approach used in the calibration case gives realistic output for strains, forces and deformations in the structure when the structure is subjected to additional load post-construction. If the structure is only being subjected to its self-weight over time, the model does not give realistic deformations.
- If long-term deformations due to degradation and creep should be taken into account, more advanced soil models must be applied.
- For a better and more precise prediction of the GRS structure response and deformations, more detailed soil investigations must be performed to limit uncertainties associated to the soil parameters.
- For a better evaluation base of the deformations, it would be preferable with a calibration case that has corresponding loading conditions as a GRS bridge abutment, where deformations have been monitored over time.
- The modelled GRS abutment in Risheim exhibits realistic strains and forces in the reinforcement as well as deformations. The modelled results are within proposed requirements from the literature and standards, indicating that it can be good, alternative solution.
- The deformations of the GRS Abutment itself stopped almost immediately after end of construction and the placement of dead load. The deformations in the subsoil seem to be close to zero after 1.5 to 2 years of consolidation, with the main part of the settlements occurring when applying the load.
- The outcome of the analysis leads to the conclusion that GRS abutment can be a good solution for cases with similar properties like Risheim, and that it is relevant to further investigate the option.

Chapter 6

Further Work

For GRS bridge abutment to be a realistic choice of design, more detailed investigations have to be performed, with less uncertainties in the soil properties. More detailed soil investigations, providing soil properties with higher accuracy, would give a more reliable result. Calibrating the FEM model, using cases where GRS supporting structures are monitored, including deformations, would increase the reliability of the results. Lab scale models, monitored over time, could be a valid tool to investigate a GRS abutment behaviour in a controlled environment. The results could also be further modelled and used as calibration for FEM analysis.

The accuracy of the FEM model can be increased by using more advanced soil models, provided that they can be utilised in a realistic way. Detailed soil investigations that provide necessary information is required for the advanced models to be valid. Since the scope of this thesis only covers 2D FEM analysis of the abutment, 3D analysis should be utilised, investigating the impact of out of the plane strains and deformations in the abutment.

Bibliography

Abrahamsen, R. B. and Valnes, T. (2011). Alternativer på kort og lang sikt for 02-699 Risheim bru, fv 504. En mulighetsstudie. Technical Report 02-699, Statens Vegvesen Region Øst, Sweco.

Abu-Farsakh, M., Ardah, A., and Voyiadjis, G. (2018). 3D Finite element analysis of the geosynthetic reinforced soil-integrated bridge system (GRS-IBS) under different loading conditions. *Transportation Geotechnics*, 15:70–83. https://doi.org/10.1016/j.trgeo.2018.04.002.

Abu-Farsakh, M. Y., Ardah, A., and Voyiadjis, G. Z. (2019). Numerical parametric study to evaluate the performance of a Geosynthetic Reinforced Soil–Integrated Bridge System (GRS-IBS) under service loading. *Transportation Geotechnics*, 20:100238. https://doi.org/10.1016/j.trgeo.2019.04.001.

Abu-Hejleh, N., Wang, T., and Zornberg, J. G. (2000). Performance of Geosynthetic-Reinforced Walls Supporting Bridge and Approaching Roadway Structures. In *Advances in Transportation and Geoenvironmental Systems Using Geosynthetics*, pages 218–243, Denver, Colorado, United States. American Society of Civil Engineers. https://doi.org/10.1061/40515(291)15.

Adams, M., Nicks, J., Stabile, T., Schlatter, W., Hartmann, J., and United States. Federal Highway Administration. Office of Infrastructure and Transportation Performance (2012). Geosynthetic Reinforced Soil Integrated Bridge System Interim Implementation Guide. Technical Report FHWA-HRT-11-026, United States. Federal Highway Administration. Office of Infrastructure and Transportation Performance.

Adams, M., Nicks, J., Stabile, T., Wu, J. T., Schlatter, W., Hartmann, J., and United States. Federal Highway Administration. Office of Infrastructure Research and Development (2011). Geosynthetic Reinforced Soil Integrated Bridge System, Synthesis Report. Technical Report FHWA-HRT-11-027, United States. Federal Highway Administration. Office of Infrastructure and Transportation Performance.

Adams, M. T., Ketchart, K., and Wu, J. T. H. (2007). Mini Pier Experiments: Geosynthetic Reinforcement Spacing and Strength as Related to Performance. In *Geosynthetics in Reinforcement and Hydraulic Applications*, pages 1–9, Denver, Colorado, United States. American Society of Civil Engineers. https://doi.org/10.1061/40909(228)10.

Allen, T. and Bathurst, R. (1996). Combined Allowable Strength Reduction Factor for Geosynthetic Creep and Installation Damage. *Geosynthetics International*, 3(3):407–439. https://doi.org/10.1680/gein.3.0069.

Anderson, P. L., Gladstone, R. A., and Sankey, J. E. (2012). State of the Practice of MSE Wall Design for Highway Structures. In *Geotechnical Engineering State of the Art and Practice*, pages 443–463, Oakland, California, United States. American Society of Civil Engineers.

Anderson, P. L., Gladstone, R. A., and Withiam, J. L. (2010). Coherent Gravity: The Correct Design Method for Steel-Reinforced MSE Walls. In *Earth Retention Conference 3*, pages 512–521, Bellevue, Washington, United States. American Society of Civil Engineers.

Ardah, A., Abu-Farsakh, M., and Voyiadjis, G. (2017). Numerical evaluation of the performance of a Geosynthetic Reinforced Soil-Integrated Bridge System (GRS-IBS) under different loading conditions. *Geotextiles and Geomembranes*, 45(6):558–569. https://doi.org/10.1016/j.geotexmem.2017.07.005.

Ardah, A., Abu-Farsakh, M., and Voyiadjis, G. (2021). Numerical parametric study of geosynthetic reinforced soil integrated bridge system (GRS-IBS). *Geotextiles and Geomembranes*, 49(1):289–303. https://doi.org/10.1016/j.geotexmem.2017.07.005.

Carrubba, P., Montanelli, F., and Nicola, M. (1999). Instrumented soil reinforced retaining wall: Analysis of measurements. In *Instrumented soil reinforced retaining wall: Analysis of measurements*, pages 921–934, Boston, U.S.A.

Elias, V. (2001). Long-term durability of geosynthetics based on exhumed samples from construction projects. Technical Report FHWA-RD-00-157, Federal Highway Administration.

Emdal, A. (2013). Introduksjon til geoteknikk. Place: Trondheim.

Fannin, R., Quinteros, S., Vaslestad, J., and Ahmed, T. (2014). Behaviour of a geosynthetic reinforced soil slope: A 25 year field study. In *Behaviour of a geosynthetic reinforced soil slope: A 25 year field study*, Berlin, Germany. Deutsche Gesellschaft fur Geotechnik e.V.

Fannin, R. J. and Hermann, S. (1990). Performance data for a sloped reinforced soil wall. *Canadian geotechnical journal*, 27(5):676–686. Place: Ottawa, Canada Publisher: NRC Research Press.

Fjeldheim, N. (1993). Armert jord med grønn front : ny forbindelse fra E6 til Lillehammer sentrum. *Vegdirektoratet*.

Gofar, N. (2008). Geosynthetic reinforced soil structure. In *Ground Improvement and Stabilization*. Penerbit Universiti Teknologi Malaysia.

Helwany, S. M. B., Wu, J. T. H., and Froessl, B. (2003). GRS bridge abutments—an effective means to alleviate bridge approach settlement. *Geotextiles and Geomembranes*, 21(3):177–196. https://doi.org/10.1016/S0266-1144(03)00004-9.

Holtz, R. D. and Lee, W. F. (2002). Internal Stability Analyses of Geosynthetic Reinforced Retaining Walls. Technical Report WA-RD-532.1, Washington State Transportation Commission.

Jones, C. J. F. P. (1996). *Earth reinforcement and soil structures*. Thomas Telford Publishing. https://doi.org/10.1680/erass.34891.

Koerner, R. M. (2012). *Designing with Geosynthetics - 6Th Edition Vol. 1*. Xlibris Corporation.

Lopes, M.-L. (2002). 2. Soil–geosynthetic interaction. In *Geosynthetics and their applications*, pages 55–79. Thomas Telford Publishing. https://doi.org/10.1680/gata.31173.0002.

Lovdata.no (2021). Lovdata, Forskrift for trafikklast på bruer, ferjekaier og andre bærende konstruksjoner i det offentlige vegnettet (trafikklastforskrift for bruer m.m.). https://lovdata.no/dokument/SF/forskrift/2017-11-17-1900.

McGown, A., Andrawes, K. Z., and Al-Hasani, M. M. (1978). Effect of inclusion properties on the behaviour of sand. *Géotechnique*, 28(3):327–346. https://doi.org/10.1680/geot.1978.28.3.327.

Murray, R. T. (1980). Fabric Reinforced Earth Walls: Development of Design Equations. *Ground Engineering*, 13(7):29–36.

Nokken, M. (2010). Risheim Bru, Datarapport Grunnundersøkelser. Datarapport 713755-01, Sweco.

Nordal, S. (2020). TBA4116 Geotechnical Engineering Advanced Course.

Norgeskart.no (2021). Norgeskart. www.norgeskart.no.

PLAXIS (2021a). *PLAXIS 2D Material Models Manual*. Bentley Systems Incorporated. https://communities.bentley.com/products/geotech-analysis/w/plaxis-soilvision-wiki/46137/manuals—plaxis.

PLAXIS (2021b). *PLAXIS 2D Reference Manual*. Bentley Systems Incorporated. https://communities.bentley.com/products/geotech-analysis/w/plaxis-soilvision-wiki/46137/manuals—plaxis.

Rogbeck, Y., Alén, C., Franzén, G., Kjeld, A., Odén, K., Watn, A., and Øiseth, E. (2006). *Nordisk håndbok: Armert Jord og Fyllinger*. De geotekniske foreningene i norden Nordisk Industrifond. Edition: Rev. B, norsk utg.

Saghebfar, M., Abu-Farsakh, M., Ardah, A., Chen, Q., and Fernandez, B. A. (2017). Performance monitoring of Geosynthetic Reinforced Soil Integrated Bridge System (GRS-IBS) in Louisiana. *Geotextiles and Geomembranes*, 45(2):34–47. https://doi.org/10.1016/j.geotexmem.2016.11.004.

Shukla, S. (2002). *Geosynthetics and their applications*. Thomas Telford Publishing, London.

Shukla, S., Sivakugan, N., and Das, B. (2009). Fundamental concepts of soil reinforcement — an overview. *International Journal of Geotechnical Engineering*, 3(3):329–342. https://doi.org/10.3328/IJGE.2009.03.03.329-342.

Shukla, S. K. (2017a). Basic Description of Soil and Soil Reinforcement. In Shukla, S. K., editor, *Fundamentals of Fibre-Reinforced Soil Engineering*, Developments in Geotechnical Engineering, pages 1–21. Springer, Singapore. https://doi.org/10.1007/978-981-10-3063-5_1.

Shukla, S. K. (2017b). Soil Reinforcing Mechanisms and Models. In Shukla, S. K., editor, *Fundamentals of Fibre-Reinforced Soil Engineering*, Developments in Geotechnical Engineering, pages 111–144. Springer, Singapore. https://doi.org/10.1007/978-981-10-3063-5_4.

Stokkebø, S. H. (1989). Armert jord. ISBN: 8272426072 Place: Oslo Series: Kommunalteknikk.

Tatsuoka, F., Tateyama, M., Uchimura, T., and Koseki, J. (1997). Geosynthetic-Reinforced Soil Retaining Walls as Important Permanent Structures 1996 - 1997 Mercer Lecture. *Geosynthetics International*, 4(2):81–136. https://doi.org/10.1680/gein.4.0090.

TENSAR (2005). The Properties and Performance of Tensar Uniaxial Geogrids. Issue 6, 79010056.

Vaslestad, J. and Anthi, A. (2017). Jordarmerte landkar for bruer. Fleksibelt, økonomisk og miljøvennlig.

Vaslestad, J., Fjeldheim, N., Braaten, A., and Johansen, T. H. (1996). Long-term behaviour of a 13 m high reinforced steep soil slope. Paper presented at Euro Geo 1 Maastrict. *20*. Accepted: 2014-02-03T07:35:09Z Publisher: Vegdirektoratet.

Vaslestad, J., Murad, S. S., Damtew, T., and Johansen, T. H. (2012). Long term performance of instrumented geosynthetic reinforced steep slopes in Norway.

Vegdirektoratet (2018). *Geoteknikk i vegbygging, Håndbok v220*. Statens Vegvesen.

Vegdirektoratet (2019). *Prefabrikkerte brubjelker, Håndbok V426*. Statens Vegvesen.

Vegdirektoratet (2021). *Vegnormal N200 Vegbygging*. Statens Vegvesen. https://svv-cm-store-prod.azurewebsites.net/svv-proj-1464925.

Wahls, H. E. (1990). *Design and construction of bridge approaches*, volume 159. Transportation Research Board.

Wu, J. T., Ketchart, K., and Adams, M. (2001). GRS Bridge Piers And Abutments. Technical report, University of Colorado at Denver.

Wu, J. T. H., Lee, K. Z. Z., Helwany, S. M. B., and Ketchart, K. (2006). *Design and Construction Guidelines for Geosynthetic-Reinforced Soil Bridge Abutments with a Flexible Facing*, volume 556. Transportation Research Board, Washington, D.C. https://doi.org/10.17226/13936.

Wu, J. T. H. and Ooi, P. S. K. (2015). Synthesis of Geosynthetic Reinforced Soil (GRS) Design Topics. Technical Report FHWA-HRT-14-094, Federal Highway Administration.

Wu, J. T. H., Yang, K.-H., Mohamed, S., Pham, T., and Chen, R.-H. (2014). Suppression of Soil Dilation—A Reinforcing Mechanism of Soil-Geosynthetic Composites. *Transportation Infrastructure Geotechnology*, 1(1):68–82. https://doi.org/10.1007/s40515-014-0003-6.

Ziegler, M. (2017). Application of geogrid reinforced constructions: History, recent and future developments. In *Proceedings of first international symposium on Archimedes bridge (ISAB-2010)*, volume 172 of *Procedia Engineering*, pages 42–51, Amsterdam. Elsevier. ISSN: 18777058.

Zienkiewicz, O., Taylor, R., and Zhu, J. (2013). Chapter 1 - the standard discrete system and origins of the finite element method. In Zienkiewicz, O., Taylor, R., and Zhu, J., editors, *The finite element method: its basis and fundamentals (seventh edition)*, pages 1–20. Butterworth-Heinemann, Oxford, seventh edition edition. https://doi.org/10.1016/B978-1-85617-633-0.00001-0.

Appendix

Appendix A

Skedsmo Slope

PLAXIS 2D Version 21.1.0.479

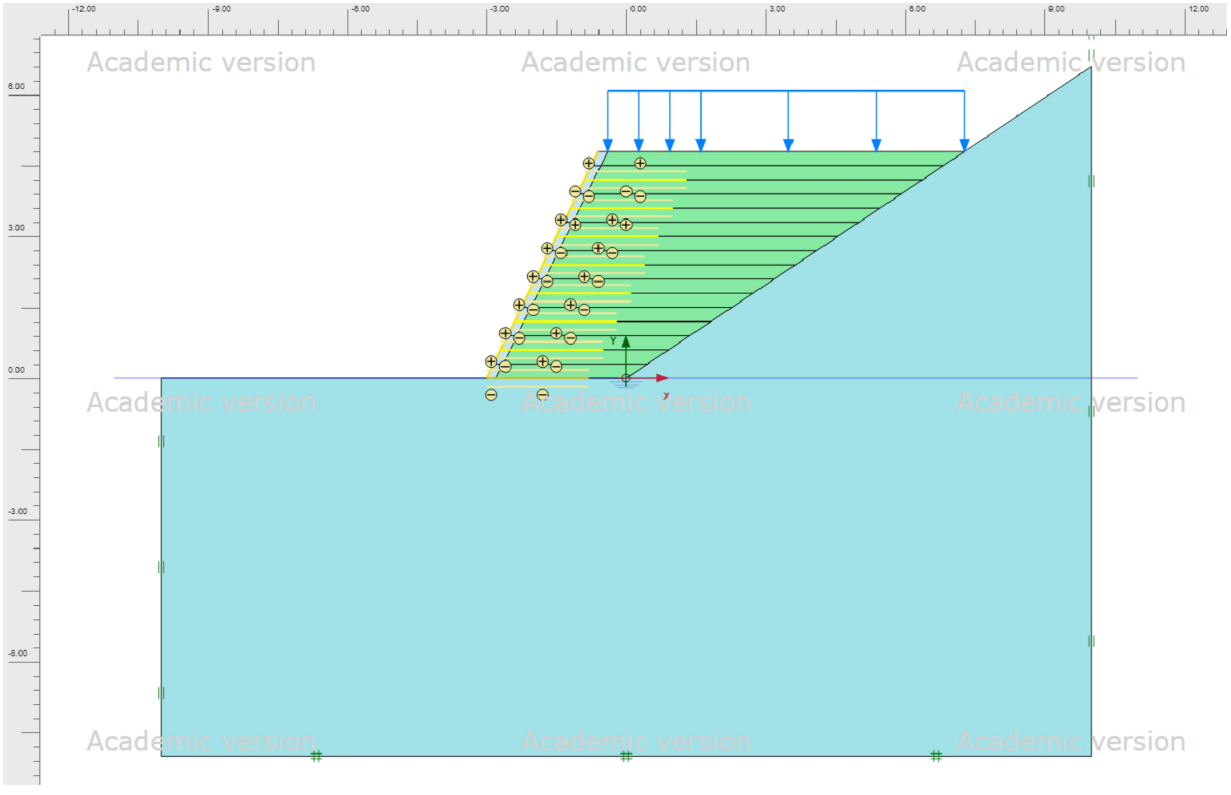

PLAXIS® 2D CONNECT Edition	*Project description* SL_Skedsmo_start	*Date* 25.11.2021
	Project filename SL_Skedsmo_v5_Dr.p2dx	*Company* NTNU

Appendix B

Lillehammer Slope

PLAXIS 2D Version 21.1.0.479

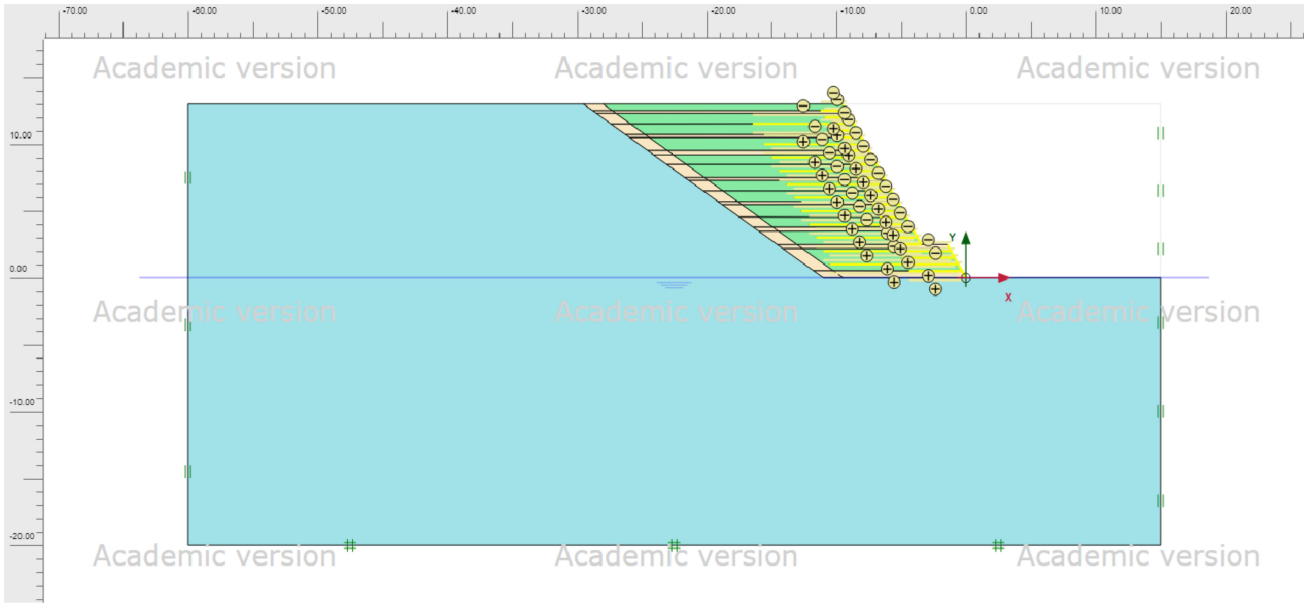

PLAXIS® 2D CONNECT Edition	*Project description* Model Lillehammer	*Date* 11.01.2022
	Project filename SL_Lill_simple_undr.p2dx	*Company* NTNU

PLAXIS 2D Version 21.1.0.479

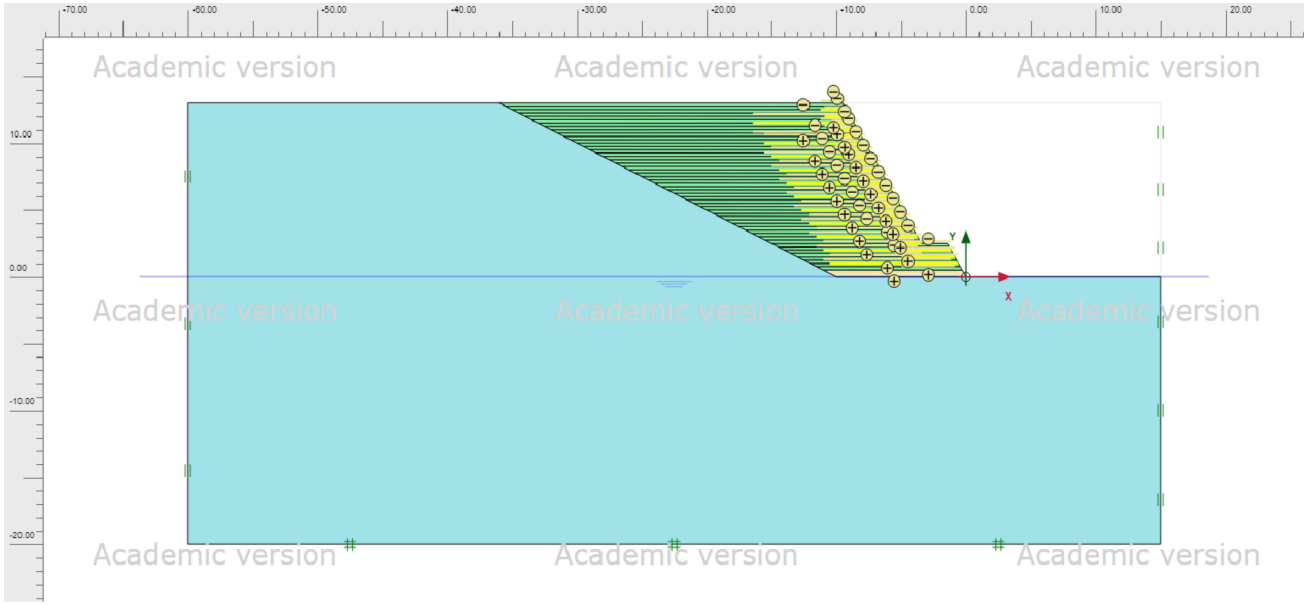

PLAXIS® 2D CONNECT Edition	*Project description* Model Lillehammer 52 Soillifts	*Date* 11.01.2022
	Project filename SL_Lill_v3.p2dx	*Company* NTNU

Appendix C

Risheim

PLAXIS 2D Version 21.1.0.479

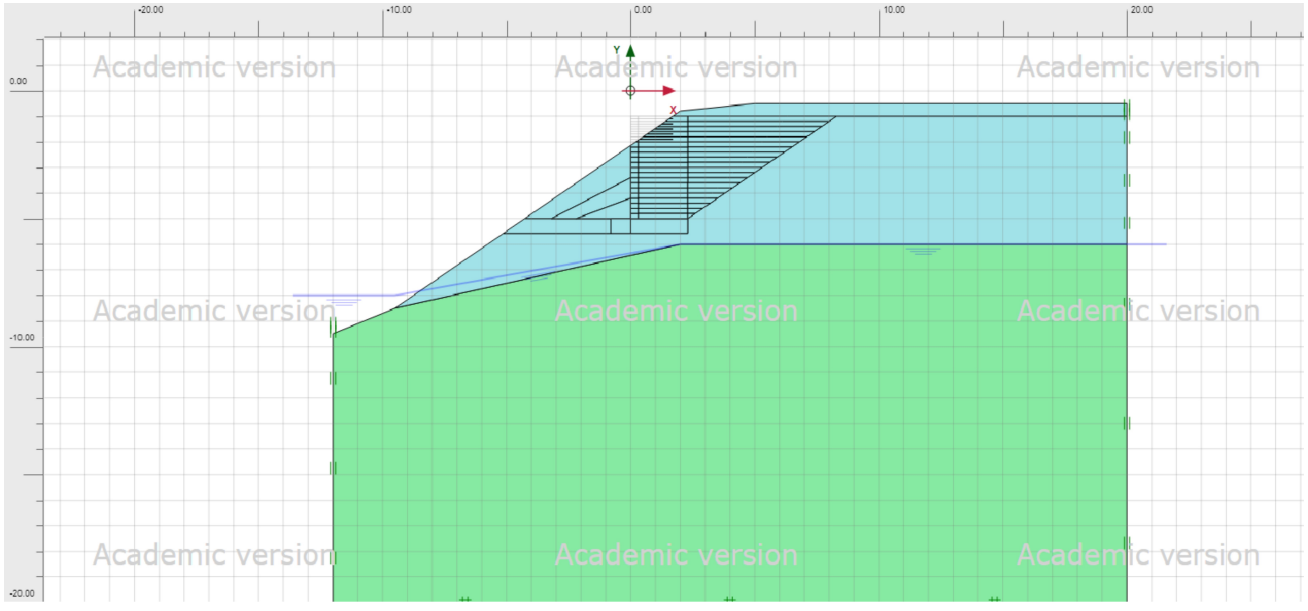

PLAXIS® 2D
CONNECT Edition

Project description	Date
Model Initial Geometry Risheim	11.01.2022
Project filename	**Company**
GRS_Bridgeabutment_Risheim_Inte ...	NTNU

PLAXIS 2D Version 21.1.0.479

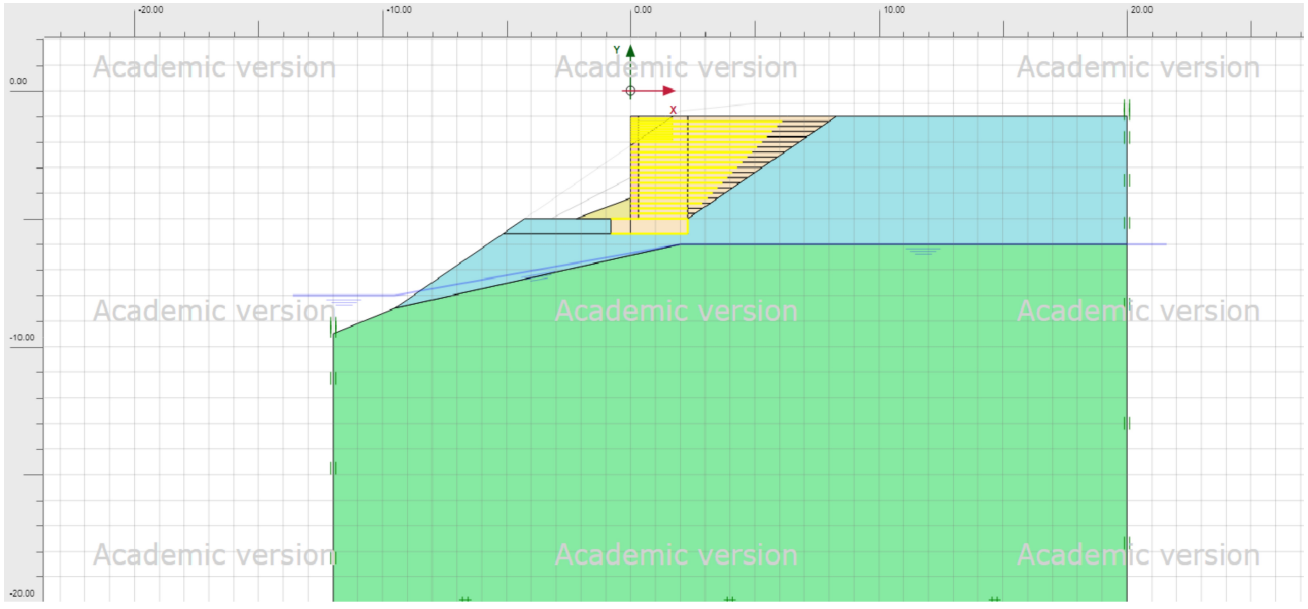

PLAXIS® 2D
CONNECT Edition

Project description	Date
GRS Brige Abutment Risheim	11.01.2022
Project filename	**Company**
GRS_Bridgeabutment_Risheim_Inte ...	NTNU

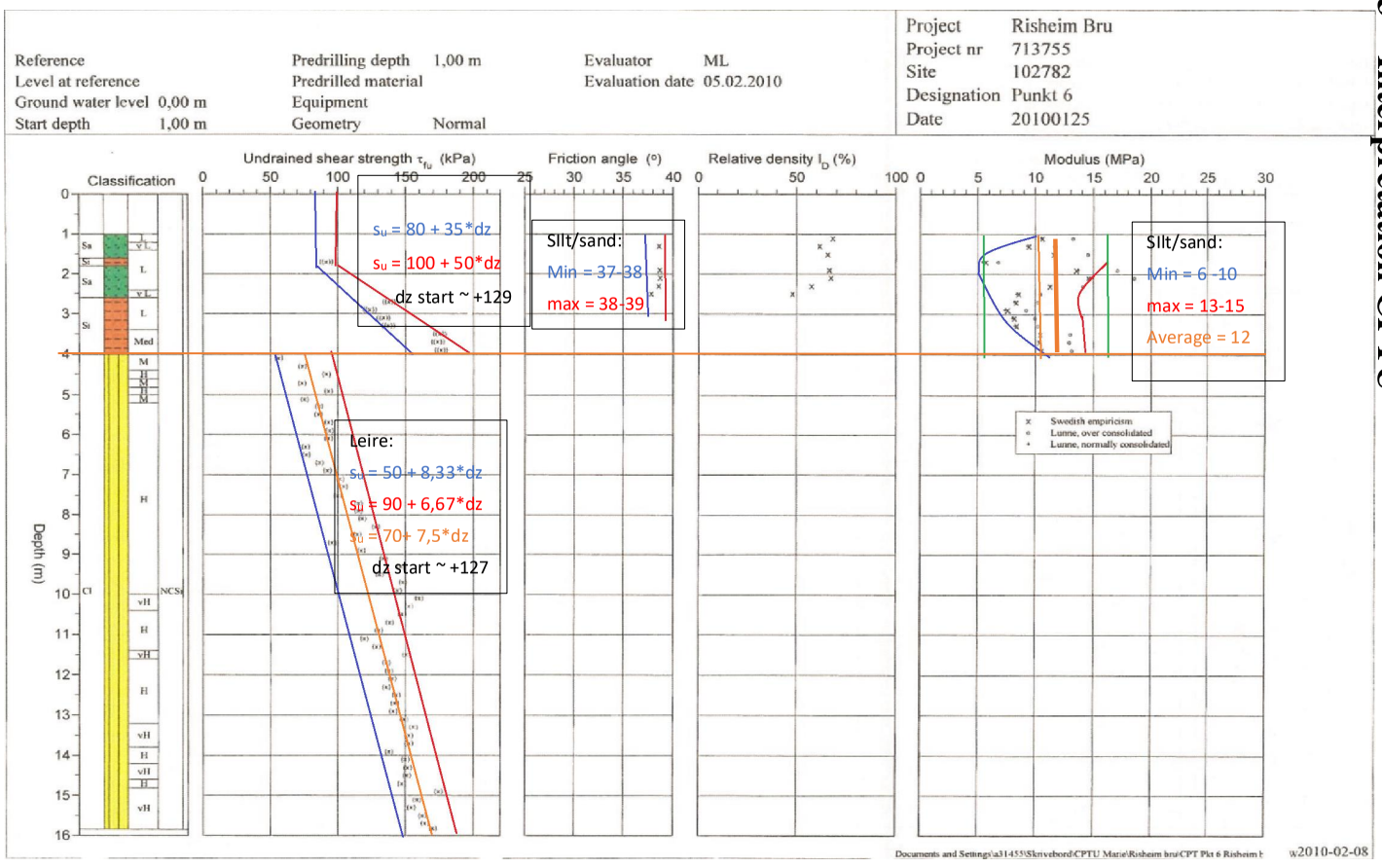
Reference
Level at reference
Ground water level 0,00 m
Start depth 1,00 m
Predrilling depth 1,00 m
Predrilled material
Equipment
Geometry Normal
Evaluator ML
Evaluation date 05.02.2010
Project Risheim Bru
Project nr 713755
Site 102782
Designation Punkt 6
Date 20100125
Classification
Undrained shear strength τ_{fu} (kPa)
Friction angle (°)
Relative density I_D (%)
Modulus (MPa)
Depth (m)
s_u = 80 + 35*dz
s_u = 100 + 50*dz
dz start ~ +129
Silt/sand:
Min = 37-38
max = 38-39
Silt/sand:
Min = 6 -10
max = 13-15
Average = 12
Leire:
s_u = 50 + 8,33*dz
s_u = 90 + 6,67*dz
s_u = 70+ 7,5*dz
dz start ~ +127
Swedish empiricism
Lunne, over consolidated
Lunne, normally consolidated
Documents and Settings\a31455\Skrivebord\CPTU Marie\Risheim bru\CPT Plot 6 Risheim b
w2010-02-08

Reference		Predrilling depth	136,20 m	Evaluator	ML
Level at reference	137,20 m	Predrilled material		Evaluation date	07.01.2010
Ground water level	130,70 m	Equipment			
Start depth	136,20 m	Geometry	Normal		

Project	Risheim bru
Project nr	713755
Site	104135
Designation	Punkt 2
Date	20091222

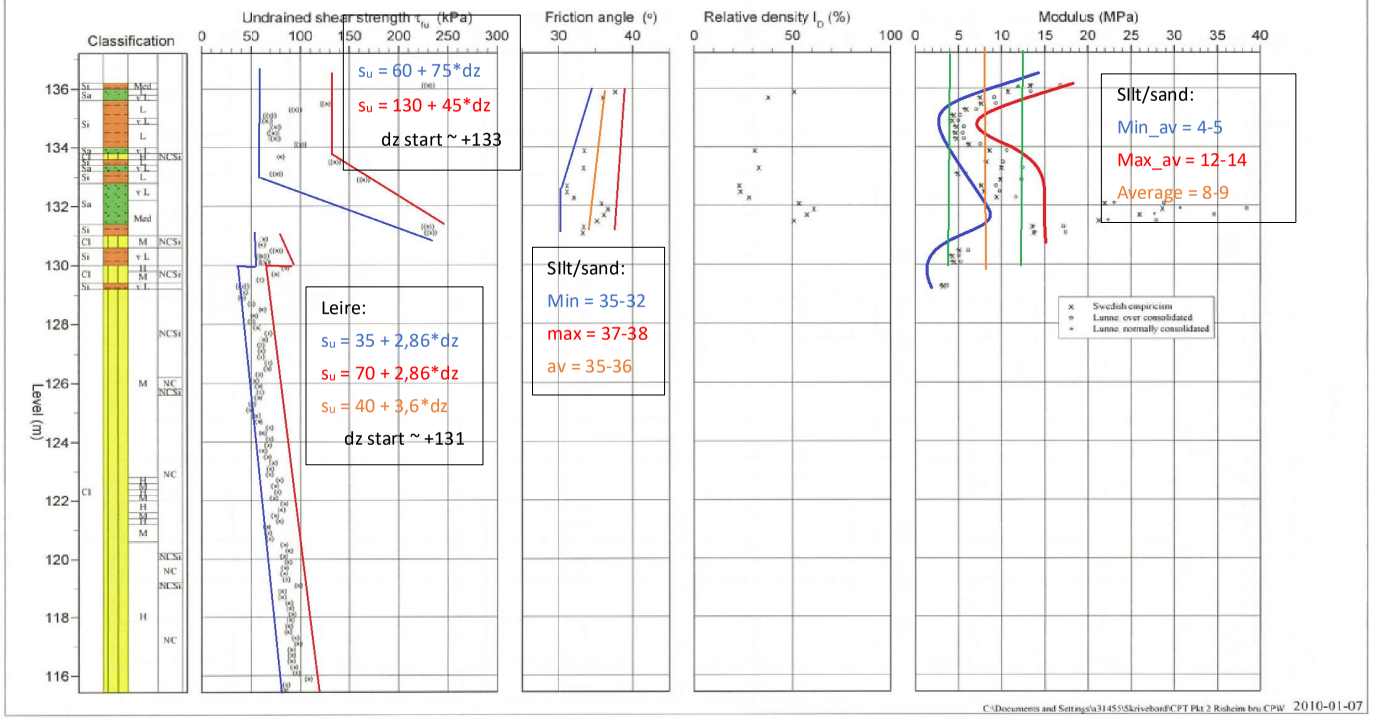

C.4 Cross-Section with GRS Abutment

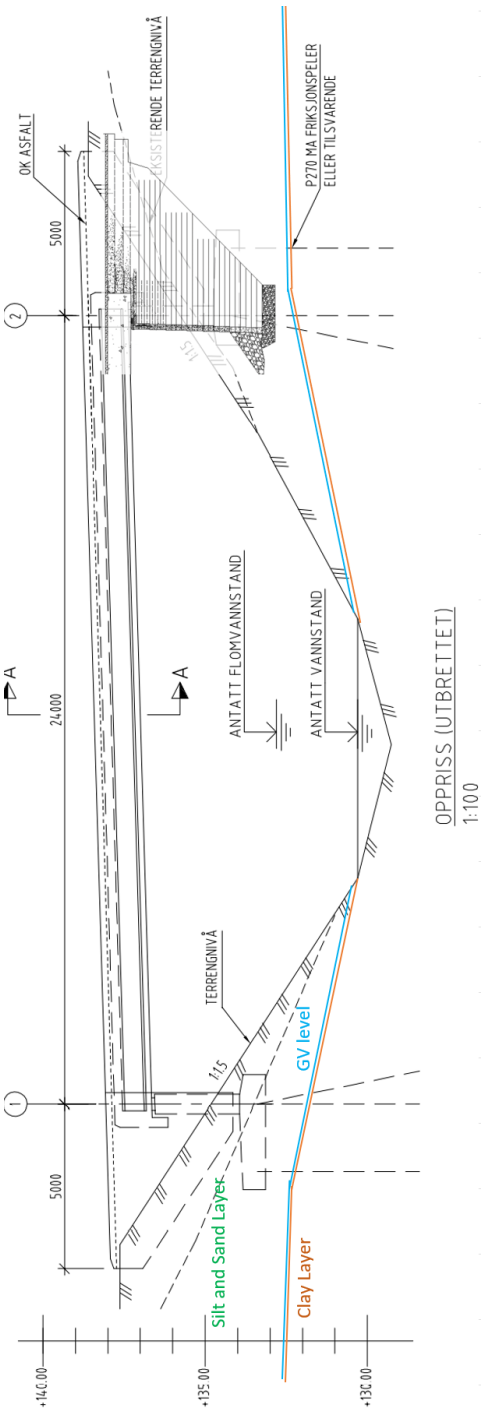

C.5 Cross-Section for the New Bridge

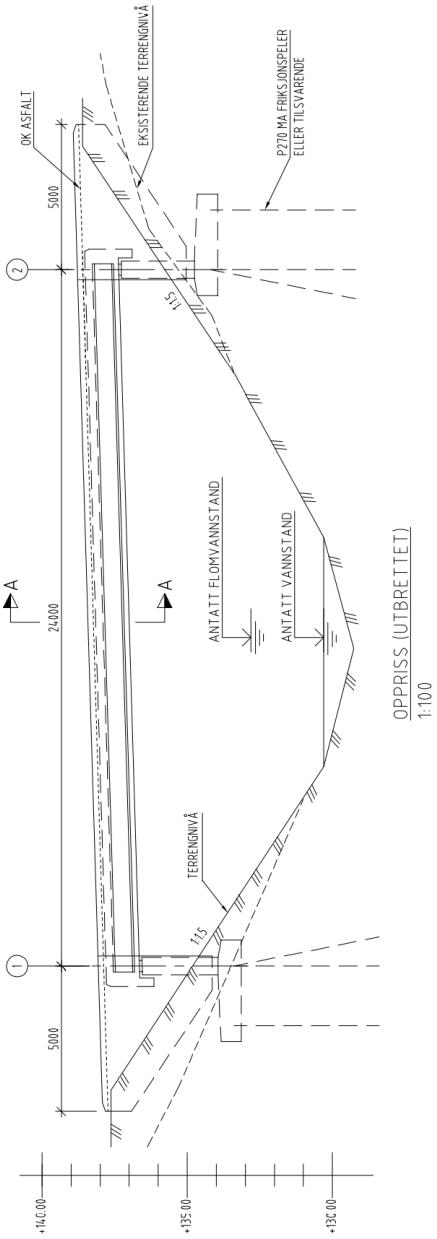

C.6 Interpretation soil layers overview

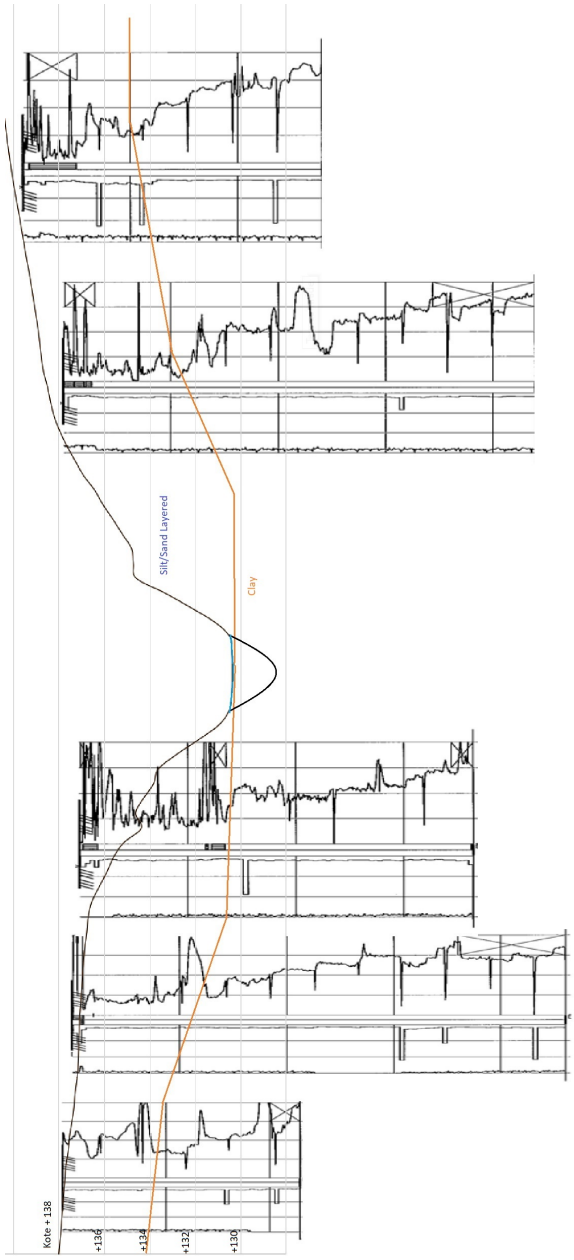

Ida Lindkvist

Bridge Abutment Using Geosynthetic Reinforced Soil Technique

NTNU
Norwegian University of
Science and Technology